University of Pardubice
Faculty of Chemical Technology

MASTER THESIS

Synthesis and properties of undoped and Er^{3+}-doped TeO_2–ZnO–BaO glasses for optical applications

Jan HRABOVSKÝ

Supervisor: Ing. Lukáš Střižík, Ph.D.
Advisor: Prof. Ing. Tomáš Wágner, CSc.
Study programme: Chemistry and Technology of Materials
Specialization: Material Engineering

Pardubice, Czech Republic
2019

Univerzita Pardubice
Fakulta chemicko-technologická
Akademický rok: **2018/2019**

ZADÁNÍ DIPLOMOVÉ PRÁCE

(PROJEKTU, UMĚLECKÉHO DÍLA, UMĚLECKÉHO VÝKONU)

Jméno a příjmení:	**Bc. Jan Hrabovský**
Osobní číslo:	**C16502**
Studijní program:	**N2808 Chemie a technologie materiálů**
Studijní obor:	**Materiálové inženýrství**
Název tématu:	**Syntéza a vlastnosti nedopovaných a Er^{3+} dopovaných skel TeO_2-ZnO-BaO pro optické aplikace**
Zadávající katedra:	**Katedra obecné a anorganické chemie**

Zásady pro vypracování:

1) Zpracujte literární rešerši o sklech systému TeO_2-ZnO-BaO s důrazem na jejich strukturu, termické a optické vlastnosti.

2) Připravte objemová skla TeO_2-ZnO-BaO a odhadněte oblast sklotvornosti skel obsahujících 50-80 mol.% TeO_2.

3) Vybraná skla dotujte ionty Er^{3+} a tyto vzorky charakterizujte s ohledem na dosažení fotonové upkoverzní fotoluminiscence ve viditelné oblasti spektra.

4) Připravená skla charakterizujte z hlediska struktury, termických a optických vlastností. Získané výsledky diskutujte s literárními zdroji.

Rozsah grafických prací:

Rozsah pracovní zprávy:

Forma zpracování diplomové práce: **tištěná**

Seznam odborné literatury:

Podle pokynů vedoucího práce.

Vedoucí diplomové práce: **Ing. Lukáš Střižík, Ph.D.**
Katedra obecné a anorganické chemie

Konzultant diplomové práce: **prof. Ing. Tomáš Wágner, DrSc.**
Katedra obecné a anorganické chemie

Datum zadání diplomové práce: **28. února 2019**

Termín odevzdání diplomové práce: **10. května 2019**

L.S.

prof. Ing. Petr Kalenda, CSc.
děkan

prof. Ing. Zdeněk Černošek, CSc.
vedoucí katedry

V Pardubicích dne 12. února 2019

Prohlašuji:
Tuto práci jsem vypracoval samostatně. Veškeré literární prameny a informace, které jsem v práci využil, jsou uvedeny v seznamu použité literatury.
Byl jsem seznámen s tím, že se na moji práci vztahují práva a povinnosti vyplývající ze zákona č. 121/2000 Sb., autorský zákon, zejména se skutečností, že Univerzita Pardubice má právo na uzavření licenční smlouvy o užití této práce jako školního díla podle § 60 odst. 1 autorského zákona, a s tím, že pokud dojde k užití této práce mnou nebo bude poskytnuta licence o užití jinému subjektu, je Univerzita Pardubice oprávněna ode mne požadovat přiměřený příspěvek na úhradu nákladů, které na vytvoření díla vynaložila, a to podle okolností až do jejich skutečné výše.
Souhlasím s prezenčním zpřístupněním své práce v Univerzitní knihovně.

Beru na vědomí, že v souladu s § 47b zákona č. 111/1998 Sb., o vysokých školách a o změně a doplnění dalších zákonů (zákon o vysokých školách), ve znění pozdějších předpisů, a směrnicí Univerzity Pardubice č. 9/2012, bude práce zveřejněna v Univerzitní knihovně a prostřednictvím Digitální knihovny Univerzity Pardubice.

V Pardubicích dne

_____

Bc. Jan Hrabovský

ACKNOWLEDGEMENT

Foremost, I would like to express my sincere gratitude to my supervisor Ing. Lukáš Střižík, PhD. for the continuous support of my master study and research, for his patience, motivation and enthusiasm. His guidance helped me in all the time of research and writing of this thesis.

I would like to thank my advisor prof. Tomáš Wágner, CSc. for his support and motivation since the beginning of my scientific career.

Besides my advisor and supervisor, I would like to thank prof. Frédéric Smektala and Frédéric Desevedavy (University Bourgogne, ICB) for their motivation and guidance with this research in its very beginning.

I would also like to thank my colleagues who were involved in this research, namely to: doc. Ing. Luvík Beneš, Ing. Božena Frumarová, CSc., Ing. Stanislav Šlang, PhD., Ing. Petr Kalenda. PhD., Ing. Roman Svoboda, PhD., Ing. Vít Prokop, RNDr. Václav Dědič (MFF UK), Martin veis, PhD. (MFF UK), Gregory Gadret, PhD. (University Bourgogne, ICB) and to my friends, who helped me with final corrections: Robin Kryštůfek, Jiří Etrych and Monika Tran.

I thank to Center of Materials and Nanotechnologies for EDX analysis financially supported by the project CZ.1.05/4.1.00/11.0251 and by grant LM2015082 from Czech Ministry of Education, Youth and Sports of the Czech Republic.

Last but not least, I must express my very profound gratitude to my family and to my girlfriend for providing me with unfailing support and continuous encouragement throughout my years of study and throughout the process of researching and writing this thesis. This accomplishment would not have been possible without them.

Thank you
Jan Hrabovský

Název:

Syntéza a vlastnosti nedopovaných a Er^{3+} dopovaných skel TeO_2-ZnO-BaO pro optické aplikace

Anotace:

Předkládaná diplomová práce se zabývá studiem optických, strukturních a termických vlastností skelného systému TeO_2-BaO-ZnO (TBZ) a jeho vhodností pro dopování Er^{3+} ionty za účelem pozorování fotoluminiscenční emise při ≈1.5 μm a fotonové up-konverze ve viditelné a blízké infračervené oblasti elektromagentického spektra. Struktura připravených skel byla studována pomocí Ramanovy spektroskopie. S rostoucí koncentrací BaO a ZnO byl pozorován nárůst koncentrace TeO_{3+1} a TeO_3 strukturních jednotek, přičemž docházelo ke snížení počtu jednotek typu TeO_4. K tomuto chování docházelo v důsledku přerušování vazeb a nárůstu koncentrace nevazebných kyslíků (NBO). Termické vlastnosti byly studovány pomocí Diferenční termické analýza (DTA) a Diferenční skenovací kalorimetrie (DSC). Teplota skelné transformace rostla s vyšším obsahem BaO ve sklech a nižší koncentrací ZnO a TeO_2. Index lomu naopak s vyšší koncentrací ZnO a TeO_2 lineárně vzrůstal. Připravená skla jsou transparentní od viditelné do střední infračervené oblasti elektromagnetického spektra ($\lambda \approx 0{,}4–6$ μm). Vybrané vzorky napříč oblastí sklotvornosti byly následně dopovány 0,2 at.% Er^{3+}, avšak pouze složení $T_{80}B_{15}Z_5Er_{0.2}$, $T_{70}B_{25}Z_5Er_{0.2}$, $T_{60}B_{35}Z_5Er_{0.2}$ a $T_{60}B_{20}Z_{20}Er_{0.2}$ byla homogenní, a tedy vhodná pro další optické analýzy. Studované vzorky vykazovaly silnou $\lambda \approx 1550$ nm fotoluminiscenční emisi v blízké infračervené oblasti a fotonovou up-konverzi od blízké infračervené až do viditelné oblasti spektra. Pozorované intenzity intra-4*f* absorpčních pásů Er^{3+} iontů byly následně využity ke zjištění hodnot Judd-Ofeltových fenomenologických parametrů Ω_2, Ω_4 a Ω_6.

Připravené materiály ze skupiny TBZ skel se tak jeví jako aplikačně vhodné pro vláknovou optiku a konstrukci optických zesilovačů, vláknových laserů, senzorů a detektorů. Nicméně pro naplnění aplikačního potenciálu je žádoucí další studium jejich luminiscenčních vlastností.

Klíčová slova:

TeO_2-ZnO-BaO skla; sklotvornost; Er^{3+} dopovaná skla; fotoluminiscence; fotonová up-konverze

Title: Synthesis and properties of undoped and Er^{3+}-doped TeO_2-ZnO-BaO glasses for optical applications

Annotation:

This work deals with a systematic study of optical, structural and thermal properties of the TeO_2-BaO-ZnO (TBZ) glasses and their ability for doping with Er^{3+} ions in order to achieve the ≈1.5 μm Stokes photoluminescence and upconversion photoluminescence emission in visible and near-infrared spectral region. The structure of synthesized TBZ glasses was investigated by Raman scattering. It was found that with increasing BaO and ZnO content in TBZ glasses, the content of TeO_{3+1} and TeO_3 units increases at the expense of the TeO_4 units. This occurs as a consequence of increases non-bridgring oxygen (NBO) concentration. Thermal properties of studied glasses were investigated by the differential thermal analysis DTA) and differential scanning calorimetry (DSC). The glass transition temperature T_g increases with the increasing BaO content and decreasing concentration of ZnO and TeO_2. Refractive index of TBZ glasses linearly increases with increasing concentration of TeO_2 and ZnO. Prepared glasses are transparent from visible up to mid-infrared spectral region ($\lambda \approx 0.4$–6 μm). Selected glassy samples across the glass-forming region were doped with 0.2 at.% of Er^{3+} but only those containing higher concentration of BaO were homogenous: $T_{80}B_{15}Z_5Er_{0.2}$, $T_{70}B_{25}Z_5Er_{0.2}$, $T_{60}B_{35}Z_5Er_{0.2}$ and $T_{60}B_{20}Z_{20}Er_{0.2}$. These samples exhibit strong near-infrared photoluminescence at $\lambda \approx 1550$ nm and upconversion photoluminescence emission from visible to near-infrared spectra region. The intensities of Er^{3+} intra-4*f* electronic transitions were calculated on the basis of the Judd-Ofelt theory with derived phenomenological parameters Ω_2, Ω_4 and Ω_6.

The present study of the TBZ family glasses manifests their promising application potential in fibre optics for construction of optical amplifiers, lasers, sensors and detectors. However, further study of luminiscent properties is highly desirable for applications.

Key words:

TeO-ZnO-BaO glasses; glass-forming; Er^{3+} dopped glasses; photoluminesce; photon upconversion

TABLE OF CONTENS

SYMBOLS AND ABBREVIATIONS

Units

eV	electronvolt
Pa	Pascal
K	Kelvin
°C	degrees of Celsius
s	second
mol	mole
g	gram
J	Joule
µm	micrometer
nm	nanometer
µs	microsecond
ns	nanosecond
mol. %	mole percent

Abbreviations

$^{2S+1}L_J$	Spectroscopic term symbol. Symbol S denotes the total spin quantum number, 2*S*+1 represents the spin multiplicity, *L* is the total orbit quantum number and *J* denotes the total angular quantum momentum
4*f*	The ground state atomic orbitals with principal quantum number equal to 4 (n = 4) and azimuthal quantum number equals to three(l = 3).
4*f**	The excited state atomic orbital with principal quantum number equals to 4 (n = 4) and azimuthal quantum number equals to three (l = 3).
A(J,J')	Einstein's coefficient of spontaneous emission , [–]
A_{ED}	The probability of spontaneous emission for J↔J' electric dipole trnsition ,[s^{-1}]
A_{MD}	The probability of spontaneous emission for J↔J' magnetic dipole transition, [s^{-1}]
A_C, B_C, C_C	Cauchy coefficients (refractive index)
A_S, B_S, C_S	Sellmeier coefficients (refractive index)
A_T	Radiative transition probability

B_x	Material constant (Tauc absorption)
c	Speed of light, [ms^{-1}], c = 2,998·10^{8} ms^{-1}
LWAE	Long-wavelength absorption edge
DSC	Differential Scanning Calorimetry
e	Elementary charge of electron, [As], e = 1,602·10^{-19}As
E	Energy, [eV]
E_C	Energy od conductivity band, [eV]
E_F	Fermi energy, [eV]
E_g	Energy gap, [eV]
E_U	Urbach energy, [eV]
E_V	Energy of valence band, [eV]
E_{WAT}	Weak absorption tail energy, [eV]
EDX	Energy-dispersive X-ray spectroscopy
f_{cal}	Calculated oscilator strength of corresponding J↔J‘ electronic transition derived from phenomenological Judd-Offelt parameters, [–]
f_{exp}	Experimental strength of corresponding J↔J‘ electronic transition derived from experimentally obtained absorption/emission spectra, [–]
g	Electron *g*-factor, [–], g = 2,002
$\hbar$	Reduced Planck constant, [Js], $\hbar$ =1,054·10-34 Js,
$\hat{H}$	Hamiltonian
h	Planck’s constant, [m^{2}kgs^{-1}], h= 6,626·10^{-34} m^{2}kgs^{-1}
i	Imaginary unit
J, J‘	Total angular quantum momentum for ground state (*J*) and ecited state (*J‘)* corresponding to $\|L+S\|$ až $\|L-S\|$
k	Extinction coefficient
SWAE	Short-wavelength absorption edge
k_B	The Boltzmann constant, [m^{2}kds^{-2}K^{-1}]
l	Sample thickness, [m]
L, L‘	Total orbital quantum number
Ln^{q+}	Lanthanide atom in the q-th valency
m_1	Mass density of material measured in air, [kg]
m_2	Mass density of material measured in liquid, [kg]
m_e	Invariant electron mass, [kg], m$_e$ = 9,109·10^{-31} kg
MIR	Mid-infrared part of electromagnetic spectrum

M_2O	Monovalent cations oxides
MO	Divalent cations oxides
MSE	Mean squarred error
NIR	Near-infrared part of electromagnetic spectrum
n_p	Number of photons
n_r	Real part of complex refractive index
n_r*	Complex optical refractive index
PL	Photoluminescence
RE^{3+}	Trivalent eare earth ion
RMS	Root mean square
S, S'	Total spin quantum number represented as the sum of electon spins
s,p,d,f	Atomic orbitals
S_{ED}	Electric dipole strength of J↔J' electronic transitions, [cm^2]
SEM	Scanning electron microscope
S_{MD}	Magnetic dipole strength of J↔J' electronic transitions, [cm^2]
t	Time, [s]
T	Thermodynamic temperature, [K]
T_c	Crystalization temperature, [K]
T_g	Glass transition temperature, [K]
T_t	Melting temperature, [K]
$T_{ann.}$	Annealing temperature, [K]
$U^{(t)}$	Tensor operator of $4f \leftrightarrow 4f^*$ electronic transitions
T	Transmittance, [%]
TBZ	TeO_2-BaO-ZnO glasses
TBZ:Er	TeO_2-BaO-ZnO glasses doped with Er^{3+} ions
T.T.T.	Time-temperature-transforamtion diagram
UV	Ultraviolet part of electromagnetic spectrum
VIS	Visible part of electromagnetic spectrum
V	Volume, [m^3]
V_M	Molar volume, [m^3]
VASE	Variable angle spectroscopic ellipsometry
WAT	Weak absorption tail
XRD	X-ray diffraction
α	Absorption coefficient, [cm^{-1}]

α_0	Preexponential factor, [cm^{-1}]
α_M	Expansiton factor,
β (J J‘)	Branching ration of corresponding J↔J‘ electronic transition, [–]
η	Quantum yield of photoluminescence, [–]
λ	Wavelength, [*nm*]
λ_0	Mean wavelength of J ↔J‘ electronic transition, [nm]
λ_{exc}	Excitation wavelength, [nm]
λ_{em}	Emission wavelength, [nm]
π	Ludolf’s number, π = 3.141592654
σ	Absorption cross-section, [cm^2]
σ_{rms}	Standard deviation, [cm^2]
τ	Total lifetime, [s]
τ_{nr}	Nonradiative lifetime, [s]
τ_r	Radiative lifetime, [s]
τ_r^{JO}	Judd-Ofelt radiative lifetime calculated by Judd-Ofelt theory, [s]
$X_{ED,MD}$	Correction factors for the host matrix electric field at Ln^{3+} ions derived from Lorentz Force, [–]
Ψ,Δ	Ellipsometric parameters
ω	Angular frequency, [s^{-1}]
$\Omega_2, \Omega_4, \Omega_6$	Judd-Ofelt phenomenological parameters, [cm^2]

LIST OF FIGURES

LIST OF TABLES

1 INTODUCTION

Amorphous tellurites are attractive materials in photonics due to their broad optical window ranging from visible (0.5 μm) to mid-infrared (6 μm) spectral region, high linear and nonlinear refractive index, low phonon energies and high solubility of rare-earth ions. High thermal and mechanical stability as well as high chemical resistance against moisture, acids and alkalines, make them promising candidates for photonic applications [1–3].

Present work deals with the TeO_2–BaO–ZnO family glasses. Over literature [1–3], there were studied mainly binary TeO_2-MO (M = Ba or Zn) glasses. However, the deeper systematic study of the ternary TeO_2–BaO–ZnO glasses is missing although these glasses may be promising in photoluminescence applications [1–4]. The addition of divalent oxides (e.g. BaO, ZnO) to TeO_2 increases the glass-network connectivity of TeO_2–MO glasses and improves the chemical resistance [1] The content of the BaO and the ZnO, in the TeO_2–MO binary glasses may be up to ≈40 mol.% (BaO) and 45 mol.% (ZnO) respectively [5–7]. The addition of the BaO or ZnO to the TeO_2 decreases the refractive index and increases the glass transition temperature of glasses [1,5].

The present work deals with synthesis of TeO_2–BaO–ZnO ternary glasses in wide range of chemical compositions with respect to study their structural, thermal and optical properties. Selected glasses were doped with Er^{3+} ions in order to achieve the Er^{3+}: $^4I_{13/2} \rightarrow {}^4I_{15/2}$ ($\lambda \approx 1.5$ μm) emission and upconversion photoluminescence emission ranging from visible up to near-infrared spectral region. Obtained results allow to design the TBZ glasses of required properties, mainly for their optical applications such as manufacturing of optical fibers, amplifiers and waveguides.

2 THEORETICAL PART

2.1 Tellurite glasses

2.1.1 Introduction and general properties of glasses

Based on the long-range periodicity of solid-state structure, two main categories of materials may be recognized - amorphous or crystalline. Crystalline solids are arranged into a highly ordered microscopic structure over long atomic distances forming the so-called crystal lattice [8]. On the other hand, the lack of long-range order but preservation of the short-range order is typical for amorphous or non-crystalline solids [9].

The glassy materials are a special example of amorphous solids, which are isotropic with short-range periodicity and exhibit a glass transition [8]. Glasses may be formed in variety of materials with various chemical bonds (covalent, ionic, metallic, hydrogen). The conventional synthesis of glassy materials is a rapid quenching of the molten material below the melting temperature (T_m). The metastable state of glass between solid state and melting point T_m is known as supercooled liquid, where the atomic diffusion is limited due to increase in viscosity thus resulting in amorphous structure. Further cooling of the supercooled liquid reults in formation of long-term stable glassy solid. This process may be denoted as the general method for synthesis of glasses [9–11]. Slowing down of the cooling rate may lead to the formation of nucleation centers and their growth thus resulting in formation of the crystalline or semi-crystalline solid material. Volume tellurite glasses are mainly prepared via conventional melt-quenching technique to the preheated metal or carbon moulds with subsequent annealing [1]. Materials with different thermical parameters, such as temperature of glass transition, can be obtained by altering the rapidity of cooling. General example of glass fabrication is illustrated in Fig.1. [9–11]. During the time, three main criteria of glass formation were developed.

Kinetic criterion states that the glass may be prepared by cooling of any molten material upon the high cooling rate which must be higher than is the rate of crystallization (nucleation rate and growth of nuclei). However, in practice, the cooling rate for manufacturing of glass is limited [11].

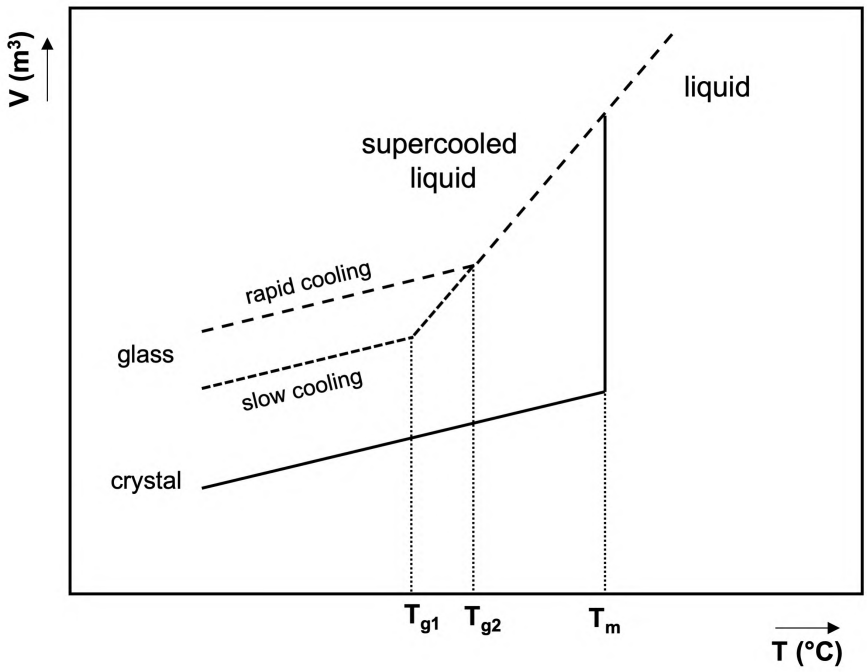

Fig. 1 Schematic diagram of glass preparation

Structural glass-forming criteria involve the characteristics of glassy structure with respect to ionic radii and coordination numbers of the central atom for simple oxides (Goldschmidt's theory [12]), number of bridging and non-bridging oxygen atoms per polyhedron (Stevelsov's theory [13]) or agrgregation of microcrystalline entities in disordered surrounding matrix (Lebededs theory [14]). Unfortunately, none of these mentioned structural theories is universaly valid. The most general structural theory was developed by Zachariasen [15], who identified two main glassy components: the glass-forming oxide (or network former) and the network modifier. Glass-forming A_xO_y-type oxide follows several rules: 1 – presence of a small number of oxygen atoms around A cation, 2 – non-sharing of oxygen atom by more than two A atoms, 3 – sharing of polyhedra via the corners, not via the edges or the faces and 4 – sharing of at least three corners of each polyhedron by the other surrounding polyhedra. The glassy modifiers usually break the network connectivity thus change the resulting properties of glass [15].

In addition to the previously mentioned criterion, several other theories of glass-forming ability exist (Dietzel, Stenworth, etc.) with different precision for specific kinds of glasses [11].

2.1.2 Tellurite Glasses

Tellurite glasses contain as their main structural component Tellurium dioxide (TeO_2), which is the most stable oxide in comparison with the other Te-based oxides (TeO, TeO_3). Melting temperature of TeO_2 is then ≈730 °C [16].

Synthesis of tellurite glasses was firstly reported during the 1950s [17–19] however, pure TeO_2 glasses were prepared almost ten years later via multistep synthesis by Chereminsinov *et al*. (1962) [1,20]. Moreover, it was found [1] that the addition of only a small amount of glassy modifier results in easier glass manufacturing due to lowering of the melting temperature. The TeO_2 glassy structure is built up of octahedral units with close-order faces configuration [18]. This configuration was found to be similar to those observed in the paratellurite α-TeO_2 crystals [1,21,25]. It has been concluded, that the octahedral structural units remain relatively unchanged during the transformation from crystalline to amorphous state [1,19]. Similar behavior was also observed in SiO_2 glasses built up from $SiO_{4/2}$ tetrahedra [22].

The existence of TeO_2 glasses seems to be in contradiction to the Zachariasen glass-forming criteria [15], due to proposed necessity of presence of tetrahedral units in the glassy network. It was concluded [1], that coordination complex with at least four atoms leads to formation of the following units: 1 – firmly shared polyhedra faces 2 – edge-shared polyhedra with one variable angle and 3 – corner-shared polyhedra with three variable angles. The presence of corner-shared polyhedra at the expense of edge-shared and face-shared polyhedra improves the glass formation of TeO_2 based glasses.

Above mentioned statements were later confirmed by using the XRD and Raman spectroscopy [23–25]. Results of these studies allowed to find the relationship between the Raman vibrational modes in paratellurite (α–TeO_2), β–TeO_2 and the pure TeO_2 glass. Later, two additional modification of TeO_2 (γ–TeO_2, δ–TeO_2) were also identified [26] and their influence on TeO_2 structure was discussed. Therefore, it can be assumed, that α–TeO_2 creates a three–dimensional (3D) network of infinite chains, which is mainly composed of TeO_4 trigonal bipyramids (tbs) connected at the corners. Remaining three modifications (β-TeO_2, γ-TeO_2, δ-TeO_2) are built up by disordered trigonal bipyramids of the $(Te_2O_6)^{4-}$ units as a result of accidentally shared edges [27,28].

Pure TeO_2 glass is then mainly built up by the TeO_4 units shared vertices (accidentally edges). The addition of modifiers into TeO_2-glasses results in formation of TeO_{3+1} units with one stretched axial bond Te–O or even in formation of TeO_3 trigonal pyramids (Fig.2) [25–29].

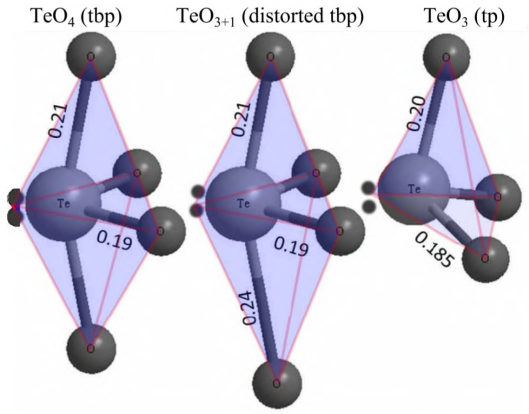

Fig. 2 Structure representation of TeO_4, TeO_{3+1} and TeO_3 units in tellurite glasses [1,25]

Tunability of properties in multicomponent tellurite glasses via the adjustment of chemical composition open the using of these materials in a variety of applications. Tellurite glasses are chemically resistant against moisture, acids and alkalines [17], possesses a high value of linear and nonlinear refractive index [30]. Moreover, they are highly transparent from UV (≈500 nm) to MIR (≈6 μm) spectral region with high solubility of rare-earth ions which make them attractive materials in photonics [31,32].

2.1.2.1 Properties of TeO_2 glasses

Pure tellurite glasses have density of about $\rho = 5.11$ g·cm^{-3} and molar volume $V_M = 31.29$ cm^3. Temperature of glass transition was determined as T_g = 320 °C. The color of prepared glasses is strongly composition-dependent. High-purity TeO_2 glass takes on very pale lime color and seems to be semitransparent. For other multicomponent glasses the color is strongly compositionally dependent and ranges from light to dark brown [1,33].

Amorphous TeO_2 glasses are synthesized from high purity TeO_2 powder in gold or platinum crucible. Using alumina crucible will cause diffusion of Al_2O_3 into the glass and its contamination [1]. Crucible with powder is placed into preheated furnace at 200 °C for ≈2 hours and then heated up to 900 °C with rate of 50 °C/min. In the next step the homogenized melt is heated at 900 °C for at least 30 min. Vitrification can be then performed using several techniques depending on weighted mass of the sample and cooling rate [1,34], such as splat quenching [35] or twin-roller technique [36]. Other possible procedures of pure TeO_2 preparation can be found in the literature [1].

2.1.2.2 Binary Tellurite glasses

Several complex studies of glass-forming properties of binary tellurite glasses containing monovalent (M_2O) and divalent cations (MO) [5] or transition metals oxides [1,37] were investigated in late 1970s. These works mainly described the dependence of refractive indices, densities and transmission spectra in corresponding concentration ranges. Structrual investigations using raman spectroscopy [29] and NMR [6] were later used for determination of structural units in glasses, where similar behavior to bivalent oxides was observed, which form disordered trigonal bipyramids (TeO_{3+1}) and trigonal pyramids (TeO_3). Besides that, results derived from NMR techniques describe linear increase in TeO_3 units concentration with addition of bivalent oxides up to 33.3 mol %. Further addition of MO rapidly increases their concentration and for concentrations in range 40–45 mol. % the glass structure contains almost exclusively TeO_3 units [6]. Observed local structure surrounding Te atoms was divided to five groups in connection to the structural units observed in tellurite crystals (Fig.3.) [6,7] as was already discussed in section 2.1.2. These isolated trigonal pyramids (TeO_3) may occur as a free anion in the structure or be connected through corners to other Te based polyhedron.

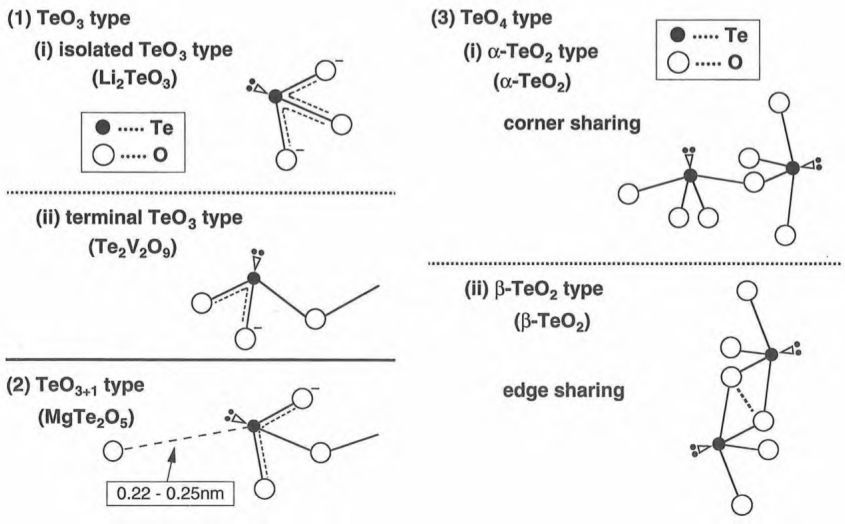

Fig. 3 Observed structural units in binary tellurite glasses [6,7]

Binary tellurites of TeO_2–BaO and TeO_2–ZnO systems are transparent from ultraviolet (≈500nm) to near infrared (≈6.5 μm) and their optical window does not shift significantly within their concentration ranges (Fig.4) [1,38].

Addition of zinc leads to increasing refractive index, third–order nonlinear susceptibility, chemical durability and lower thermal expansion more than for the rest of alkali metal oxides R_2O (R = Li, Na. K, Rb, Cs) and network intermediates MO (M = Zn, Mg, Ba and Pb) [1,39,40].

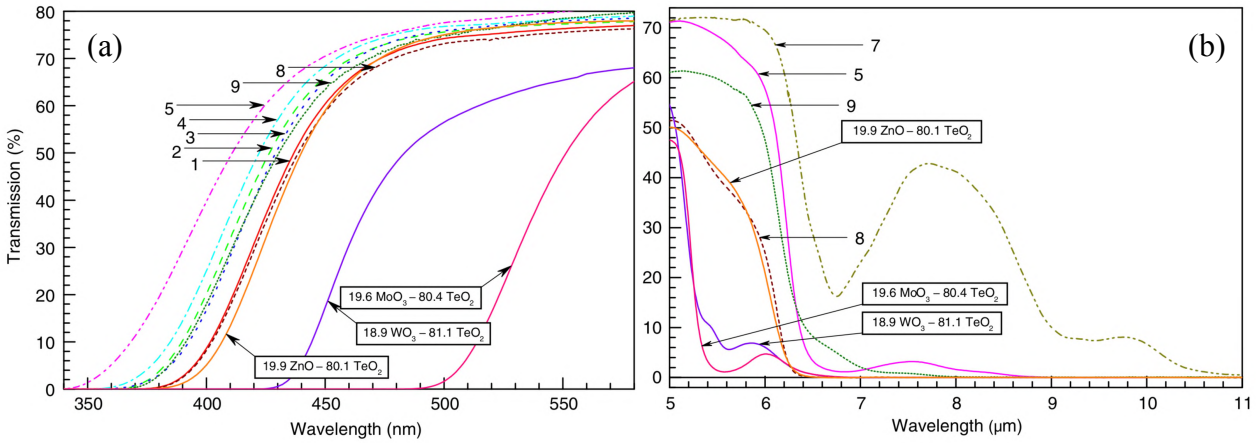

Fig. 4 Tellurite glasses transmission spectra near the short-wavelength edge (a) and the long wavelength edge (b). 1- $10BaCl_2$–10BaO–$80TeO_2$, 2- $15BaCl_2$–5BaO–$70TeO_2$, 3- $15BaCl_2$–25BaO–$60TeO_2$, 4- $20BaCl_2$–20BaO–$60TeO_2$, 5- $37BaCl_2$–18BaO–$45TeO_2$, 6- $40BaCl_2$–18BaO–$42TeO_2$, 7- $30BaCl_2$–30BaO–$40TeO_2$, **8- 20BaO–$80TeO_2$** and 9- $20BaCl_2$–$80TeO_2$ [38].

content up to 35 % can be prepared using copper mould (10 K/min) or roller technique (> 10^3 K/s). Partial glass-forming diagram is shown in Fig.5 [3].

Basic structural properties were investigated by *Mochida et al.* (1978) [44], who identified the concentration limit of ZnO in range 2.5–45.0 mol.%. Higher ZnO content leads to decrease in density (5.602 → 5.408 g/cm3) and refractive index (2.18 → 1.95). On the contrary, the temperature of glass transition increases slowly from about 300°C to almost 340 °C. Expansion coefficient factor (α_M) in the tellurite glasses with ZnO content was higher in comparison to silicate glasses (5.0 → 15.3) and increases more, than was observed in the samples modified with BaO [5]. This work was later extended and clarified by *Burger et al.* (1992) [3].

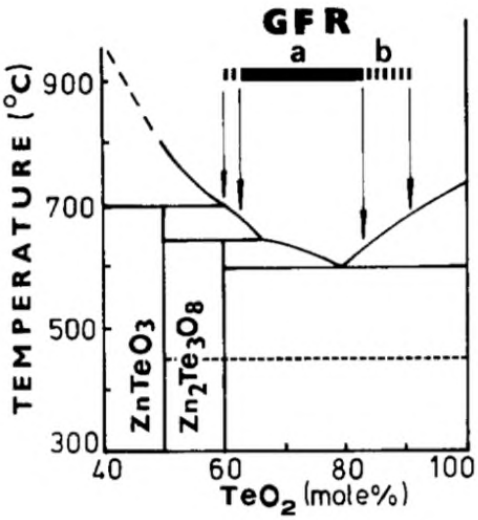

Fig. 5 Partial phase diagram of the system TeO_2–ZnO with illustrated limits at cooling rate (a)≈1 K/min (b) 10 K/min [3]

2.1.2.2.2 Binary TeO_2–BaO

The glass-forming ability of TeO_2–BaO system was investigated by *Mochida et al.* (1978) [44], who estimated the limit values of BaO concentration in range 2.5 – 35.8 mol.%. Higher BaO content decreases density (5.596 → 5.382 g/cm3) and refractive index (2.17 → 1.93) more rapidly than for glasses containing ZnO. On the other hand, the temperatures of glass transition increase more or less linearly from about ≈300 °C to almost ≈350 °C. Expansion coefficient factor (α_M) in the tellurite glasses modified with BaO was higher in comparison to silicate glasses (23.0 → 27.0) [5].

The structure of phase diagram of TeO_2–BaO system was investigated by *Nakashima et al.* (1988) [45] and later extended by *Mishra et al.* (2014) [46]. The partial cooling rates and composition diagrams were then experimentally determined in the composition range 50-100 mol % TeO_2. Results of these two works are shown in Fig.6. In this diagram, two main concentration ranges of glass forming were identified. Additionaly two time-temperature-transforamtion (T.T.T) diagrams for compostitions $80TeO_2$–20BaO (Fig.7a) and 65 TeO_2-35 BaO (Fig.7b) were estimated with shown curves of different cooling rates (C.C.T.). Increase of BaO content then leads to shift of crystallization curve towards shorter holding times and decreases the probability of glass formation [45,46].

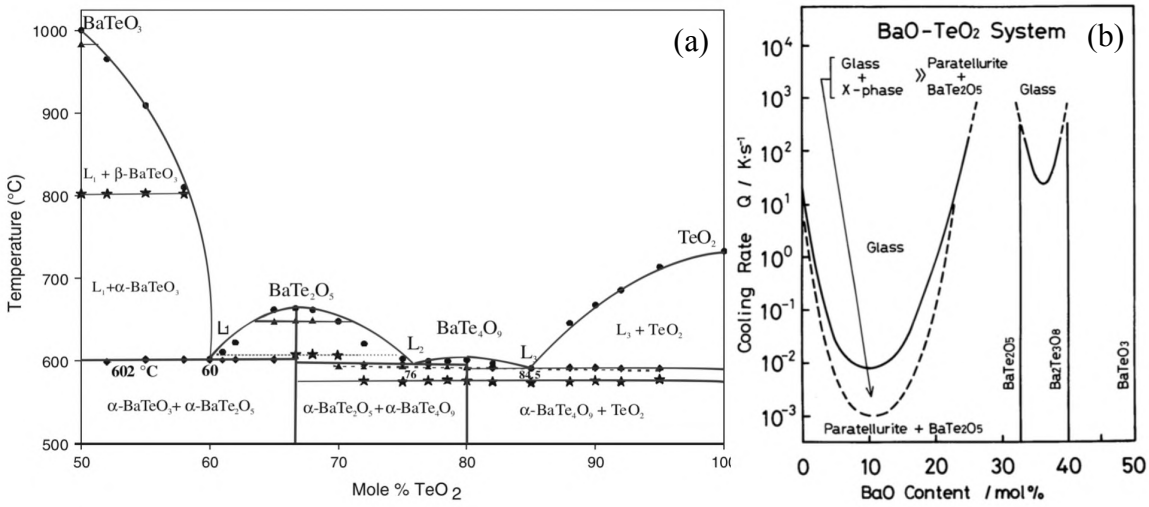

Fig. 6 Partial phase diagram (a) and influence of cooling rate to glass forming ability (b) for the system TeO_2-BaO [45,46]

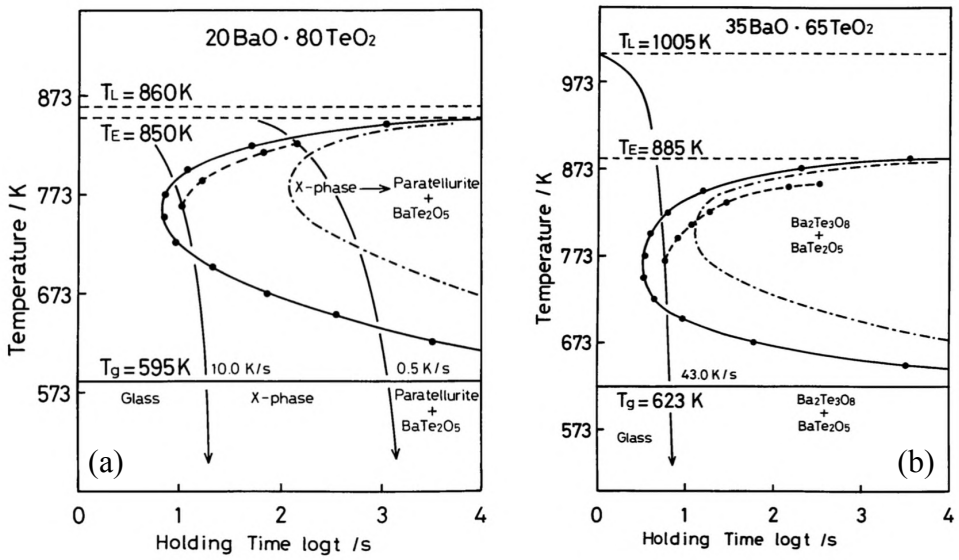

Fig. 7 Time-temperature-transforamtion diagram of (a) 80TeO_2–20BaO systém and (b) 65TeO_2-35BaO [45,46]

2.1.2.3 Ternary Tellurite glasses

2.1.2.3.1 TeO_2–BaO–ZnO glasses

First known investigation of TeO_2–BaO–ZnO (TBZ) system from the glass-forming ability point of view was made by *Imaoka et al.* (1968) [47]. This composite work describes glass formation ranges of binary and ternary tellurite glasses. Prepared glasses were synthesized in a gold crucible (85% Au + 15 % Pd) to avoid the interaction among the crucible and the molten materials at high temperatures above ≈1000 °C [47]. Obtained ternary glass formation range diagram of TBZ glasses is illustrated in Fig.8.

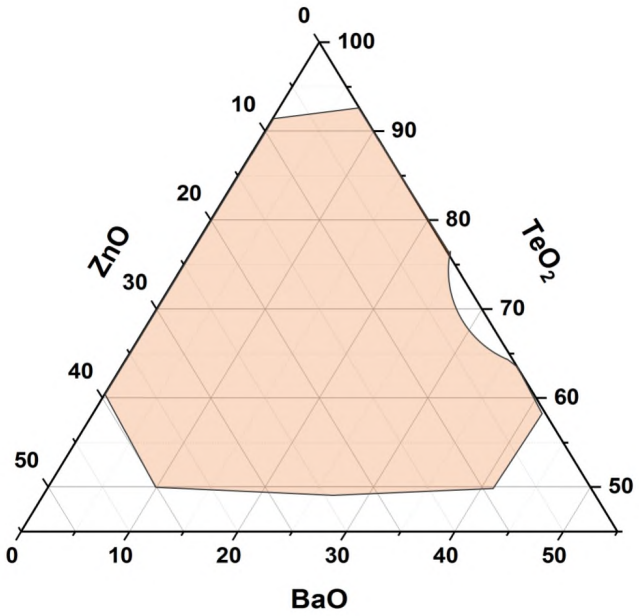

Fig. 8 Ternary diagram of glass formation range in the TeO_2–BaO–ZnO (TBZ) system [47]

The first publication describing thermal and optical properties of selected TBZ glasses was published by *Manikandan et al.* (2012) [4], who investigated the addition of BaO to binary TeO_2-ZnO system. Glasses of compositions (80-x)TeO_2–20ZnO–xBaO (x = 5, 10 15, 20 mol%) were prepared by the standard melt-quenching method in a gold crucible at 850 °C for 2 hours in flowing oxygen atmosphere. Homogenized molten material was then poured onto preheated metal plates ($T_{preheat}$ = 230 °C) and annealed below the glass transition temperature to remove residual stresses. It was found, that the addition of BaO improves the thermal stability and increases the glass transition temperature T_g [4]. Similar structural behaviour for TBZ glasses and binary TeO_2–BaO(ZnO) glasses was observed using Raman spectroscopy, where higher content of modifiers leads to the breaking of Te–O bonds and creation of NBO which results in increasing of the concentration of TeO_{3+1} and TeO_3 structural units. [4,6,29]. Prepared samples were transparent from 0.6 μm to 6 μm with observed absorption in MIR part of spectra due to the presence of hydroxyl (OH) groups. Refractive index was measured using variable angle spectroscopic ellipsometry (VASE) and corresponded with observation in binary glasses, where its decrease with the addition of modifiers was observed [4].

Work of Manikandan was in some way used for further investigation of thermal behaviour of TBZ glasses by *Zhou et al.* (2013) [48]. Several compositions located around the composition $T_{60}B_{20}Z_{20}$ in the central region of ternary TBZ diagram were synthesized under dry Redox balanced atmosphere in 5Au-95Pt crucible. Prepared samples were yellowish due to the diffusion of platinum from the crucible. Their temperatures of glass transition and crystallization have been measured using DSC and was observed, that the sample 60TeO_2-20BaO–20ZnO is the most stable from the thermal stability point of view [4]. Measured transmission spectra were comparable with works made with binary oxides [1,38]. Selected compositions were then optimized in combination with other compounds (Na_2O, BaCl, $ZnCl_2$) to reduce glass absorption in MIR. Obtained results were used for the preparation of bulk fibre preform and fibre drawing. Glass transformation temperature T_g exhibit the same behaviour as was observed in the work made by Manikadan et al. (2012) [4], while the crystallization temperature was not observed for all prepared samples [4,48].

Ternary (90-x)TeO_2–10ZnO–xBaO for $25 \leq x \leq 35$ glasses were later investigated by *Yasaka et. al* (2016, 2017) under two different synthesis conditions. In first work [49] the glasses were synthesized at 950 °C (1 hour, alumina crucible) and annealed at 350 °C, whereas the second work [50] used the temperature of 1100 °C. Density decreases from 5.34 to 5.29 g.cm^{-3} with increasing BaO content was observed and the amorphous state was

verified using XRD analysis. The optical band gap (E_g) was determined from Tauc's plot [9] and estimated to operate in range 2.73 → 2.78 eV following the higher BaO concentration.

Photoluminescence properties of TBZ glasses with respect to used RE^{3+} ions as the dopant were investigated for selected compositions by various works. Implantation of Dy^{3+} rare earth ions was firstly studied by *Boonin et al.* (2013) [51] for glass composition $15ZnO\text{-}5BaO\text{-}(80\text{-}x)TeO_2\text{–}xDy_2O_3$ and $1 \leq x \leq 8$, where three luminescence emission bands were observed under 450 nm excitation and assigned to Dy^{3+} electronic transitions: $^4F_{9/2} \rightarrow {}^6H_{15/2}$ (484 nm), $^4F_{9/2} \rightarrow {}^6H_{13/2}$ (575 nm) and $^4F_{9/2} \rightarrow {}^6H_{9/2}$ (661 nm). Radiative lifetimes of 575 nm emission were measured 0.117, 0.060, 0.018 and 0.012 ms for corresponding concentration 1, 3, 5 and 8 mol.% of Dy^{3+} ions. Losses for higher concentrations were assigned to increase of resonant energy transfer and cross relaxation [51]. Composition of 54TeO2–10ZnO–35BaO–1.0 Dy_2O_3 was investigated as a part of a more complex study of silver nanoparticles influence in TBZ glasses under 352 nm excitation [52]. Prepared glasses exhibit the same emission bands as the previously mentioned work.

Studies of photoluminescence properties of Er^{3+}-doped samples were made by *Yasaka et. al* (2016) [53] and *Gaafar et. al* (2017) [54]. Prepared Er-doped glasses of composition $(80\text{-}x)TeO_2\text{-}15ZnO\text{–}5BaO\text{–}xEr_2O_3$ for x = 0.0, 0.5, 1.0, 1.5 and 2.0 mol. % were synthesized in alumina crucible (850 °C, 30 min). Weak luminescence emission at 1550 nm originating from $^4I_{13/2} \rightarrow {}^4I_{15/2}$ was then observed in all prepared glasses under 980 nm (flash lamp) excitation and increased in connection with higher Er_2O_3 content [53].

More complex study was made by *Gaafar et al.* (2017) [54] in glass system $60TeO_2\text{-}(35\text{-}y)BaO\text{–}5ZnO\text{–}yEr_2O_3$, where y = 1.0, 2.5, 3.5, 4.0 and 5.0 mol. %. UV-NIR absorption spectra have been recorded to calculate three Judd-Ofelt phenomenological parameters. These three Judd-Ofelt phenomenological parameters then followed the $\Omega_2 > \Omega_6 > \Omega_4$ order in all prepared compositions. The calculated radiative lifetime of 1550 nm emission increased from 2.637 ms to 3.290 ms with the concentration of Er_2O_3 [54].

2.1.3 Optical properties

2.1.3.1 Optical transmission

Among the fundamental properties of amorphous solid-state materials are their optical transmission, known refractive index and luminescence properties. These attributes strongly related to the structural and electronic aspects of the material.

Amorphous tellurites transmit over a wide range of wavelengths from visible (VIS) to near- (NIR) and mid-infrared (MIR) spectral region, i.e. $\lambda \approx 0.5–6$ μm [1]. Their optical transmission in mid-infrared region is limited due to phonon absorption and is denoted as long-wavelength absorption edge (LWAE). Optical transmission is influenced by the concentration of impurities and related also to the refractive index of prepared materials via the Fresnel equations. Increase of refractive index is followed by increasing of reflectivity and thus corresponding decrease of transmittance. Optical absorption in amorphous semiconductors near the absorption edge is characterized by three types of transitions. Mentioned parts of SWAE are denoted as weak absorption tail, Urbach edge and Tauc absorption (Fig.9) [1,55,56].

2.1.3.1.1 Low absorption part – Weak absorption tail (WAT)

The weak absorption tail is observed below the exponential part of the absorption edge and follows the exponential law [9,59]. Values of absorption coefficient in the weak absorption tail part correspond to $\alpha(h\nu) \leq 10^{-1}$ cm^{-1}. The absorption losses are associated with localized tail states with transitions from tail-to-tail states. These localized states are created because of the presence of impurities in the material. Intrinsic defects originate directly from the material itself and can be associated with bond breaking or remaining internal stresses in the matrix. Defects of this type are strongly temperature dependent. On the other hand, extrinsic defects are caused by impurities consisting of aliovalent cations. The behaviour of extrinsic defect depends on impurity concentration which is constant with respect to changes in volume and independent of temperature. Material absorption can be represented using (1)

$$\alpha(h\nu) \propto \exp\left(\frac{h\upsilon}{E_{WAT}}\right) \tag{1}$$

where $\alpha(h\nu)$ is the absorption coefficient, $h\nu$ is the photon energy and E_{WAT} is the energy of weak absorption tail in range of about 10^{-1}–10^{-2} eV [9,55,56].

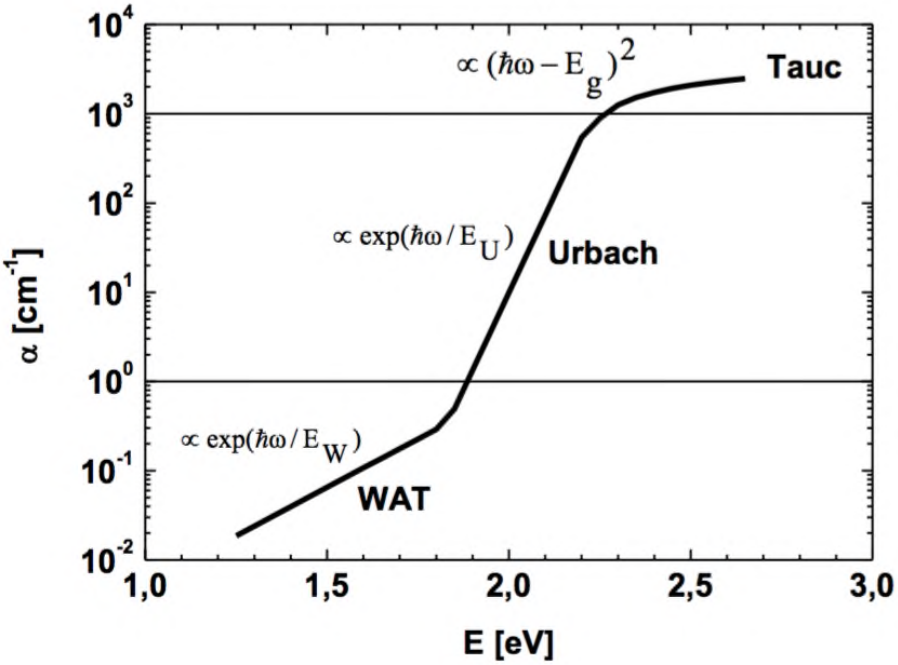

Fig. 9 Schematic illustration of the short wavelength absorption edge (SWAE) : weak absorption tail (defect states absorption), Urbach absorption (band-to-tail) and Tauc absorption (band-to-band absorption)

2.1.3.1.2 Middle absorption part – Urbach edge

The middle part of the short wavelength absorption edge is denoted as Urbach edge [57] and correspond to the absorption coefficient in the range $10^{-1} \leq \alpha \leq 10^4$ cm^{-1}. The optical absorption in the Urbach edge region is related to transitions from the localized tail states above the valence band edge to extended states in the conduction band [58]. Spectral dependence of absorption coefficient can be described using equation (2) known also as Urbach rule [57]. This equation can be expressed as

$$\alpha(h\nu) = \alpha_0 \exp\left(\frac{h\nu - E_g}{E_U}\right) \tag{2}$$

where E_g is the optical band gap energy, $h\nu$ is photon energy, α_0 is the preexponential factor and E_U represents Urbach energy. Urbach energy for amorphous semiconductors lies in the range of about 50–100 meV and is related to the breadth of the valence- or conduction-band tails states [58]. Temperature dependence of the absorption coefficient in the middle part of the short wavelength absorption edge (SWAT) can be expressed as

$$\alpha(h\nu) = \alpha_0 \exp\left(\frac{-\gamma(E_g - h\nu)}{k_B T}\right) \tag{3}$$

, where α_0 is the preexponential factor, γ is the material constant, k_B denotes Boltzmann constant and T is the thermodynamic temperature [9,55,56]

2.1.3.1.3 High absorption part – Tauc absorption

The High absorption part is an extension of the Urbach edge and expands further to the infrared part of the electromagnetic spectrum. Optical absorption is controlled by the band-to-band optical transitions. The absorption coefficient is higher than 10^3 cm^{-1} and can be calculated using Tauc's equation (4) [59]

$$\alpha(h\nu) = \frac{B_x(h\nu - E_g)^2}{h\nu} \tag{4}$$

where B_x is the material constant, $h\nu$ is the photon energy and E_g represents the optical energy gap. Better approximation for multicomponent glasses can be made using cubic relation, where the exponent in (4) is replaced by the number 3. One of the critical parameters is sample thickness. The correct value of absorption coefficient can be calculated from the transmission spectrum using equation (4) on a sample of thickness $\approx\alpha\ (h\nu)^{-1}$ [9,55,56].

2.1.3.2 Refractive index

The further important characteristic is the dispersion of light denoted as optical refractive index. Optical refractive index (n_r) can be defined as the ratio of the velocity of light in vacuum to its velocity in a specified medium [9,55]. This definition is expressed using formula (5)

$$n_r = \frac{c}{v} \tag{5}$$

Complex refractive index (n^*) can be then derived as a result of Maxwell equations (6). From this point of view, the refractive index is the frequency dependent quantity *n(v)* which describes

the interaction between the electric and magnetic field of substance environment and passing electromagnetic wave as the function of relative permittivity (ε_r) and relative permeability (μ_r) [9,60].

$$n_r^* = \sqrt{\varepsilon_r \mu_r} \tag{6}$$

In the first approximation, substances with a low magnetic field can be assumed to have relative permeability equal to one ($\mu_r = 1$) [9,60]. For light absorbing materials refractive index transform to complex variable n_r^*, which can be expressed using the following formula [9,55]:

$$n_r^* = n_r + ik \tag{7}$$

The real part of the complex refractive index then expressed the phase change of light passing throught the material and its imaginary part k describes the attenuation of this passing electromagnetic wave, i.e. absorption. Optical absorption coefficient $\alpha(h\nu)$ with respect to the wavelength of light can be described using formula (8) [9,55]

$$\alpha(h\nu) = \frac{4\pi k}{\lambda} \tag{8}$$

Spectral dependence of the real part of the refractive index n_r can be described by several empirical models. One of the most widely used models was developed by A.-L. Cauchy (1836). In this model, the refractive index obeys equation containing three Cauchy's coefficients A_C, B_C and C_C [9]:

$$n(\lambda) = A_C + \frac{B_C}{\lambda^2} + \frac{C_C}{\lambda^4} \tag{9}$$

Cauchy's model satisfactorily describes optical dispersion in the transparent area of electromagnetic spectra and can be easily applied to materials with normal dispersion. These ordinary systems exhibit gradual decreasing of the refractive index with longer wavelengths. For materials with more complex dispersion dependence in the infrared region of spectra was

derived following expression (10). This formula is also known as the Sellmeier equation [9,55,60]. Coefficient A_S represents absorption for shorter wavelengths of electromagnetic spectra and the sum with rest two remainign Sellmeier's coefficients B_S a C_S controls the shape of spectral dispersion.

$$n(\lambda)^2 = A_S + \sum_i \frac{B_{Si}\lambda^2}{\lambda^2 - C_{Si}} \tag{10}$$

Refractive index of pure tellurite glasses takes values of n ≈ 2 (λ = 632 nm). The refractive index also plays an important role in amorphous semiconductors doped with luminescence active compounds. There was observed, that a higher value of a refractive index increases the probability of radiative recombination [55].

2.1.4 Rare earth ions

The group of elements denoted as Rare Earth (RE) consists of seventeen chemical elements in the periodic table. Fifteen of them belong to lanthanides (La, Ce, Pr, Nd, Pm, Sm, Eu, Gd, Tb, Dy, Ho, Er, Tm, Yb, Lu) which are supplemented by Sc and Y [61,62].

All the elements of lanthanide series (Ln) form trivalent (Ln^{3+}) cations, which correspond to the electron configuration of Ln^{3+}: [Kr] $4d^{10}4f^{(2-14)}$ $5p^6 5s^2$ $5d^{(0-1)}6s^2$. Several exceptions exist, namely divalent Ln^{2+} (Nd^{2+}, Sm^{2+}, Eu^{2+}, Dy^{2+}, Tm^{2+}, Yb^{2+}) and quadrivalent Ln^{4+} (Ce^{4+}, Pr^{4+}, Tb^{4+}, Dy^{4+}) cations can be formed. Rare earth ions have a wide range of applications in electronics or in production of magnets, catalysts and glasses For these applications the trivalent Ln^{3+} cations are the most used [61,62].

Due to their characteristic optical and spectroscopic properties, many rare earth ions have been used in photonic application such as luminophores, lasers and amplifiers. The main benefit of rare earth ions is their spectroscopic resistance to surrounding host matrix. Emission bands originated from RE^{3+} ions in the host material are in good agreement with their characteristic energies, exhibit narrow spectral lines and large cross sections in a wide range of wavelengths from UV to MIR part of the electromagnetic spectrum. Luminescent properties of RE ions are determined by the 4f electrons and correspond to $4f \leftrightarrow 4f^*$ electronic transitions. This 4f shell is only weakly affected by the surrounding host matrix and offers well defined narrow spectral lines. This is in contrast to transition metals, which exhibit small cross sections and broad

spectral lines. This difference is mainly caused by the fact that 3d shells of transition ions are strongly affected by the host matrix, while 4f shells of lanthanides are well shielded. This screening is realized by partly filled outer shells of Ln^{3+} ions [61,62] (Fig.10).

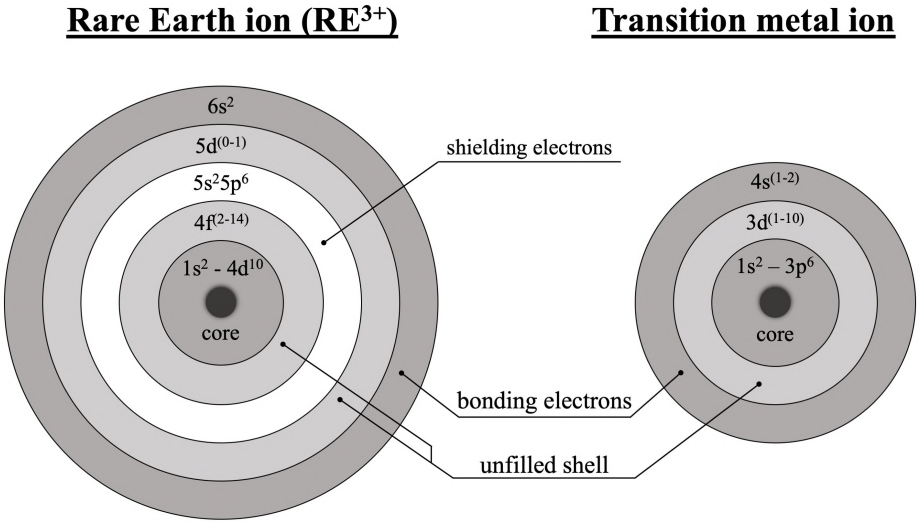

Obr.10. Rare Earth amd Transition metal ion structure

2.2 Luminescence

The luminescence is a process of spontaneous emission from an electronically or vibrationally excited species not in thermal equilibrium with its environment [63]. Radiative luminescent lifetime also has to be longer than the period of light oscillations (10^{-15} s). Based on the radiative lifetime length, two main processes can be identified: fluorescence ($\tau_{rad} < 10^{-5}$ s) and phosphorescence ($\tau_{rad} > 10^{-5}$ s) With respect to the excitation source can be the process of photon emission denoted as electroluminescence, chemiluminescence, photoluminescence, etc. [63–65].

2.2.1 Photoluminescence

Photoluminescence is light emission from any form of matter after the absorption of one or more incoming photons. The process is initiated by photoexcitation, when incoming photons excite electrons to a higher energy level [63]. The excitation wavelength is in most cases shorter than the emission wavelength due to thermal losses in the material. This process is denoted as Stokes law, where $\lambda_{ex} < \lambda_{em}$ [64,65]. The opposite process is called anti-Stokes law or upconversion, where the sequential absorption of two or more photons leads to the emission of light at a shorter wavelength than was the excitation wavelength. This sequential process is described by Ground-state-absorption/Excited-state-absorption (GSA/ESA) mechanism and

involves transitions on one atom. Other possible mechanisms of up-conversion and their combinations are also known and involve more than one luminescent centre, such as Energy transfer (ET), cooperative up-conversion, etc. [66]

With respect to the radiative lifetime, two main processes can be identified as fluorescence ($\tau_{rad} < 10^{-5}$ s) and phosphorescence ($\tau_{rad} > 10^{-5}$ s). Absorption of an incoming photon leads to excitation of an electron from the ground state to a higher energy level. Those excited electrons can be then present in a triplet or singlet state. In the triplet excited state, the electron has the same spin orientation to the other unpaired electron, whereas in the singlet state it has the opposite spin. Electrons occupiing ground state level are diamagnetic while the electrons in triplet states become paramagnetic. This difference in behaviour makes the radiative singlet-to-singlet transition more likely than triplet-to-singlet transition, because during triplet-to-singlet recombination change in the electronic state of electron must occur. For this reason, the lifetime of triplet state is longer than the singlet state. The transitions from the ground state to triplet state are also less probable and their absorption bands are less intense than singlet-to-singlet absorption. The excited triplet state can be then populated from the excited singlet state and leads to observed longer luminescent lifetimes. This phenomenon is called phosphorescence [64,65]

2.2.2 Recombination processes

Electron excited by incoming light is situated in a non-equilibrium state. This position is unstable and the electron has a tendency to emit redundant energy and deexcitate back to the ground state level. Realized recombination processes can occur independently and the total recombination rate can be determined as the combination of all contributions [64,65].

The transition from an excited state to a lower energetic state can be realized with the emission of luminescent energetic quanta (radiative relaxation). Alternatively, the energy can be released in form of phonons (nonradiative relaxation). Nonradiative relaxation occurs when the energy difference between the levels is very small and faster than the radiative recombination. The transition probability is then expressed as (11) [9,64,65].

$$\frac{1}{\tau} = \frac{1}{\tau_r} + \frac{1}{\tau_{nr}} \tag{11}$$

where τ is the total luminescence lifetime, τ_r is the radiative lifetime and τ_{nr} is the nonradiative lifetime. The quantum efficiency η is then represented as the ratio between radiative luminescence lifetime to the total recombination lifetime (12). Superior luminescent properties are connected with a higher value of quantum efficiency [64,65].

$$\eta = \frac{\tau}{\tau_r} \tag{12}$$

2.3 Judd-Ofelt theory

Judd-Ofelt theory (JO) was invented in 1962 by Brian R. Judd [67] and George S. Ofelt [68] independently on each other. This theory describes the spectroscopic properties of trivalent Ln^{3+} ions in different kinds of solid or liquid host matrices.

Judd-Ofelt theory describes the $4f \leftrightarrow 4f^*$ electronic transitions intensities of RE^{3+} ions influenced by the surrounding ligand field. These 4f electrons are well shielded by 5s and 5p electrons which leads to the very weak interaction between these optical active electrons and host matrix. Perturbation of the environment then manifests itself in the Hamiltonian of RE^{3+} free ion and leads to the creation of Stark levels [62,67–70]. The Hamiltonian of free RE^{3+} ion can be expressed as (13)

$$\hat{H}(x,t) = -\frac{\hbar}{2m}\sum_{i=1}^{N}\nabla_i^2 - \sum_{i=1}^{N}\frac{Ze^2}{r_j} + \sum_{i<j}^{N}\frac{Ze^2}{r_{ij}} + \sum_{i=1}^{N}\xi(r_i)(s_i l_i) \tag{13}$$

where the first two terms on the right-hand side of the equation represent nucleus-electron interaction (H_0), the third term is the coulombic repulsion (H_{el}) and the last term represents spin-orbit interaction (H_{SO}). The interaction among the ion and surrounding ligand field (perturbation) is expressed by one additional term H_{lf} [69,70]. More terms describing lattice phonons or electromagnetic field can be used, but they were not included in this model [61,62].

The electrostatic interaction between electrons (Coulombic repulsion) causes the splitting of energy levels of the order of 10^4 cm^{-1} and form new ^{2S+1}L energy levels of 10^4 cm^{-1} mutual distances. Further energy levels splitting occurs when spin-orbit interactions are included ($^{2S+1}L_J$). Influence of ligand field perturbation then leads to the creation of Stark levels and the process is labelled as Staks splitting. During Stark splitting each J level is split to 2J+1 new stark levels with energy separation of ~ 10^2 cm^{-1}. Used spectroscopic symbols represent total

spin (S), total orbital angular momentum (L) and total angular momentum J, where J = S+L. Process of stark splitting is illustrated in Fig.10 [61,62,69].

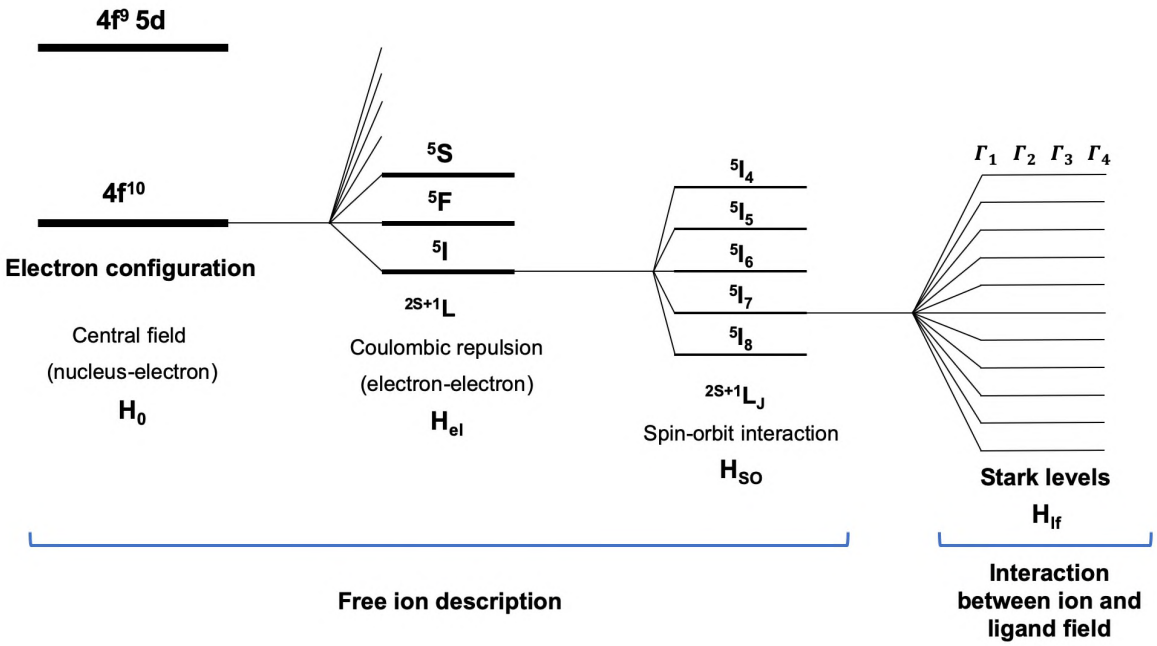

Fig. 10 Electron interaction in the host matrix

For isotropic materials, the electric (S_{ED}) and magnetic (S_{MD}) transition strengths of J ↔ J´ electronic transition are given by (14) a (15) [61,62,69]

$$S_{ED}(J,J') = e^2 \sum_{t=2,4,6} \Omega_t \left| \left\langle f^F [SLJ] \| U^{(t)} \| f^F [S'L'J'] \right\rangle \right|^2 \tag{14}$$

$$S_{MD}(J,J') = \frac{e^2\hbar^2}{4m_e^2c^2} \sum_{t=2,4,6} \Omega_t \left| \left\langle f^F [SLJ] \| L + gS \| f^F [S'L'J'] \right\rangle \right|^2 \tag{15}$$

, where e is the elementary charge, $\hbar$ is the reduced Plancks constant, c is the speed of light in vacuum, g is the electron g-factor and symbol Ω_t for t = 1, 2, 3 represents three phenomenological Judd-Ofelt parameters. The term on the right-hand side of the equation is double reduced matrix element of J↔J´ transition with corresponding tensor operator $U^{(t)}$. This tensor operator is independent to the chosen host matrix and its components are tabulated.

Interaction between the surrounding host matrix and Ln^{3+} ions are then expressed by three phenomenological Judd Ofelt parameters. From the known electrical and magnetical dipole forces and JO phonomenological parameters can be further calculated the oscillator strength f_{cal} of J↔J′ transition. Calculated oscillator strength represents the ratio between absorbed (emitted) and emitted (absorbed) intensity of electomagnetic radiation for harmonically oscilating electron and expressed the probability of individual J ↔ J′ transitions. Determination of calculated oscillator strength fcal can be written as [69]:

$$f_{cal}(J,J') = \frac{8\pi^2 m_e c}{3he^2(2J+1)\lambda_0}\left[X_{ED}S_{ED}(J,J') + X_{MD}S_{MD}(J,J')\right] \tag{16}$$

where h is the Planck's constant, J is the total angular momentum of corresponding energetic state, λ_0 is the mean wavelength of corresponded J ↔ J′ transition and X_{ED} together with X_{MD} represent the correction factors, which describe the influence of electromagnetic field on Ln^{3+} ions. Evaluation of these two correction factors for J → J′ absorption can be made using formulae (17) and (18) [61,62,69]. The J′→ J emission transition can be then obtained by multiplying the two previous equations by the material refractive index to the second power.

$$X_{ED} = \frac{\left(n^2-2\right)^2}{9n} \tag{17}$$

$$X_{MD} = n \tag{18}$$

Experimental oscillator strength f_{exp} can be derived from known values of absorption coefficient α(hν) by the integration over the J → J′ transition spectral range (19), where ρ is the Ln^{3+} concentration in unit volume and ε_0 is the permittivity of vacuum. Using the equality assumption, that the experimental oscillator strength is equal to the calculated oscillator strength ($f_{exp} = f_{cal}$), then leads to the introduction of the relationship between fitted absorption spectra and JO phenomenological parameters (20) [61,62,69]. Transitions J ↔ J′ with low contribution or absence of magnetic dipole forces reduce the equation (20) to the new form,

where the last element on the righ side is zero. Accuracy of the fit is determined by the mean square error (21) [61,69].

$$f_{\exp}(J,J') = \frac{4m_e c^2 \varepsilon_0}{\rho e^2 \lambda_0} \int_J^{J'} \alpha(h\nu) d\alpha \tag{19}$$

$$S_{ED}(J,J') = \frac{3\varepsilon_0 ch(2J+1)}{2\pi^2 \lambda_0 \rho X_{ED}} \int_J^{J'} \alpha(h\upsilon) d\alpha - \frac{X_{MD}}{X_{ED}} S_{MD}(J,J') \tag{20}$$

$$\sigma_{rms} = \sqrt{\sum_{j=1}^{Y} \left(S_j^m - \sum_{i=1}^{3} Y_{i,j} \Omega_i \right)^2} \tag{21}$$

where Y_{ij} are the elements of matrix $U^{(t)}$ of order Y×3 and for t ∈ (2, 4, 6). Terms Ω_i are the elements of matrix size 1×3 describing the Judd-Ofelt phenomenological parameters Ω_t and t = 2, 4 a 6. The parameters Ω_2, Ω_4 and Ω_6 can be now used to obtain radiative transition probabilities of spontaneous emission A(J′→J), (Einsten coefficient) of electric dipole transitions between the excited states and lower-lying energetic levels of Ln^{3+} ions (22). The sum of the reciprocal Einstein's coefficient of spontaneous emission than gives the theoretically predicted value of the radiative lifetime τ_r^{JO} (23) [62,69]

$$A(J,J') = \frac{16\pi^3 n^2}{3h\varepsilon_0 (2J'+1)\lambda_0^3} \left(X_{ED} S_{ED} + X_{MD} S_{MD} \right) \tag{22}$$

$$\tau_r^{JO} = \sum_J \frac{1}{A(J,J')} \tag{23}$$

The luminescence branching ratio β(J′,J) is given by (24) and represents the distribution of the emission transitions in the emission spectra. Using theoretical JO lifetime and branching ratio in combination with experimentally measured lifetime for assigned transition leads to equation (25), which describes the radiative quantum yield of corresponding J′→J electronic transition [62,69].

$$\beta(J,J') = \frac{A(J,J')}{\sum_{J} A(J,J')} \tag{24}$$

$$\eta = \frac{\tau}{\tau_r^{JO}}\ \beta(J,J') \tag{25}$$

3 EXPERIMENTAL PART

3.1 Preparation methods

3.1.1 Preparation of ternary TBZ glasses

TeO_2-BaO-ZnO (TBZ) glasses were synthesized from high purity compounds of TeO_2 (4N), BaO (4N) and ZnO (4N) with a total batch weight of 5.5 g. Calculated quantities of each compound were mixed and grinded in platinum or alumina crucible. The platinum crucible was purified before the synthesis by its immersion into hydrofluoric acid for 24 hours.

Starting compounds loaded in the platinum crucible were melted in an electrically heated furnace under an air atmosphere at the temperature of ≈900 °C for 15 min. Homogenized melt was quenched into the preheated brass mould and annealed for 4 hours at the temperature of 20 °C below the glass transition temperature to remove the residual internal stress. The mould preheating temperature ($T_{preheat}$) was set to 270 °C for each composition and was later modified for selected samples which could not be prepared in one piece due to remaining internal stresses. For these samples, the synthesis temperature was set selectively as $T_{preheat} = T_g - 20$ °C. This procedure was employed mainly for compositions located near the glass formation border. Compositions prepared in alumina crucible were quenched into the preheated carbon moulds ($T_{preheat}$ = 300 °C) and annealed for at least 5 hours on the hotplate (300 °C). Undoped glasses prepared in the platinum crucible have yellowish colour contrary to the fully transparent colourless glasses prepared in an alumina crucible. Dimensions of the prepared samples were approximately 4×20×10 mm^3.

The chemical compositions of the TeO_2-BaO-ZnO synthesized glasses were chosen with respect to investigate the basic physico-chemical properties over the glass-forming region. One selected glass of the $(TeO_2)_{60}(BaO)_{20}(ZnO)_{20}$ chemical composition was synthesized using both platinum or alumina crucible in order to compare the thermal properties (glass transition temperature and crystallization temperature). Chemical compositions of synthesized glasses are presented in Table 1 with their labelling. For better clarity, the obtained glassy and crystalline samples in TBZ system is presented in ternary diagram in Fig.11.

Tab. 1. Theoretical chemical compositions of prepared TeO_2-BaO-ZnO glasses

Notation	TeO_2 (mol. %)	BaO (mol. %)	ZnO (mol. %)
$T_{90}B_5Z_5$	90	5	5
$T_{80}B_{10}Z_{10}$	80	10	10
$T_{70}B_{15}Z_{15}$	70	15	15
$T_{60}B_{20}Z_{20}$	60	20	20
$T_{55}B_{22.5}Z_{22.5}$	55	22.5	22.5
$T_{50}B_{25}Z_{25}$	50	25	25
$T_{80}B_5Z_{15}$	80	5	15
$T_{80}B_{15}Z_5$	80	15	5
$T_{70}B_5Z_{25}$	70	5	25
$T_{70}B_{25}Z_5$	70	25	5
$T_{60}B_0Z_{40}$	60	0	40
$T_{60}B_5Z_{35}$	60	5	35
$T_{60}B_{10}Z_{30}$	60	10	30
$T_{60}B_{15}Z_{25}$	60	15	25
$T_{60}B_{25}Z_{15}$	60	25	15
$T_{60}B_{30}Z_{10}$	60	30	10
$T_{60}B_{35}Z_5$	60	35	5
$T_{55}B_5Z_{40}$	55	5	40
$T_{55}B_{10}Z_{35}$	55	10	35
$T_{55}B_{15}Z_{30}$	55	15	30
$T_{55}B_{20}Z_{25}$	55	20	25
$T_{55}B_{25}Z_{20}$	55	25	20
$T_{55}B_{30}Z_{15}$	55	30	15
$T_{55}B_{35}Z_{10}$	55	35	10
$T_{52.5}B_{22.5}Z_{25}$	52.5	22.5	25
$T_{52.5}B_{25}Z_{22.5}$	52.5	25	22.5
$T_{55}B_0Z_{45}$ - crystalline	52.5	25	22.5
$T_{60}B_{40}Z_0$ - crystalline	52.5	25	22.5
$T_{60}B_{20}Z_{20}$ -Al_2O_3 crucible	60	20	20

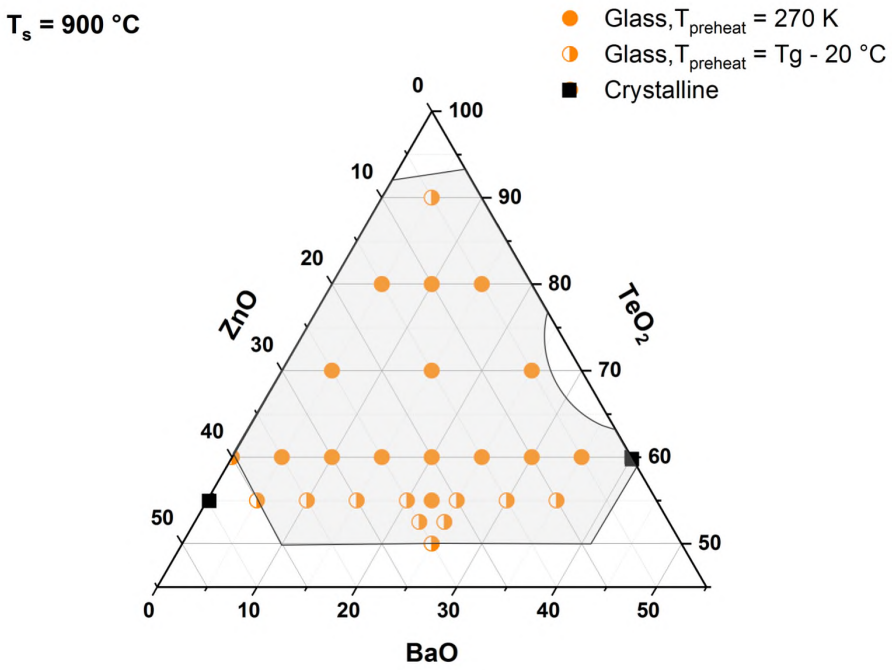

Fig. 11 Ternary diagram of prepared TeO_2-BaO-ZnO (TBZ) glasses (markers) and glass formation region found by *Imaoka et al.* (1968) [47]

3.1.2 Preparation of doped TBZ glasses

0.2 at.% Er^{3+}-doped TeO_2-BaO-ZnO glasses were synthesized from high purity compounds of TeO_2 (4N), BaO (4N), ZnO (4N) and Er_2O_3 (3N). Calculated quantities of each compound have been mixed and grinded together. The synthesis was performed in alumina crucibles.

Weighted mixture has been melted in electrically heated furnace under air atmosphere conditions at temperature of 900 °C for 15 min to homogenize the melt and then quenched into the preheated carbon mould of about 300 °C. Glasses were then annealed to remove residual internal stresses on preheated hot plate at the temperature of T_g – 20 °C. Each sample was annealed for at least 5 hours and then slowly cooled down to laboratory temperature. Glasses doped with Er^{3+} ions are pink coloured contrary to colourless (alumina crucible) or yellowish (platinum crucible) undoped samples.

Samples prepared via melt quenching method under conditions described above were designed to investigate the glass-forming ability and solubility Er^{3+} ions in TBZ glassy system. Theoretical chemical compositions of synthesized glasses are presented in Tab.2 with their labelling. Fig12 represents the glass formation in the TBZ:Er glasses. Samples $T_{80}B_{15}Z_5$:$Er_{0.2}$, $T_{70}B_{25}Z_5$:$Er_{0.2}$, $T_{60}B_{35}Z_5$:$Er_{0.2}$ and $T_{60}B_{20}Z_{20}$:$Er_{0.2}$ were fully transparent, the rest of the samples was opaque.

Tab. 2 Theoretical chemical compositions of prepared 0.2 at.% Er-doped TeO_2-BaO-ZnO glasses

Sample ID	Notation	TeO2	BaO	ZnO	Er
D1 - cryst	$T_{80}B_5Z_{15}:Er_{0.2}$	80	5	15	0.2
D2	$T_{80}B_{10}Z_{10}:Er_{0.2}$	80	10	10	0.2
D3	$T_{80}B_{15}Z_5:Er_{0.2}$	80	15	5	0.2
D4	$T_{70}B_5Z_{25}:Er_{0.2}$	70	5	25	0.2
D5	$T_{70}B_{15}Z_{15}:Er_{0.2}$	70	15	15	0.2
D6	$T_{70}B_{25}Z_5:Er_{0.2}$	70	25	5	0.2
D7 - cryst	$T_{60}B_5Z_{35}:Er_{0.2}$	60	5	35	0.2
D8	$T_{60}B_{20}Z_{20}:Er_{0.2}$	60	20	20	0.2
D9	$T_{60}B_{35}Z_5:Er_{0.2}$	60	35	5	0.2

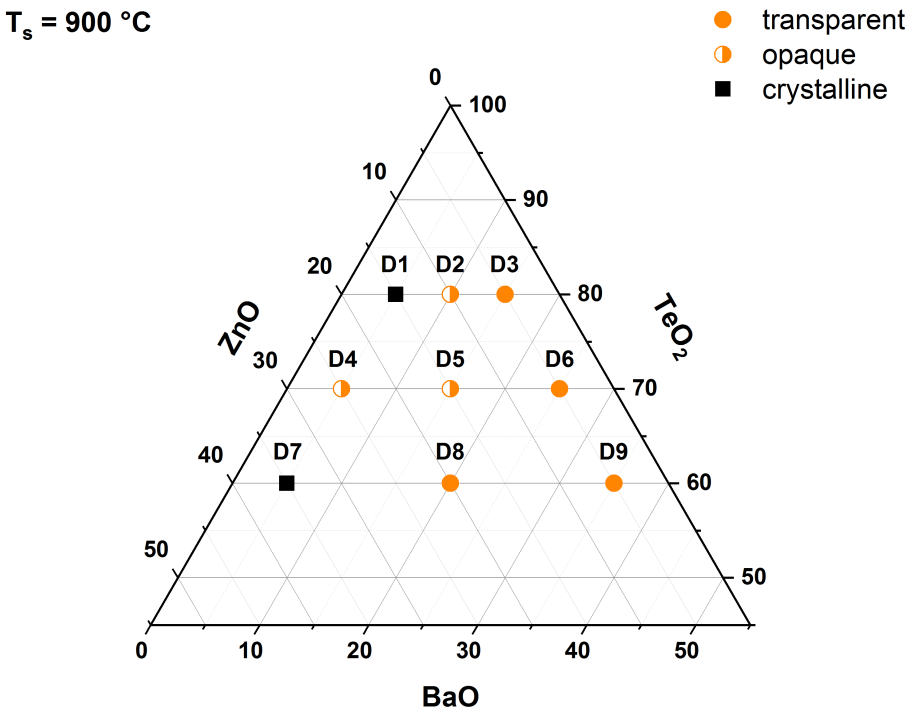

Fig. 12 *Ternary diagram of prepared TeO_2-BaO-ZnO:0.2 at.% Er (TBZ:Er) glasses*

3.2 Characterization methods

The diffraction patterns (Cu $K\alpha$, $\lambda = 1.5418$ Å) were recorded on powdered samples using D8 Advance diffractometer (Bruker AXS, Germany) with Bragg-Brentano θ-θ goniometer equipped with Ni-beta filter and LynxEye detector. The scan was performed at room temperature in the range of 2θ from 5° to 90° with a step of 0.01° and counting time of 2 s per step.

Chemical composition of prepared glasses was verified by scanning electron microscope Lyra 3 (Tescan) with EDX analyser AZtec X-Max 20 (Oxford instruments) with 20 kV voltage on polished samples at three different points on the area of about ≈400×400 μm^2. For measurements, the samples were coated with a carbon film.

Raman scattering spectra were measured using a Dimension P2 system (Lambda Solution, USA). Spectra were excited with a laser operating at $\lambda = 532$ nm. Reduction of Raman spectra of measured samples was carried out using the Gammon–Shuker reduction [71] and decomposed with 8 Voight functions [72].

Thermal properties of the glasses were studied with the STA 449 F5 (Netzsch) operating in DTA a heating rate of 10 °C.min^{-1} over the temperature range 25 – 650 °C. The measurements were carried out with approximately 100 mg of the bulk sample in the alumina crucible under inert nitrogen atmosphere.

The densities of all prepared samples were estimated using the Archimedes' method according to the Eq. 27. Distilled water was used as a reference liquid

$$\rho_S = \frac{\rho_l m_1}{m_1 - m_2} \tag{26}$$

where ρ_S is the density of prepared glass, ρ_l is the density of distilled water, m_1 is the weight of glass in the air and m_2 is the weight of glass immersed in distilled water. In the case of Er-doped TBZ glasses, the density was used for estimation of the total concentration of Er^{3+} ions per unit volume.

Refractive index measurements were carried out on polished glassy blocks of the thickness of about ≈4 mm using the variable angle spectroscopic ellipsometer made by J.A.Woollam, Co., Inc. in the spectral range 200–1800 nm. Measured spectra were fitted using the Tauc-

Lorentz oscillator [73,74] with inclusion of surface roughness according to the effective medium approximation [75].

Undoped TBZ glasses were also investigated using prism (TiO_2) coupled refractometry (PCR) at the three different wavelengths of λ = 632, 1064 and 1550 nm.

The optical transmittance spectra were recorded using the UV-Vis-NIR spectrophotometer Jasco V-570 in the wavelength range of 250–2500 nm or Shimadzu UV3600+ spectrophotometer in the wavelength range of 200–1750 nm. The transmittance in infrared spectral region was measured by the infrared spectrophotometer BRUKER Vertex 70v/80v in the spectral range of 2300-7000 nm. Area of the absorption bands of Er^{3+} $4f \rightarrow 4f^*$ electronic transitions was integrated in program Fityk v.0.8.9 by a set of Gaussian functions.

Corresponding absorption cross sections were calculated using the formula:

$$\sigma = \ln 10[-\log T_S + \log(1 - R)]/\rho d, \tag{27}$$

where T_S is transmittance, R reflectance, ρ is the concentration of Er^{3+} in prepared glasses and d is the sample thickness. Determined absorption cross-section spectra and refractive index of glasses were used for application of the Judd-Ofelt theory to determine the intensities of $4f$ electronic transitions by using the program JOF v.2.3.win [69].

Photoluminescence spectra were measured using the tunable Ti:sapphire laser Spectra Physics 3900s as excitation source and recorded by the FTIR spectrometer Bruker equipped with Ge or MCT nitrogen colled detector. Upconversion emission spectra were excited using the 975 nm fibre laser and recorded by the OceanOptics USB4000 spectrophotometer.

4 RESULTS AND DISCUSSION

4.1 General study of ternary TeO_2-BaO-ZnO (TBZ) glass system

4.1.1 X-ray diffraction (XRD) analysis

The amorphous state of prepared TeO_2-BaO-ZnO glasses was verified using the X-ray diffraction (XRD) analysis. XRD diffractograms are presented in Fig. 14. All the samples, except that $T_{60}B_{40}Z_0$, show typical "halo" from which may be judged on their amorphous structure [76].

The XRD pattern of crystalline $T_{60}B_{40}Z_0$ sample is shown in Fig.13. Observed diffraction peaks were assigned to triclinic $Ba_3Te_4O_{11}$ (space group P-1) and orthorhombic $BaTeO_3$ (space group Pnma)) phases standards from PDF-4+ database [77]. Formation of the $BaTeO_3$ crystalline phase in $T_{60}B_{40}Z_0$ sample corresponds to work [78].

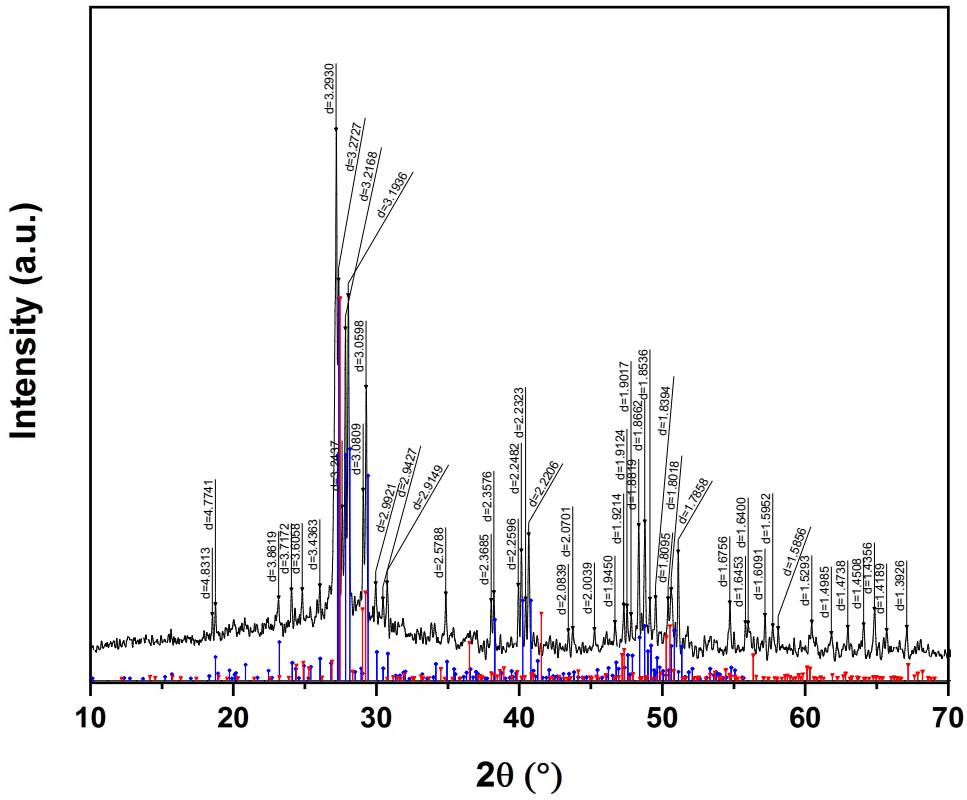

Fig. 13 The XRD pattern of sample $T_{60}B_{40}Z_0$ with identified and assigned diffraction peak to $Ba_3Te_4O_{11}$ (triclinic) and $BaTeO_3$ (orthorhombic) structure units.

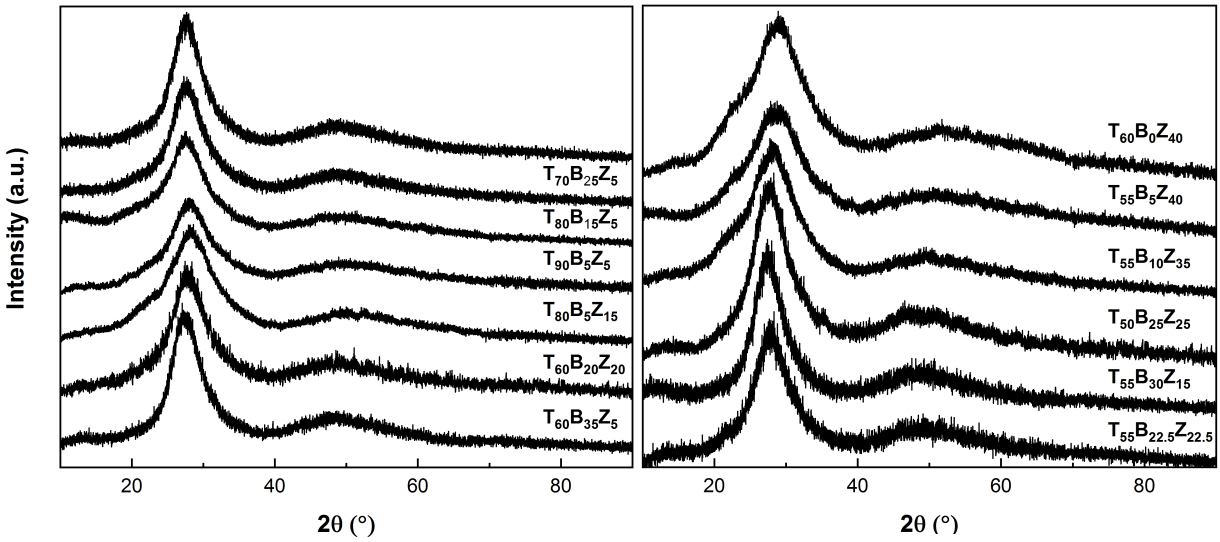

Fig. 14 The XRD patterns of prepared TeO_2-BaO-ZnO glasses

4.1.2 Raman spectroscopy

The structure of selected compositional series in the TBZ glassy system have been studied by Raman scattering in Raman shift wavenumber range of 50-1000 cm^{-1}. The compositional series were $T_{85-x}B_xZ_5$ or $T_{85-x}B_5Z_x$, where x = 5, 10 or 15 mol.%, and $T_{100-y}B_{y/2}Z_{y/2}$, where y = 20, 30 or 40 mol.%. Reduced Raman spectra for all studied samples are presented in Fig.15.

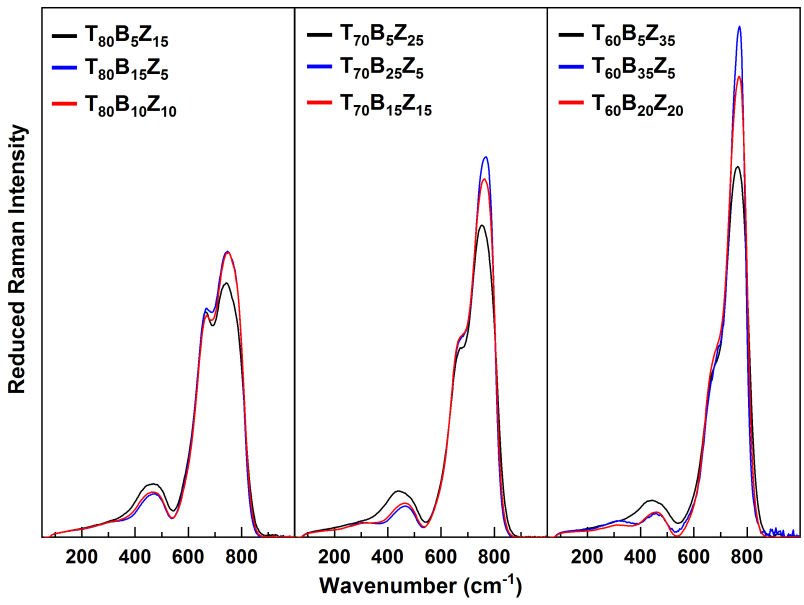

Fig. 15 Normalized Raman spectra of TeO_2-BaO-ZnO glasses at three constant TeO_2 concentrations 80%, 70% and 60%.

The Raman spectra were decomposed with eight Voigt functions centred approximately at wavenumbers of ≈220 cm^{-1}, ≈330 cm^{-1}, ≈430 cm^{-1}, ≈470 cm^{-1}, ≈590 cm^{-1}, ≈660 cm^{-1}, ≈750 cm^{-1} and ≈790 cm^{-1} which were assigned to individual vibrational modes according to the work [4,25,29]. The assignment of vibrational modes to individual structural units in TBZ glasses is represented in Tab. 3. The representative decomposed reduced Raman spectrum for the $T_{60}B_{20}Z_{20}$ glass is shown in Fig. 16. The vibrational modes at ≈220 cm^{-1} and ≈330 cm^{-1} (bands A) are assigned to the collective vibrational modes of the glass structure. The bands at ≈430 cm^{-1} (band B) and ≈470 cm^{-1} (band C) are assigned to the symmetric bending and stretching vibrational modes of the Te-O-Te linkages in corner-sharing TeO_4, TeO_{3+1} and TeO_3 polyhedra [23]. The presence of TeO_4 units is represented by the bands at ≈590 cm^{-1} (band D), which correspond to the respective anti-symmetric stretching modes of a continuous network of TeO_4 units. The band at ≈660 cm^{-1} (band E) represents the antisymetric vibrations of Te_{eq}-O-$_{ax}$Te units composed of two non-equivalent Te-O bonds [29]. The band at ≈750 cm^{-1} (band F) corresponds to the vibrational stretching modes of TeO_{3+1} and TeO_3 units and the band at ≈790 cm^{-1} (band G) to vibrational modes of non-bridging oxygens (NBO). Non-bridging oxygens are bonded as Te=O or Te–O^- as is illustrated in Fig.2. According to the literature [29], the NBO atoms in TeO_{3+1} and TeO_3 units weakly interact with other surrounding atoms which may lead to a weakening of the bond between NBO and central Te atoms. This interaction may cause a shift of the appropriate Raman modes towards lower wavenumbers.

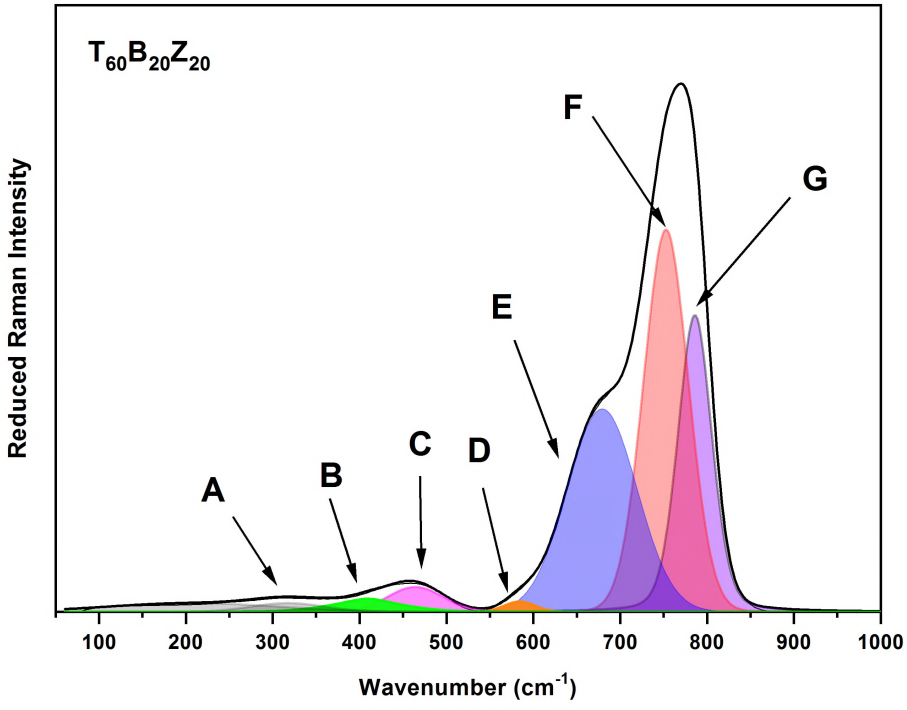

Fig. 16 Decomposed Raman spectrum of $T_{60}B_{20}Z_{20}$ glass with denotation of vibrational bands according to Tab.3.

Tab. 3 Result of deconvolution and assignments of peaks in TBZ glasses

Raman shift (cm^{-1})	Structure unit	Assignments
A (≈220cm^{-1},≈330cm^{-1})		Collective vibration of local structure
B (≈430 cm^{-1})	BO-related units in Te-O-Te	Network connectivity via corner sharing
C (≈470 cm^{-1})		TeO_4, TeO_{3+1} and TeO_3 polyhedra
D (≈590 cm^{-1})	BO-related units	continuous TeO_4 network
E (≈660 cm^{-1})	Te_{eq}-O-$_{ax}$Te bonds	TeO_4 concentration
F (≈750cm^{-1})	TeO_3 and TeO_{3+1} units	TeO_{3+1}, TeO_3 concentration
G (≈790 cm^{-1})	Non-bridging oxygen TeO^-	NBO^- content

The ratio of the vibrational bands (E+F+G)/(B+C+D) from Tab. 3 corresponds to the ratio of bridging oxygen to nonbridgin oxygen content in studied TBZ glasses. This ratio is plotted as function of BaO and ZnO concentration in TBZ glasses in Fig. 17. The addition of BaO and ZnO increases the concentration ratio of NBO/BO units in TBZ glasses, especially in those containing a low content of TeO_2.

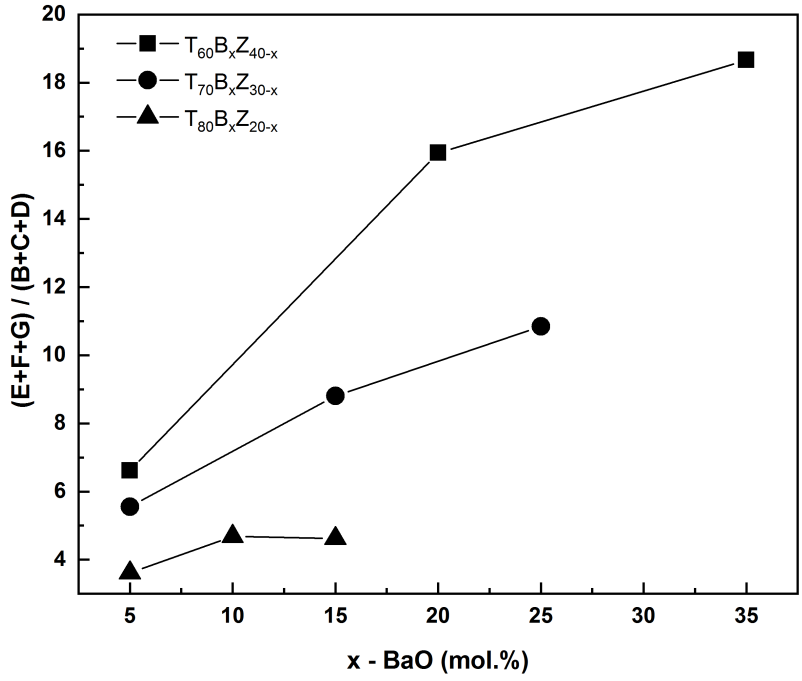

Fig. 17 Dependence of (E+F+G) to (B+C+D) Raman bands ratio to used modifier concentration

4.1.3 Thermal characteristics (DSC, DTA)

One of the most important parameters for glass characterization, especially for materials used for optical fibres, is their thermal behaviour, which is represented by the temperature of glass transition T_g and temperature of crystallization T_x. The glass transition temperature was investigated using both differential scanning calorimetry (DSC) and differential thermal analysis (DTA) methods. Obtained results were in good agreement within the instrument error of ±3 °C.

For ternary TBZ system, it was observed that the temperature of glass transition increases with the increasing BaO content and decreasing concentration of TeO_2 (Fig.18). The lowest T_g have been found for $T_{90}B_5Z_5$ and $T_{80}B_5Z_{15}$ glasses as T_g = 319 °C. Contrary to previous results, the highest T_g corresponds to composition $T_{50}B_{25}Z_{25}$ (T_g = 369 °C). It was found that the substitution of ZnO by BaO leads to increasing of T_g. Moreover, the T_g in $T_{90-x}B_{x/2}Z_{x/2}$ (x = 0, 10, 20, 30 mol.%) is changed approximately by ≈10 °C per 10 mol.% of TeO_2.

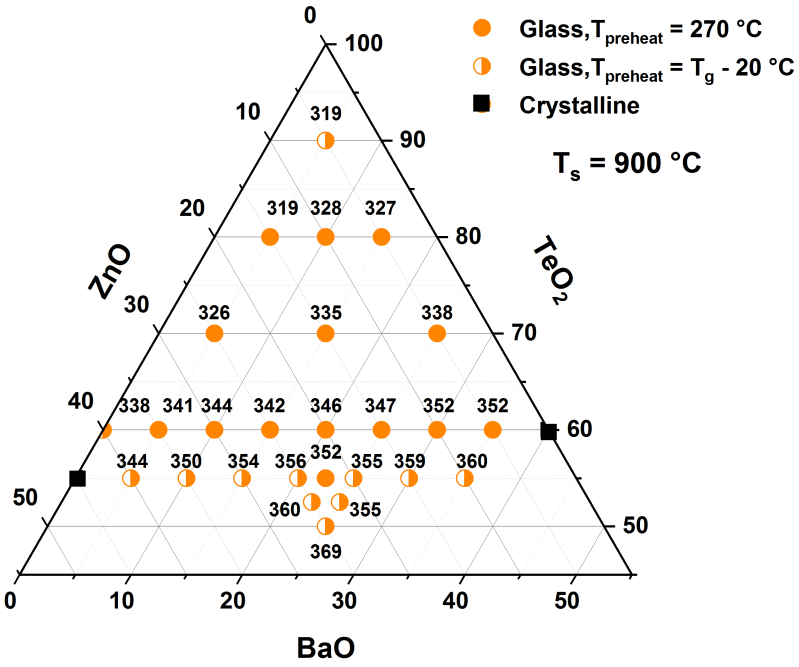

Fig. 18 Ternary diagram of TeO_2-BaO-ZnO (TBZ) glasses with corresponding glass transition temperatures Tg

According to literature, T_g of oxide glasses increases with the increasing bond strength, cross-link density and closeness of packing of the glass structure (decrease of free volume of the glass) [1,11,79]. The Te-O bonding energy (E_{Te-O} = 376.1 ± 20.9 kJ.mol^{-1} [80]) is significantly lower than the energy of Ba-O bonds (E_{Ba-O} = 561.9 ± 13.4 kJ.mol^{-1} [80]), but higher than energy of the O-Zn bond (E_{Zn-O} = 159 ± 4 kJ.mol^{-1} [81]). In Fig.18 is observed that T_g increases with the higher concentration of BaO and lower TeO_2 content which may be explained on the

basis of bond energies. However, in the case of substitution TeO_2 by ZnO T_g increases as well, which cannot be explained on the basis of the bond energy theory since $E_{Zn\text{-}O} < E_{Te\text{-}O}$. Such behaviour may be attributed to a decrease of molar volume of glass by addition of small Zn^{2+} cations into TBZ (see Fig. 22).

Investigation of thermal patterns (Fig.19) showed strong crystallization peak for high concentrations of TeO_2 of about 90% and 80%. This detected crystallization almost disappeared for lower concentrations under the increasing concentration of modifiers. Cleary assignable crystallization peak for composition with a lower concentration of TeO_2 was observed only for compositions with a higher concentration of ZnO than BaO. In relation to previous results, thermal stability seems to be suitable for all measured samples with clearly assignable crystallization temperature T_x (Tab.4.).

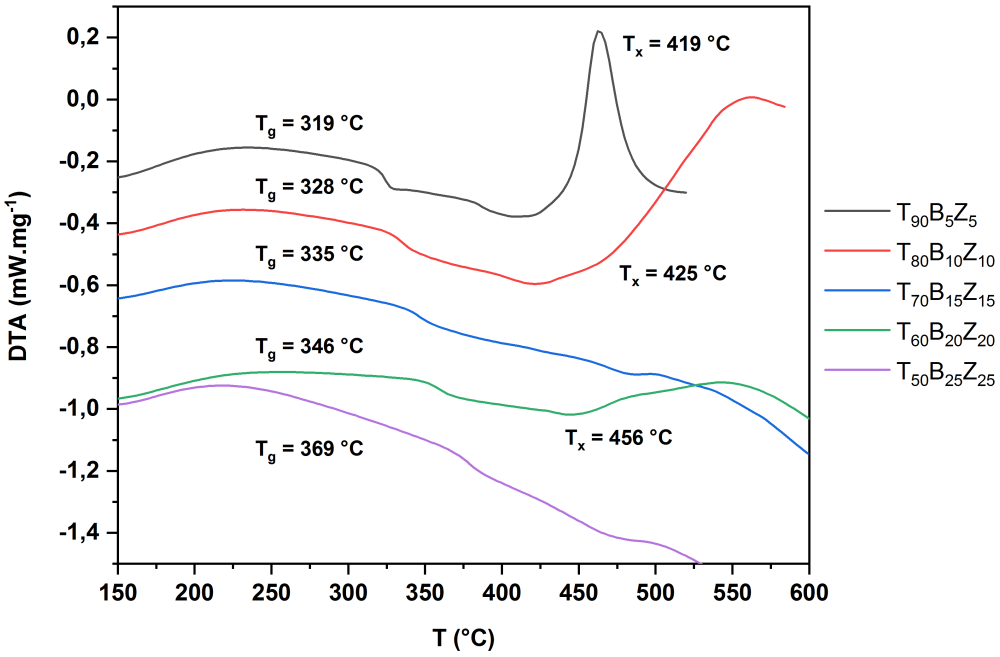

Fig. 19 TGA traces of TeO_2-BaO-ZnO (TBZ) glasses for central vertical line compositions with a similar concentration of modifiers and various concentrations of TeO_2

Some of the prepared samples were investigated in bulk and powder form to better understand their thermal properties and the behaviour of crystallization processes. In the thermal diagram for sample $T_{60}B_{20}Z_{20}$ (Fig.20), the crystallization peak is shifted towards lower temperatures when the powdered sample is used instead of bulk glass. However, the glass transition temperature was practically constant. The rapid crystallization of the powdered sample may be explained by the presence of surface crystallization [82]. Suppression of internal crystallization also improves the ability of glass to resist micro crystalization inside the fibres during cyclic heating procedures.

Tab. 4 Transition and crystallization temperatures of TeO_2-BaO-ZnO (TBZ) glasses with calculated stability coefficient (ΔT) and melting temperature (T_m) estimated from Turnbull "2/3 rule"

Notation	T_g (°C)	T_x (°C)	$\Delta T = T_x - T_g$ (°C)	T_m (°C)
$T_{90}B_5Z_5$	319	419	100	624
$T_{80}B_5Z_{15}$	319	416	97	624
$T_{80}B_{10}Z_{10}$	328	425	97	638
$T_{80}B_{15}Z_5$	327	-	-	636
$T_{70}B_5Z_{25}$	326	450	124	635
$T_{70}B_{15}Z_{15}$	335	-	-	648
$T_{70}B_{25}Z_5$	338	-	-	653
$T_{60}B_5Z_{35}$	341	494	153	657
$T_{60}B_{20}Z_{20}$	346	456	110	665
$T_{60}B_{35}Z_5$	352	-	-	674
$T_{50}B_{25}Z_{25}$	369	-	-	700

Finally, the effect of used Pt or Al_2O_3 crucible for the synthesis of TBZ glasses was investigated as well. EDX spectroscopy of the Er-doped $T_{60}B_{20}Z_{20}$ glasses prepared from alumina crucible explored the presence of Al (ca 1.5 at.%) in the synthesized glass. Moreover, it is very well known that TeO_2-based glasses synthesized from platinum crucible contain Pt [1,47,48]. The difference of T_g value between TBZ synthesized in Pt or Al_2O_3 crucible is ≈10 °C, but practically no change in crystallization temperature was observed. The difference in T_g may be explained on the basis of lower molar volume of Al-doped TBZ and higher molar volume of Pt-doped TBZ glasses as was discussed above.

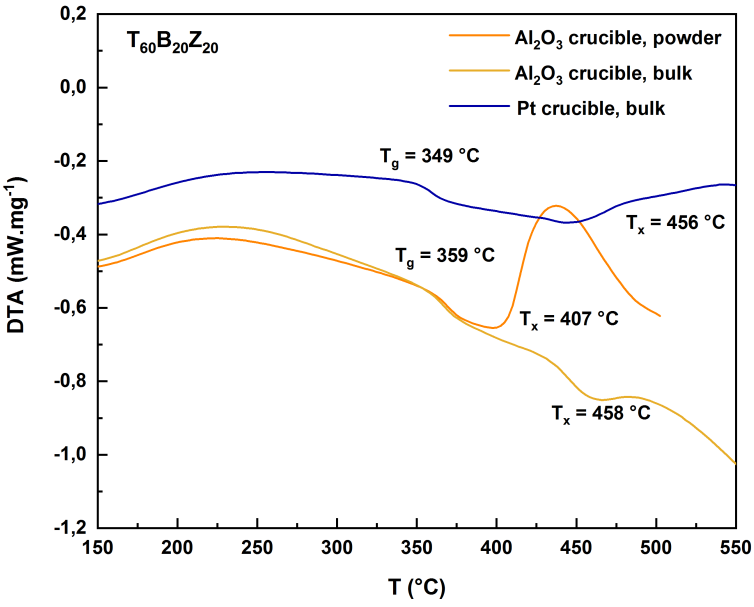

Fig. 20 TGA traces of glass sample $T_{60}B_{20}Z_{20}$ as a) powder - alumina crucible b) bulk – alumina crucible and c) bulk – platinum crucible.

4.1.4 Density measurement

The density of all prepared glass samples was measured using a standard Archimedes method with distilled water as a reference liquid. The molar volume has been calculated using the Eq. (28):

$$V_{mol} = {}^{M_{tot}}/_{\rho}, \tag{28}$$

, where M_{tot} is the average molar weight of TBZ glass (g mol^{-1}), ρ is glass density (g cm^{-3}).

For ternary TBZ system, it was observed that the density decreases with the substitution of ZnO by BaO and with increasing BaO content and decreasing concentration of TeO_2 (Fig.21). On the other hand, the molar volume increases in the opposite manner with a higher concentration of BaO. Such behaviour may be attributed to decrease of molar volume of glass by addition of small Zn^{2+} cations into TBZ (Fig.22) [79,83]. Observed trends corresponding with the behaviour in the binary glasses [84].

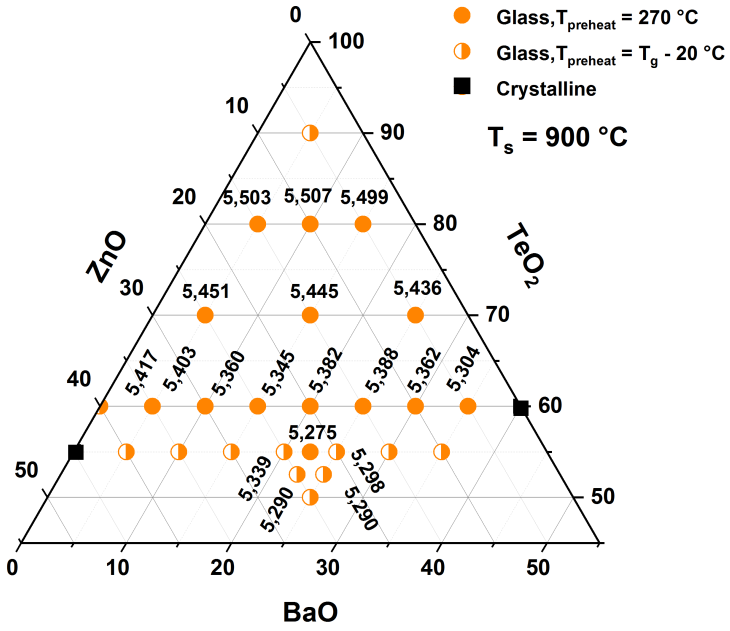

Fig. 21 Density evolution across the TeO_2-BaO-ZnO (ZBZ) glass ternary concentration diagram

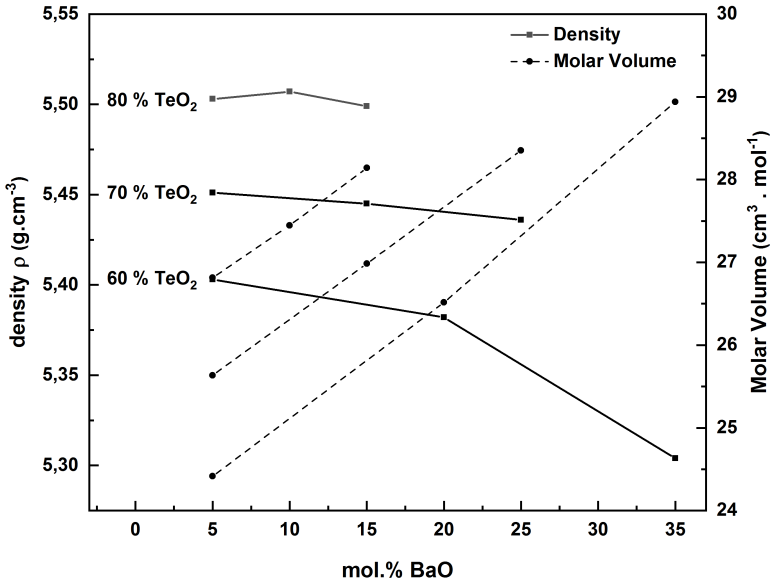

Fig. 22 Density and molar volumes as a function of BaO concentration in TeO_2-BaO-ZnO glasses

4.1.5 Refractive index (PCR, VASE)

Refractive index of the prepared TBZ samples was measured on polished blocks of a thickness of about 4 mm by a prism-coupling method at the three different wavelengths of 632, 1064 and 1550 nm and by a variable angle spectroscopic ellipsometry (VASE).

Precise determination of the spectral dependence of refractive index is one of the most critical information for successful application of photonic materials. Composition dependence of refractive index at 632 nm measured by prism coupled refractometry (PCR) is shown in the ternary diagram in Fig.23. The values of the refractive indices change from 2.1 to 1.90. Higher ZnO and TeO_2 contents are connected with higher values of refractive indices.

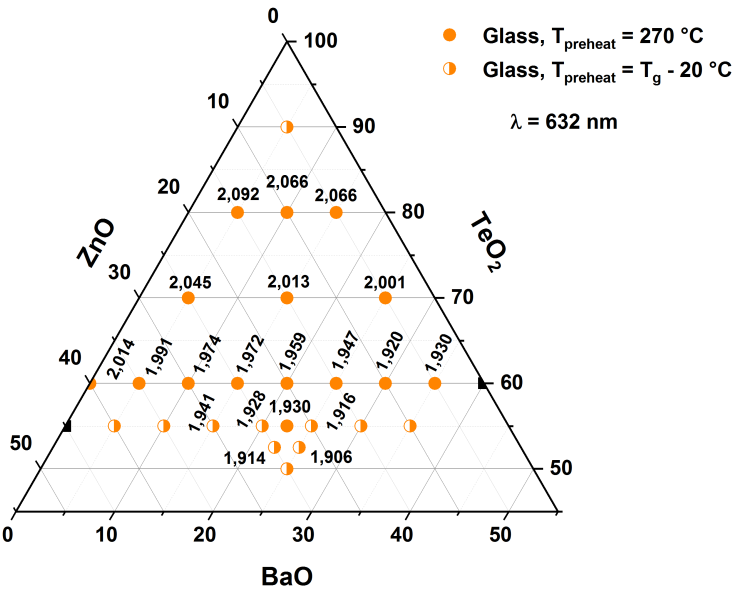

Fig. 23 Ternary diagram of TeO_2-BaO-ZnO (ZBZ) glasses with respect to their compositional dependency of refractive index using Prism Coupled Refractometry for at λ = 632 nm.

Data measured via PCR at 632 nm were plotted in Fig.24 as the function of modifier concentration. Compositional dependence of refractive index seems to be linear, which probably allows to synthesize the TBZ glasses with desired refractive index.

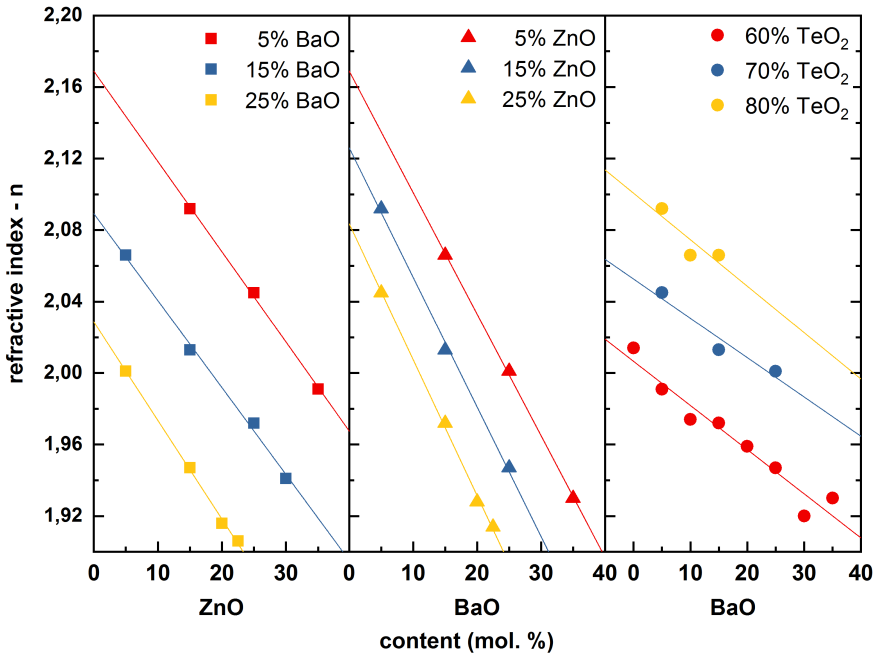

Fig. 24 Dependence of the refractive index as a function of modifier concentration measured via Prism Coupled Refractometry at $\lambda = 632$ nm

Observed refractive index changes corresponded with works on binary TeO_2-ZnO and TeO_2-BaO glasses [84]. The change of dielectric constant or refractive index may be described on the basis of Claussius-Mossotti (C.-M.) equation [85,86] or Lorentz–Lorentz (L.-L.) equation [87] with respect to polarizability and density. Polarizability roughly depends on the atomic number and it may be estimated that increases in the following series Zn < Te < Ba [84,88], which should lead to increase of refractive index with increasing concentration of BaO and decreasing concentration of ZnO in TBZ glasses. However, this is in contradiction with obtained results presented in Fig. 24, where the refractive index increases with decreasing concentration of BaO. Thus, the refractive index dependency is not related only to polarizability but to density (or molar volume) of studied glasses. With increasing content of TeO_2 and decreasing content of ZnO or BaO, the refractive index in Fig. 24 increases due to increasing density of glasses. Similarly, the substitution of BaO by ZnO leads to increase in refractive index due to increasing density of TBZ glass.

Tab. 5 Experimentally determine refractive indices via PCR and VASE at 632, 1064 and 1550 nm

	Prism method (PCR)			VASE method			
λ	632 nm	1064 nm	1550 nm	632 nm	1064 nm	1550 nm	Eg (eV)
$T_{60}B_5Z_{35}$	1.99	1.96	1.95	1.99	1.96	1.95	4.00
$T_{60}B_{20}Z_{20}$	1.96	1.93	1.92	1.96	1.93	1.91	3.99
$T_{60}B_{35}Z_5$	1.93	1.90	1.90	1.90	1.88	1.88	4.15
$T_{70}B_5Z_{25}$	2.05	2.00	2.00	2.05	2.01	2.00	3.79
$T_{70}B_{15}Z_{15}$	2.01	1.98	1.97	2.02	1.98	1.98	3.84
$T_{70}B_{25}Z_5$	2.00	1.97	1.96	1.99	1.95	1.94	3.95
$T_{80}B_5Z_{15}$	2.09	2.05	2.04	2.09	2.05	2.04	3.73
$T_{80}B_{10}Z_{10}$	2.07	2.02	2.02	2.06	2.02	2.01	3.85
$T_{80}B_{15}Z_5$	2.07	2.02	2.02	2.06	2.02	2.01	3.98

One of the disadvantages of PCR measurement is its limited number of used light sources. In telecommunication technologies is critical to know the dispersion of refractive index. Therefore, the variable angle spectroscopic ellipsometry has been used to determine the dispersion of refractive index using the Tauc-Lorentz parameterization of ellipsometric data [73–75]. Since ellipsometric measurements have high demands on surface treatment, obtained results were compared with PCR measurement and with previous work of *Manikandan, et al*. [4] for sample $T_{60}B_{20}Z_{20}$ as can be seen in Fig.25. Experimentally obtained values via VASE method and PCR method for three specific wavelengths are listed in Tab.5. From this comparison, it can be concluded that the results obtained via PCR and VASE are in good agreement. The optical band gap energy (E_g) of prepared samples is presented in Tab.5.

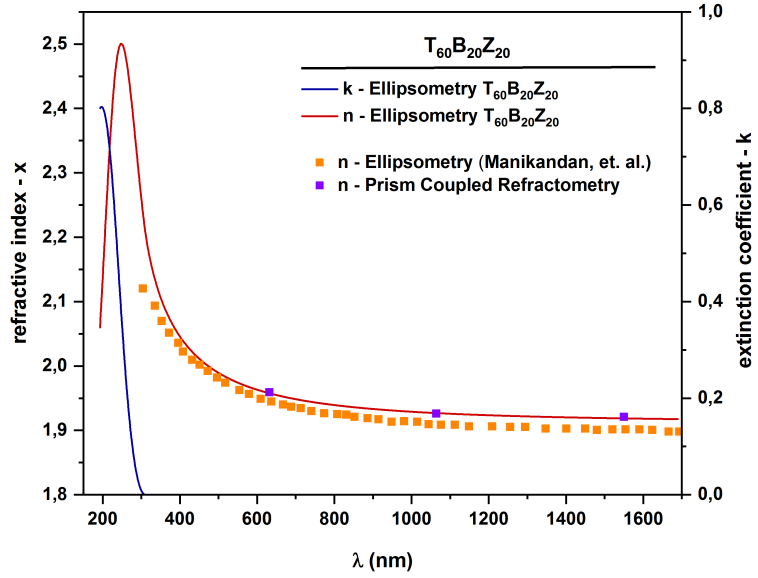

Fig. 25 Measured refractive indices for selected $T_{60}B_{20}Z_{20}$ sample using PCR (632, 1064 and 1550 nm) and VASE methods.

4.1.6 UV-Vis-NIR spectroscopy, FTIR spectroscopy

Transmission spectra of nine selected samples were recorded with JASCO and Shimadzu spectrophotometer for UV-Vis-NIR (250-2500 nm) and with BRUKER for NIR and MIR spectral range (2300-7000 nm). As is seen in Fig.26 is apparent that the TBZ glasses are transparent in a wide range of wavelengths from visible (≈350 nm) to mid-infrared (6 μm) part of the spectrum.

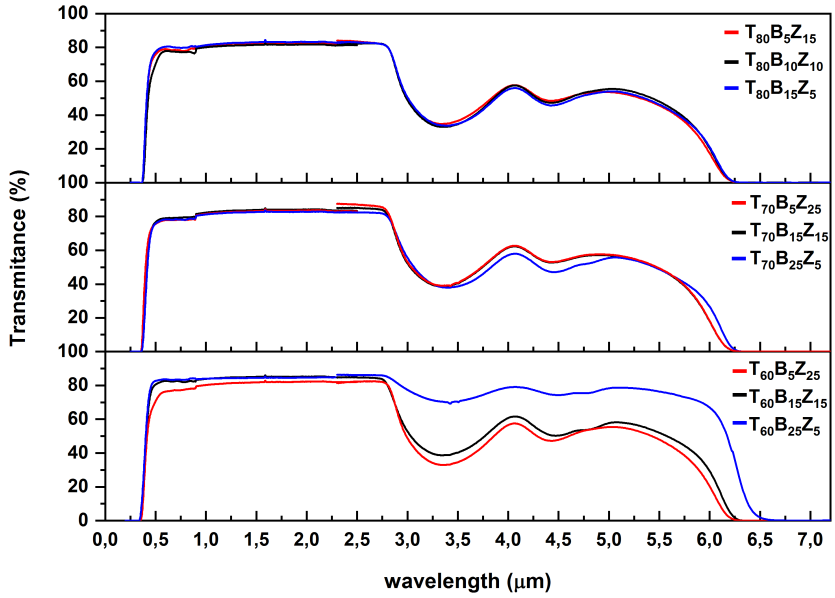

Fig. 26 Transmission spectra of TeO_2-BaO-ZnO glasses

Transmission losses in the MIR region were assigned to the fundamental stretching vibrations of free –OH groups between 2500-3000 cm^{-1} (Fig.26). Absorption of OH units can be interpreted as absorption on stretching vibrations of free OH^- groups or correspond to the presence of hydrogen bonds (H–O ···· O), which formation in TBZ glasses has been proposed [89–91].

Transmission spectra for central composition line in ternary diagram including samples $T_{60}B_{20}Z_{20}$, $T_{70}B_{15}Z_{15}$ and $T_{80}B_{10}Z_{10}$ were plotted in Fig. 27. As is visible from this plot, the increasing concentration of TeO_2 leads to slow narrowing of the optical window and exhibit lower transmission. This observed transmission decrease was connected with the increasing value of the refractive index for glasses with higher TeO_2 content. The refractive index is followed by increasing of reflectivity and thus corresponding decrease of transmittance [9,55].

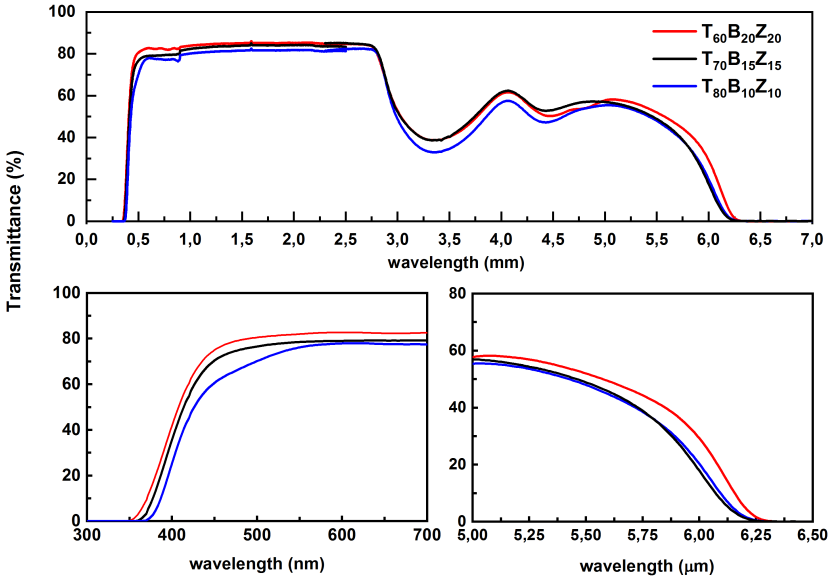

Fig. 27 Transmission spectra of TeO_2-BaO-ZnO glasses for 80,70 and 60% concentration of TeO_2

4.2 General study of doped TeO_2-BaO-ZnO:Er^{3+} (TBZ:Er) glasses

4.2.1 X-ray diffraction (XRD) analysis

The amorphous state of prepared TeO_2-BaO-ZnO:Er glasses was investigated via XRD analysis for all nine samples. The analysis shows no discrete sharp diffraction peaks, but only characteristic halo pattern representing the amorphous nature of prepared samples [76]. Only the $T_{80}B_5Z_{15}$:$Er_{0.2}$ and $T_{60}B_5Z_{35}$:$Er_{0.2}$ samples were partially crystalline and contained the respective orthorhombic α-TeO_2 (space group P212121) and monoclinic Zn_3TeO_6 (space group C2/c) crystalline phases (see Fig. 28) [77]. Growth of α-TeO_2 microcrystals was also observed in binary 80TeO_2-20ZnO glasses [92].

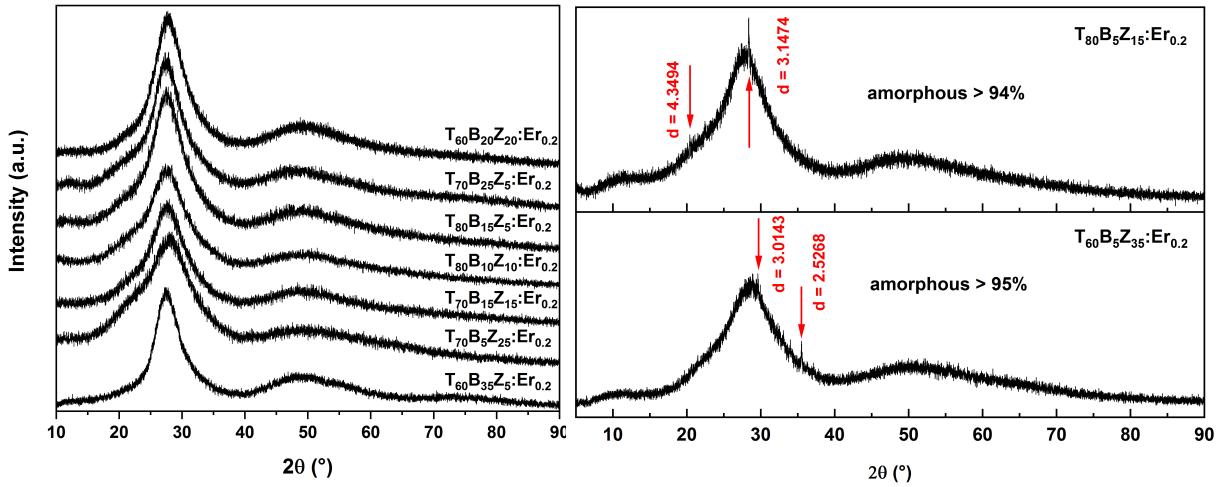

Fig. 28 The XRD patterns of (left) ternary TeO2-BaO-ZnO glasses doped with 0.2 % Er^{3+} with observed typical halo patern and (right) $T_{80}B_5Z_{15}$:$Er_{0.2}$ and $T_{60}B_5Z_{35}$:$Er_{0.2}$ with crystallization peaks assigned to Zn_3TeO_6 and α-TeO_2 structural units.

4.2.2 Energy dispersive X-ray analysis (EDX)

Real compositions of prepared samples were investigated via EDX microanalysis. It has to be mentioned, that small amount of Al (< 2 at. %) was identified in all samples, where the concentration of Al increases with increasing TeO_2 content. Comparison of the theoretical and the experimental chemical composition of prepared glasses is listed in Tab.6. The instrumental error of EDX analysis (interference effect) did not allow to measure the precise content of Te and O. For this reason, the Ba/Zn ratio was established as the qualitative index of the real glass composition. From the obtained results in Tab. 6 is obvious, that compositions of prepared samples agree with the theoretical prediction.

Tab. 6 Theoretical and experimental compositions of prepared samples of TBZ glasses

TBZ		Te	Ba	Zn	O	Er	Ba/Zn
$T_{80}B_{10}Z_{10}:Er_{0.2}$	**theor.**	28.43	3.55	3.55	64.26	0.20	1.00
	exp.	28.40	4.83	4.10	62.41	0.26	1.32 ± 0.57
$T_{80}B_5Z_{15}:Er_{0.2}$	**theor.**	28.43	1.78	5.33	64.26	0.20	0.33
	exp.	29.49	2.10	6.34	61.88	0.19	0.37 ± 0.22
$T_{80}B_{15}Z_5:Er_{0.2}$	**theor.**	28.43	5.33	1.78	64.26	0.20	2.99
	exp.	28.19	5.38	3.09	63.13	0.21	2.06 ± 0.99
$T_{70}B_{15}Z_{15}:Er_{0.2}$	**theor.**	25.80	5.53	5.53	62.95	0.20	1.00
	exp.	26.11	5.87	6.36	61.46	0.20	0.97 ± 0.31
$T_{70}B_5Z_{25}:Er_{0.2}$	**theor.**	25.80	1.84	9.21	62.95	0.20	0.20
	exp.	25.78	2.64	9.92	61.44	0.21	0.28 ± 0.13
$T_{70}B_{25}Z_5:Er_{0.2}$	**theor.**	25.80	9.21	1.84	62.95	0.20	5.00
	exp.	26.49	10.33	2.18	60.79	0.22	6.11 ± 3.49
$T_{60}B_{20}Z_{20}:Er_{0.2}$	**theor.**	22.96	7.65	7.65	61.53	0.20	1.00
	exp.	23.04	7.99	8.84	59.87	0.24	0.93 ± 0.22
$T_{60}B_5Z_{35}:Er_{0.2}$	**theor.**	22.96	1.91	13.40	61.53	0.20	0.14
	exp.	23.22	2.54	14.38	59.63	0.23	0.18 ± 0.08
$T_{60}B_{35}Z_5:Er_{0.2}$	**theor.**	22.96	13.39	1.91	61.53	0.20	7.00
	exp.	22.64	12.99	2.31	61.85	0.21	7.15 ± 3.53

4.2.3 Thermal properties

Doped TBZ:Er samples were investigated using STA 449 F5 (Netzsch) operating in the heat flux DTA mode in temperature range 25-650 °C in order to determine their thermal properties represented by the temperature of glass transition (T_g) and crystallization (T_x).

For ternary TBZ:$Er_{0.2}$ glass system was observed that the temperature of glass transition increases with the increasing BaO content and decreasing concentration of TeO_2 (Tab.7). Similar dependences were observed for undoped glasses. In comparison to undoped TBZ samples, the glass transition temperature in TBZ:Er glasses is increased by 11 up to 21 °C. According to literature, T_g of oxide glasses increases with the increasing bond strength, cross-link density and closeness of packing of the glass structure (decrease of the free volume of the glass) [1,11,79]. Analysis of the chemical composition was made using EDX spectroscopy, which explored the presence of Al (ca 1.5 at.%) in the synthesized glass prepared from alumina crucible. Increases of glass transition temperature may then attributed to decrease of molar

volume by addition of small Zn^{2+} and also Al^{3+} cations into TBZ glass as a consequence of synthesis in the alumina crucible. Similar observation was made for undoped samples, where the difference of T_g value between TBZ synthesized in Pt or Al_2O_3 crucible was observed and discussed (see section 4.1.3). Investigation of thermal patterns (Fig.29) exhibit clear crystallization peak for samples with lower ZnO content. The thermal stability seems to be suitable for glasses with TeO_2 content lower than 80 % (Tab.7) .

Tab. 7 Transition and crystallization temperatures of TeO_2-BaO-ZnO:Er (TBZ:Er) glasses with calculated stability coefficient and melting temperature using „2/3“ Turnbull rule [11].

Sample	T_g (°C)	T_x (°C)	$\Delta T = T_x - T_g$ (°C)	T_m (°C)
$T_{80}B_{15}Z_5:Er_{0.2}$	343	435	92	660
$T_{70}B_{25}Z_5:Er_{0.2}$	359	480	121	685
$T_{60}B_{35}Z_5:Er_{0.2}$	363	481	118	691
$T_{60}B_{20}Z_{20}:Er_{0.2}$	359	458	99	685

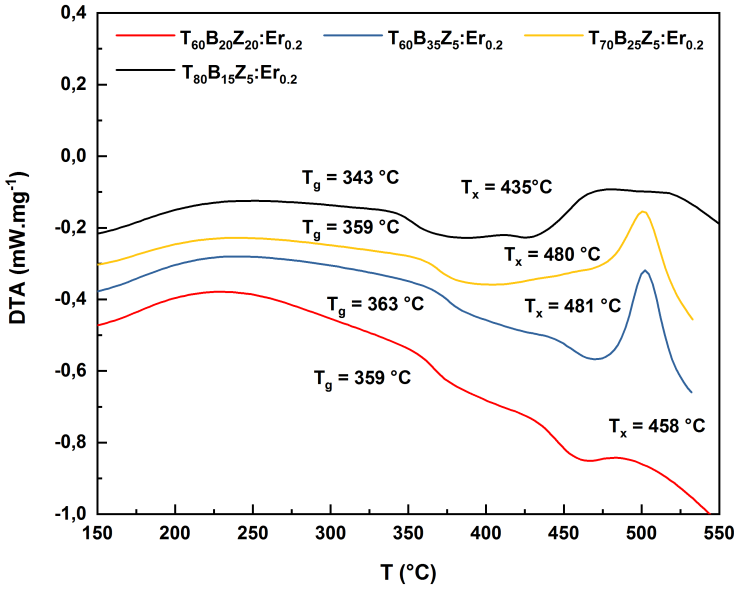

Fig. 29 Measured DTA patterns for homogenous TBZ:Er samples

4.2.4 Density measurement

The densities for all prepared glass samples were measured by standard Archimedes method with used distilled water as a reference liquid. Measurements were made simultaneously for doped and pure TBZ reference glasses.

For doped ternary TBZ system was observed, that the density decreases with the substitution of ZnO by BaO and with increasing BaO content and decreasing concentration of TeO_2 (Tab.8). Such behaviour may be attributed to decrease of molar volume of glass by addition of small

Zn^{2+} cations into TBZ (Fig.22) [79,83] as was in the same manner observed and discussed for the undoped glasses in 4.1.4.

Tab. 8 Densities and molar volumes of selected doped TeO_2-BaO-ZnO glasses

TeO_2-BaO-ZnO	ρ_{doped} (g.cm^{-3})	V_M (cm^3.mol^{-1})
$T_{80}B_{15}Z_5$	5.502	28.24
$T_{70}B_{25}Z_5$	5.416	28.57
$T_{60}B_{35}Z_5$	5.335	28.88
$T_{60}B_{20}Z_{20}$	5.360	26.74

4.2.5 Refractive index measurement

The optical refractive index of the prepared TBZ:Er samples were carried out on polished blocks of thickness of about 2 mm by Variable angle spectroscopic ellipsometry (VASE) with focusation probes. Obtained data were evaluated using Tauc-Lorentz model [73,74] with included roughness [75] in spectral range 200-1800 nm to obtain optical dependence of the refractive index as well as the value of energy gap (E_g) of prepared samples (see Tab.9).

Observed refractive index changes corresponded with work on undopeds samples. With increasing content of TeO_2 and decreasing content of ZnO or BaO, the refractive index in Fig. 30 increases due to increasing density of glasses. Similarly, the substitution of BaO by ZnO leads to increase in refractive index due to increasing density of TBZ glass.

Tab. 9.Measured refractive indices of doped TBZ glasses using Variable Angle Spectroscopic Ellipsometry with included roughness.

λ	632 nm	1064 nm	1550 nm	E_g (eV)
$T_{60}B_{20}Z_{20}$	1.95	1.92	1.91	3.89
$T_{60}B_{35}Z_5$	1.87	1.85	1.84	3.96
$T_{70}B_{25}Z_5$	1.96	1.93	1.92	3.92
$T_{80}B_{15}Z_5$	2.02	1.99	1.98	3.95

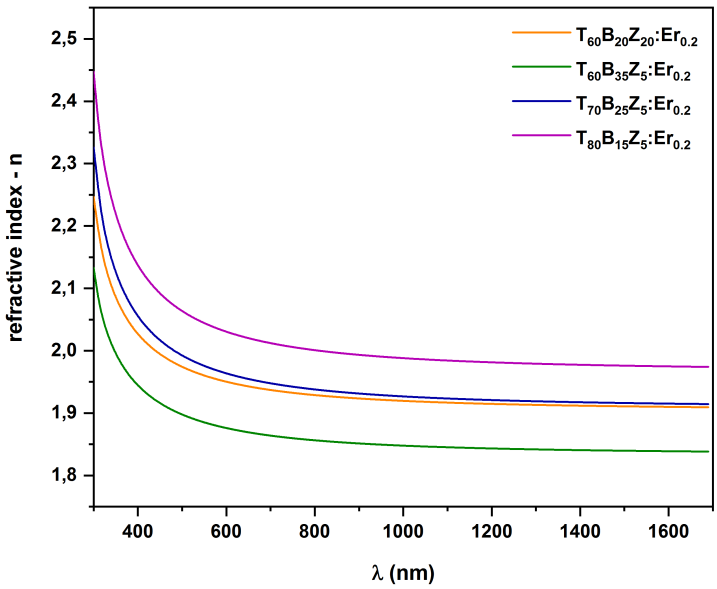

Fig. 30 Plotted refractive indices of prepared doped TeO_2-BaO-ZnO glasses obtained via Variable Angle Spectroscopic Ellipsometry (VASE).

4.2.6 UV-Vis-NIR spectroscopy, FTIR spectroscopy

For each homogenous sample was measured spectral dependence of optical absorption with JASCO and Shimadzu spectrophotometer in UV-Vis-NIR (250–2500 nm) and with BRUKER Vertex in NIR and MIR spectral range (2300–7000 nm).

Studied samples $T_{80}B_{15}Z_5$:$Er_{0.2}$, $T_{70}B_{25}Z_5$:$Er_{0.2}$, $T_{60}B_{20}Z_{20}$:$Er_{0.2}$ and $T_{60}B_{35}Z_5$:$Er_{0.2}$ exhibit multiple absorption bands in a whole spectral range. Similar transmission losses in the MIR region as in the case of undoped samples were observed and assigned to the fundamental stretching vibrations of free -OH groups between 2500-3000 cm^{-1} [90-91]. Several studies also mentioned the relation between the concentration of –OH groups and and non-radiative recombination processes via multiphonon relaxation which quench the Er^{3+}:$^4I_{13/2} \rightarrow {}^4I_{15/2}$ photoluminescence emission [93,94]

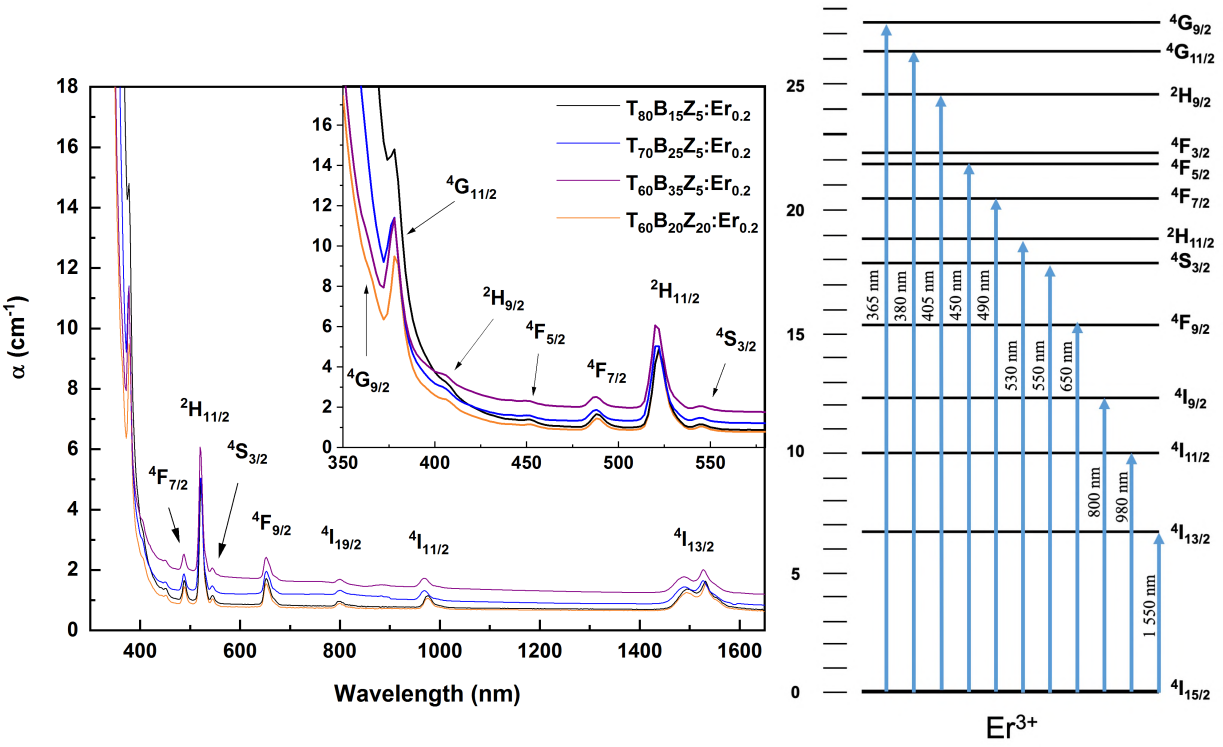

Fig. 31 Spectral evolution of absorption coefficient (α) of 0.2% Er^{3+} doped glasses $T_{80}B_{15}Z_5$, $T_{70}B_{25}Z_5$, $T_{60}B_{35}Z_5$ and $T_{60}B_{20}Z_{20}$ with shown assigned 4f→4f* electronic transitions of Er^{3+} ions. Signal deflection around ≈900 nm is caused by the instrumental error.

UV-Vis-NIR absorption spectra presented in Fig. 31 composes of Er^{3+} absorption bands due to intra-4*f* electronic transitions. Ten common Er^{3+} ground state absorption bands for all studied glasses were identified using [95,96] as follows: $^4I_{15/2}\rightarrow{}^4I_{13/2}$ (≈1.53 μm), $^4I_{15/2}\rightarrow{}^4I_{11/2}$ (≈976 nm), $^4I_{15/2}\rightarrow{}^4I_{9/2}$ (≈802 nm), $^4I_{15/2}\rightarrow{}^4F_{9/2}$ (≈652 nm), $^4I_{15/2}\rightarrow{}^4S_{3/2}$ (≈546 nm), $^4I_{15/2}\rightarrow{}^2H_{11/2}$ (≈522 nm), $^4I_{15/2}\rightarrow{}^4F_{7/2}$ (≈489 nm), $^4I_{15/2}\rightarrow{}^4F_{5/2}$ (≈450 nm), $^4I_{15/2}\rightarrow{}^2H_{9/2}$ (≈406 nm) and $^4I_{15/2}\rightarrow{}^4G_{11/2}$ (≈378 nm). Observed Er^{3+} ground state absorption transitions are illustrated in energy diagram in Fig.31. The absorption edge of TBZ:Er glasses in Fig. 31 is red shifted with increasing content of TeO_2 which may be explained by increasing density of TBZ glasses.

The absorption cross section of the prepared samples was calculated from the experimentally obtained absorption coefficient in UV-ViS-NIR region of the electromagnetic spectrum (Fig.32 and Fig.33). No significant trends in absorption cross section spectra of prepared samples with a similar concentration of Er^{3+} ions were found. Observed Er^{3+} absorptions bands below ≈480 nm were influenced by glassy host absorption.

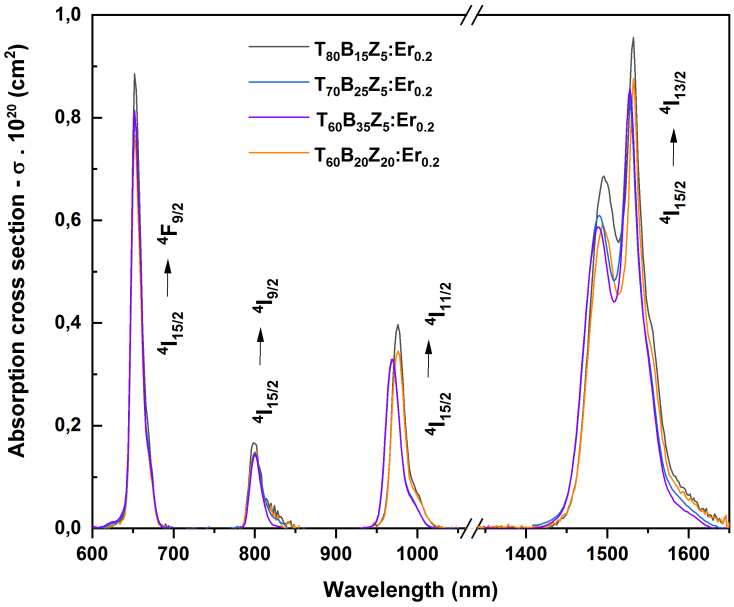

Fig. 32 Spectral evolution of absorption cross section (σ) of 0.2% Er^{3+} doped glasses $T_{80}B_{15}Z_5$, $T_{70}B_{25}Z_5$, $T_{60}B_{35}Z_5$ and $T_{60}B_{20}Z_{20}$ in wavelength range between 600-1650 nm with shown corresponding 4f→4f* electronic transitions of Er^{3+} ions. Signal deflection around ~900 nm is caused by instrumental error

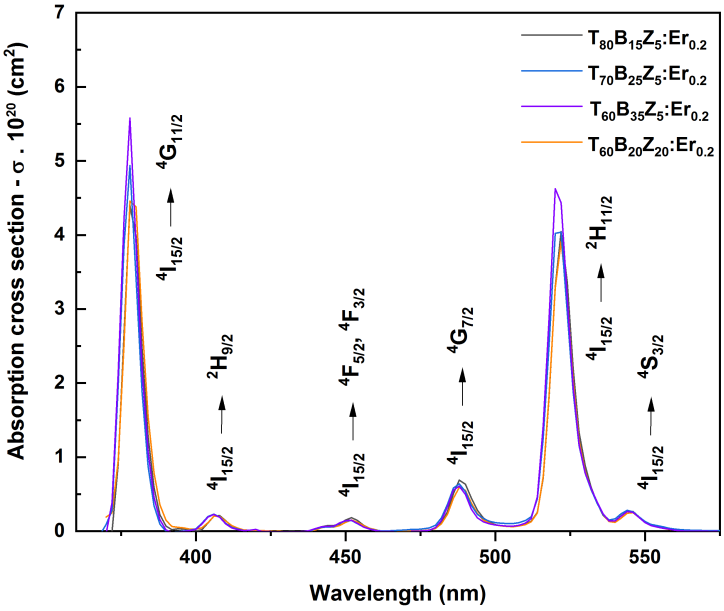

Fig. 33 Spectral dependence of absorption cross section (σ) of 0.2% Er^{3+} doped glasses $T_{80}B_{15}Z_5$, $T_{70}B_{25}Z_5$, $T_{60}B_{35}Z_5$ and $T_{60}B_{20}Z_{20}$ in wavelength range between 350-600 nm with shown corresponding 4f→4f* electronic transitions of Er^{3+} ions.

4.2.7 Photoluminescence spectroscopy

Photoluminescent spectra of Er^{3+}-doped TBZ glasses were obtained using Ti:Saphire laser (980 nm, 802 nm) and fibre laser (975 nm) as the excitation sources. Fibre laser was used for recording of upconversion emission spectra. Studied samples $T_{80}B_{15}Z_5$:$Er_{0.2}$, $T_{70}B_{25}Z_5$:$Er_{0.2}$, $T_{60}B_{20}Z_{20}$:$Er_{0.2}$ and $T_{60}B_{35}Z_5$:$Er_{0.2}$ were placed perpendicularly to the detector and the excitation

laser beam was focused to the surface under the angle of about ≈45 °. Experimentally observed Er^{3+} emission transitions are illustrated in Fig. 34 [96].

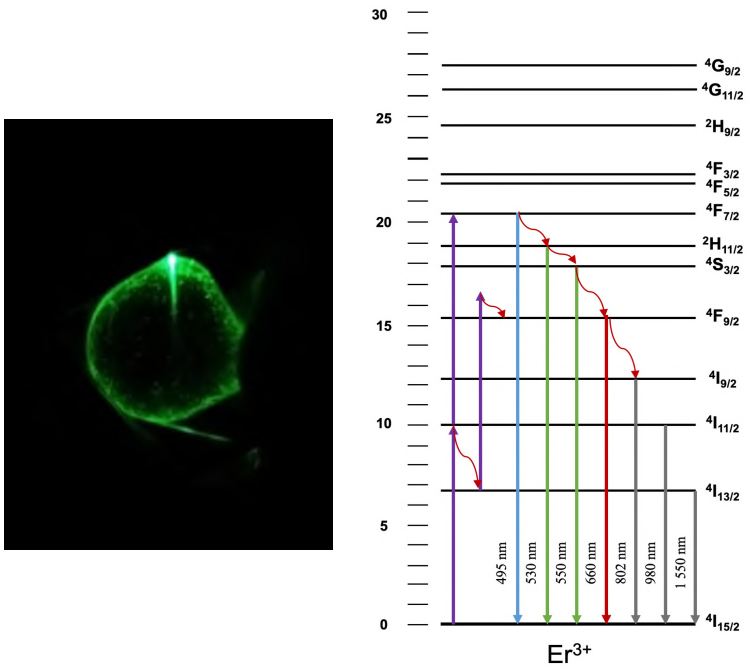

Fig. 34 Energy diagram of Er^{3+} with assigned luminescent and upconversion transitions observed in TeO_2-BaO-ZnO:Er glasses (right-hand side) and observed green upconversion emission in $T_{60}B_{20}Z_{20}$:$Er_{0.2}$ under 980 nm excitation

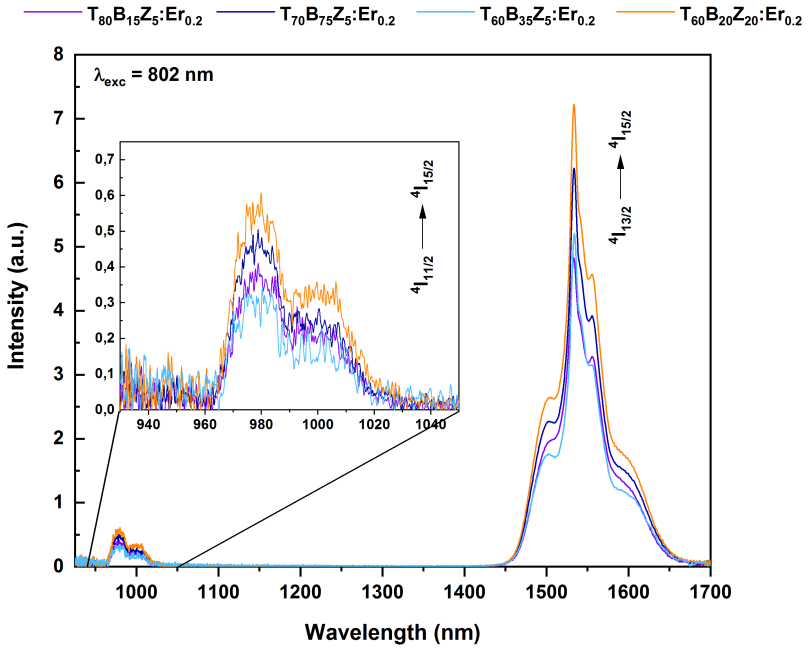

Fig. 35 Luminescence emission spectra of homogenous Er^{3+} doped TBZ samples under 802 nm excitation

The Er^{3+}: $^4I_{13/2} \rightarrow {}^4I_{15/2}$ (≈1.55 μm) and Er^{3+}:$^4I_{11/2} \rightarrow {}^4I_{15/2}$ (≈980 nm) Stokes emission spectra for $T_{80}B_{15}Z_5$:$Er_{0.2}$, $T_{70}B_{25}Z_5$:$Er_{0.2}$, $T_{60}B_{20}Z_{20}$:$Er_{0.2}$ and $T_{60}B_{35}Z_5$:$Er_{0.2}$ samples under 802 nm excitation are shown in Fig.35 and those excited by 980 nm are presented in Fig.36. Emission band centred at ≈980 nm seems to be weak due to the sensitivity limit of the used detector.

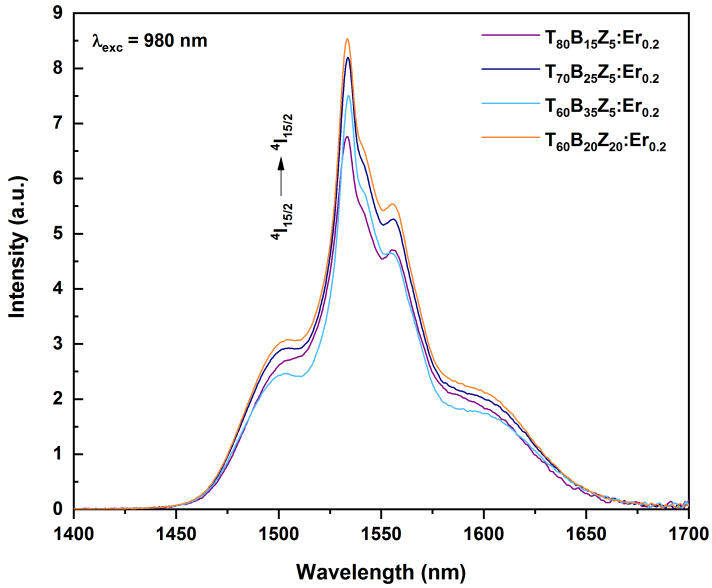

Fig. 36 Luminescence emission spectra of fully transparent Er^{3+} doped TBZ samples under 980 nm excitation

Luminescent emission spectra of $T_{60}B_{20}Z_{20}$:$Er_{0.2}$ excited by λ_{exc} = 802 nm using Ti:saphire laser at various pump powers are shown in the Fig.37. Observed emission bands originate from Er^{3+}: $^4I_{13/2} \rightarrow {}^4I_{15/2}$ (≈1.55 μm) and $^4I_{11/2} \rightarrow {}^4I_{15/2}$ (≈980 nm) intra-4f electronic transitions. It can be observed that the luminescent intensity increases with an increase in the pumping power.

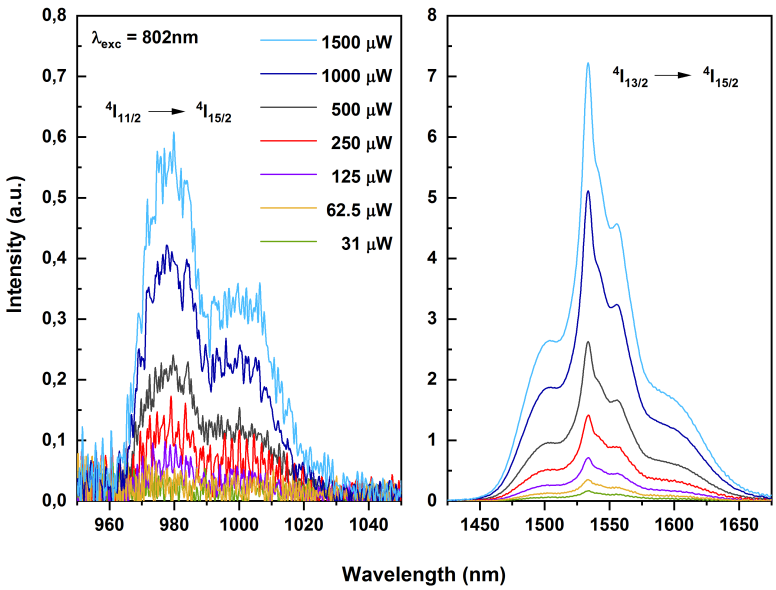

Fig. 37 Emission spectra of sample $T_{60}B_{20}Z_{20}$:$Er_{0.2}$ under 802 nm excitation for various pumping powers

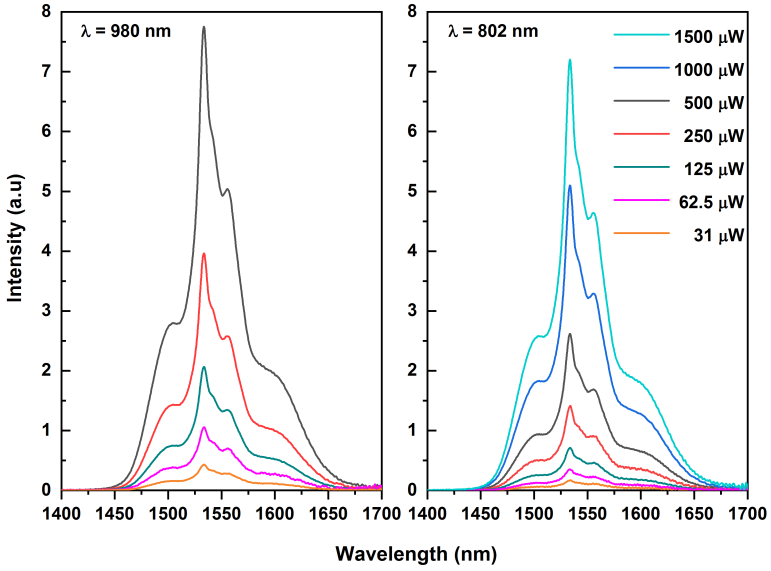

Fig. 38 Emission spectra of sample $T_{60}B_{20}Z_{20}$:$Er_{0.2}$ for various power excitations under 802 nm and 980 nm excitation

Luminescent emission spectra of $T_{60}B_{20}Z_{20}$:$Er_{0.2}$ excited by 802 nm and 980 nm using Ti:saphire laser for various pumping powers are shown in the Fig.38 for one observed emission band assigned to Er^{3+}: $^4I_{13/2} \rightarrow {}^4I_{15/2}$ (≈1.55 μm) intra-4f electronic transitions and exhibit increase in luminescent intensity with increasing pump power. Double logarithmic of 1550 nm luminescence intensity versus pump power is shown in Fig.41(a) The slope of the double logarithmic dependency provides the information on the number of photons involved in the photoluminescence process, i.e. $I \propto P^n$, where P is power, I is photoluminescence intensity and n_p is the number of photons [97]. Theoretically, the Stokes photoluminescence should be one-photon process which was confirmed experimentally in Fig.41 with obtained $n_p \cong 1$ under both excitations wavelength of 802 and 980 nm.

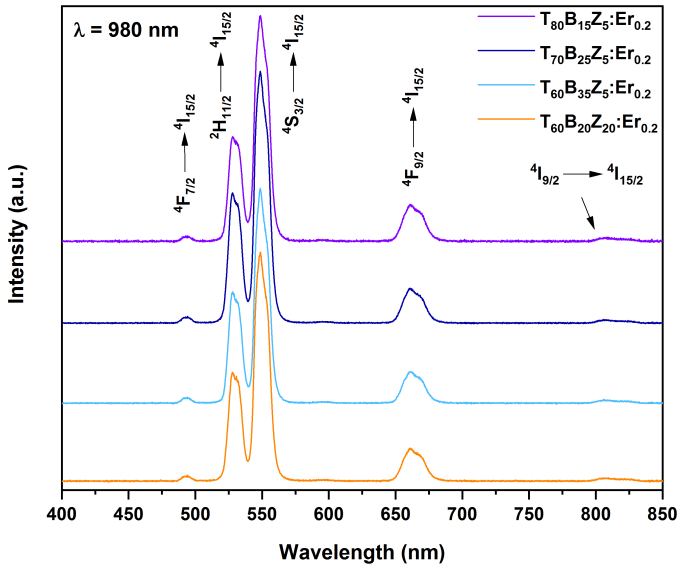

Fig. 39 Up-conversion emission spectra of fully transparent Er^{3+} doped TBZ samples under 802 nm excitation

Plausible upconversion emission spectra of $T_{80}B_{15}Z_5$:$Er_{0.2}$, $T_{70}B_{25}Z_5$:$Er_{0.2}$, $T_{60}B_{20}Z_{20}$:$Er_{0.2}$ and $T_{60}B_{35}Z_5$:$Er_{0.2}$ samples under 980 nm excitation are shown in Fig.39. Observed anti-Stokes emission bands were assigned to Er^{3+}: $^4I_{9/2}\rightarrow{}^4I_{15/2}$ (≈802 nm), $^4F_{9/2}\rightarrow{}^4I_{15/2}$ (≈660 nm), $^4S_{3/2}\rightarrow{}^4I_{15/2}$ (≈550 nm), $^2H_{11/2}\rightarrow{}^4I_{15/2}$ (≈530 nm) and $^4F_{7/2}\rightarrow{}^4I_{15/2}$ (≈490 nm) intra-4f electronic transitions. Dependence of upconversion emission on pumping power for sample $T_{60}B_{20}Z_{20}$:$Er_{0.2}$ is shown in Fig.40. It can be observed that the upconversion emission intensity increases with increasing pump power for all bands. Observed green emission up-conversion band centred at ≈550 nm is then dominantly stronger than the other observed up-conversion bands.

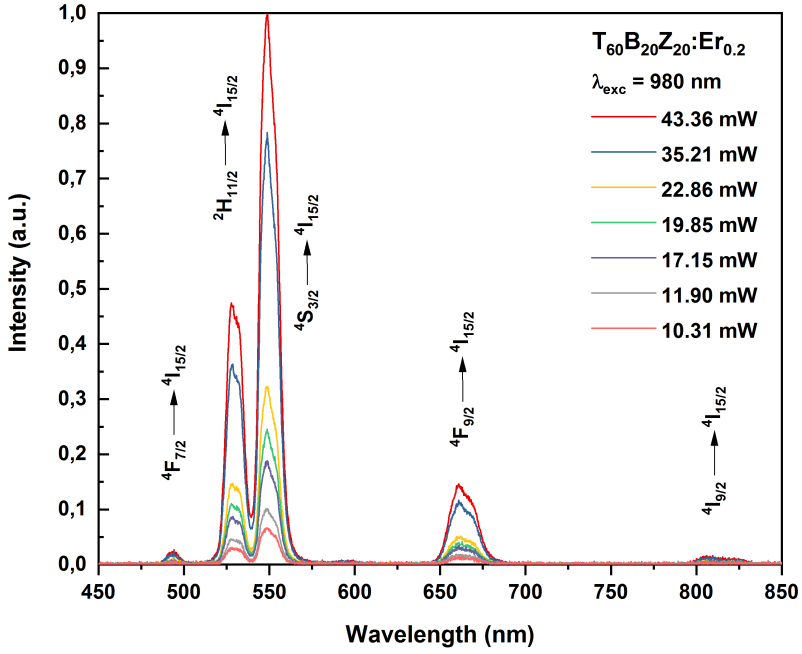

Fig. 40 Up-conversion emission spectra of sample $T_{60}B_{20}Z_{20}$:$Er_{0.2}$ under 980 nm excitation

The slope of double logarithmic dependency of upconversion photoluminescence intensity versus pump power may help to explore its dynamics. Mentioned dependencies for green (530 nm + 550 nm) and red (660 nm) upconversion emission under 980 nm excitation were plotted in Fig.41(b). The slopes of the red upconversion emission (≈660 nm) originating from Er^{3+}:$^4F_{9/2}\rightarrow{}^4I_{15/2}$ transitions are in range of $n_p \cong 1.25–1.74$ which manifests two-photon upconversion process. In the case of green (530 nm + 550 nm) upconversion emission the slope value of n_p was found in the range of 1.69–1.98 corresponding to two-photon process as well.

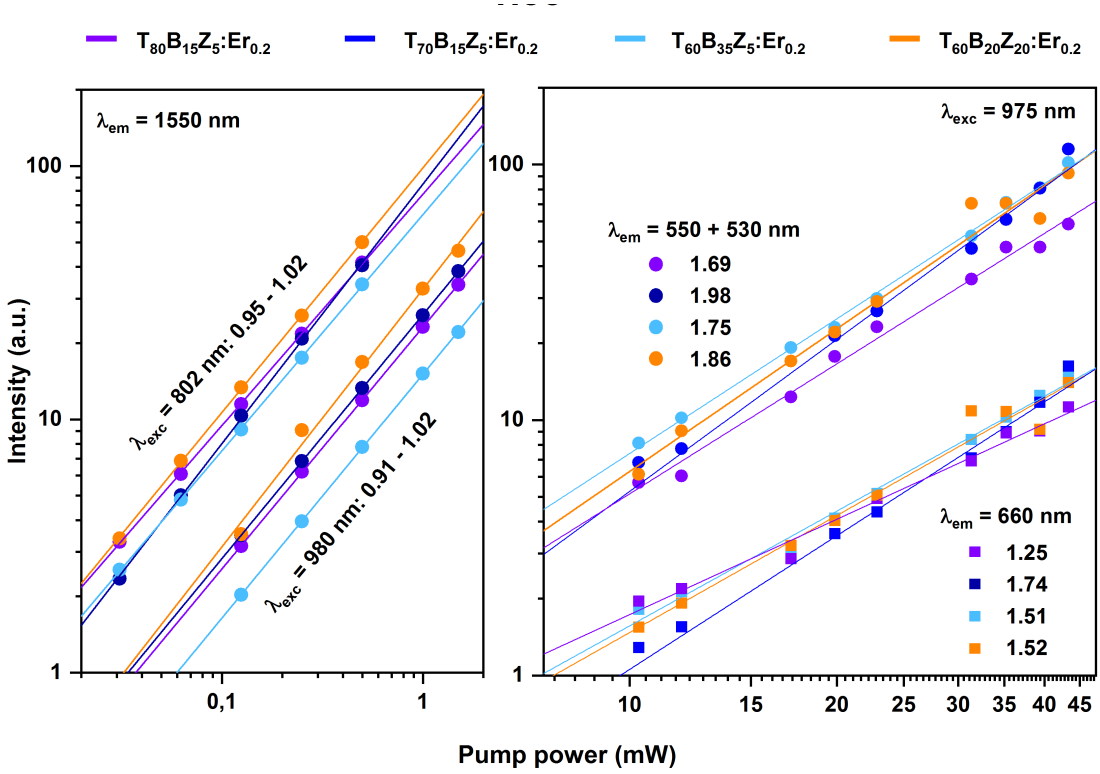

Fig. 41 Log-log plot of green a) - (530+550 nm), red (660 nm) photon up-conversion and b) - near-infrared (1550 nm) photoluminescent emission intensity as a function of 802 nm and 980 nm laser pumping in TBZ glasses doped with Er^{3+}

4.2.8 Judd-Ofelf theory

Judd-Ofelt phenomenological parameters Ω_2, Ω_4 and Ω_6 have been calculated from estimated absorption cross-section spectra for the 0.2 at.% Er-doped $T_{80}B_{15}Z_5$:$Er_{0.2}$, $T_{70}B_{25}Z_5$:$Er_{0.2}$, $T_{60}B_{35}Z_5$:$Er_{0.2}$ and $T_{60}B_{20}Z_{20}$:$Er_{0.2}$ samples. For calculations the $^4I_{15/2}\rightarrow{}^4I_{13/2}$ (~ 1.53 μm), $^4I_{15/2}\rightarrow{}^4I_{11/2}$ (~ 976 nm), $^4I_{15/2}\rightarrow{}^4F_{9/2}$ (~ 652 nm), $^4I_{15/2}\rightarrow{}^4S_{3/2}$ (~ 546 nm), $^4H_{11/2}\rightarrow{}^4I_{15/2}$ (~ 530 nm) and $I_{15/2}\rightarrow{}^4F_{7/2}$ (≈489 nm) absorption bands which originate in transparent spectral region of a host glass have been used. A weak intense Er^{3+} transitions such as Er^{3+}: $^4I_{15/2}\rightarrow{}^4I_{9/2}$ (~ 802 nm) were omitted in calculation. The hypersensitive transitions Er^{3+}: $^4I_{15/2} \rightarrow {}^2H_{11/2}$ were included in calculation to obtain the more precise Ω_2 parameter value.

Judd-Ofelt parameters play a fundamental part in study of the surrounding environemnt around the trivalent rare earth ions in the host matrix. The high value of JO parameter Ω_2 is related to the asymmetry at the RE^{3+} ions site and to its covalency. While Ω_2 is related to the asymmetry of the host glass, the Ω_6 is a measure of the covalency in the network [54,62,96,98–100]. The trend for the $\Omega_{2,4,6}$ parameters in the TBZ glassy system follow the $\Omega_2 > \Omega_6 > \Omega_4$ order. The Ω_2 and Ω_4 parameters decrease with higher TeO_2 or ZnO concentration. The opposite trend was observed for the Ω_6 Judd-Ofelt parameter. Obtained theoretical values

of branching ratios (β) and radiative lifetimes (τ^{JO}) for selected intra-4*f* Er^{3+} electronic transitions as well as derived Judd-Ofelt parameters are presented in Tab.10.

Tab. 10 Calculated branching ratios, lifetimes and Judd-Ofelt phenomenological parameters of prepared samples.

transition	**$T_{80}B_{15}Z_5$:$Er_{0.2}$**		**$T_{70}B_{25}Z_5$:$Er_{0.2}$**		**$T_{60}B_{35}Z_5$:$Er_{0.2}$**		**$T_{60}B_{20}Z_{20}$:$Er_{0.2}$**	
$^{2S+1}L_J \rightarrow {}^4I_{15/2}$	β	τ^{JO} (ms)	β	τ^{JO} (ms)	β	τ^{JO} (ms)	β	τ^{JO} (ms)
$^4I_{13/2}$	1.0000	2.3378	1.0000	2.6288	1.0000	2.8045	1.0000	2.8435
$^4I_{11/2}$	0.8620	1.7545	0.8608	1.9236	0.8636	2.0196	0.8657	2.0995
$^4I_{9/2}$	0.6673	2.0909	0.6780	2.3995	0.6758	2.3708	0.6294	2.6735
$^4F_{9/2}$	0.8908	0.2549	0.8944	0.2932	0.8911	0.2969	0.8935	0.3083
$^4S_{3/2}$	0.6673	0.1718	0.6677	0.1992	0.6691	0.2169	0.6882	0.1957
$^4H_{11/2}$	0.9495	0.0465	0.9512	0.0471	0.9536	0.0450	0.9552	0.0488
$^4F_{7/2}$	0.8142	0.0901	0.8018	0.1036	0.8014	0.1083	0.8403	0.1010
$\Omega_2 \cdot 10^{-20}$ (cm^2)	7.5923 ± 0.5220		8.8183 ± 0.4980		9.9898 ± 0.5694		7.5372 ± 0.4490	
$\Omega_4 \cdot 10^{-20}$ (cm^2)	1.5710 ± 0.5953		1.5921 ± 0.5680		1.8034 ± 0.6494		1.3172 ± 0.5120	
$\Omega_6 \cdot 10^{-20}$ (cm^2)	2.024 ± 0.1995		2.0174 ± 0.1903		2.0075 ± 0.2176		1.9063 ± 0.1716	
RMS	0.2900		0.2767		0.3163		0.2494	

5 CONCLUSIONS

This work deals with a complex study of ternary oxide glassy system of the TeO_2-BaO-ZnO (TBZ). The thesis was divided into two parts. First part was focused on structural, thermal and optical properties of undoped TBZ glasses as the potential materials for applications in photonics. In the second part of work, the doping of TBZ glasses with Er^{3+} ions with respect to their structural, thermal and optical properties was investigated.

Glass-forming region was investigated through the preparation of 27 bulk TBZ glasses. Glasses prepared in platinum crucible had typical yellowish colour while glasses prepared in the alumina crucible are colourless. The amorphous state of prepared glasses was verified using X-ray diffraction analysis. Prepared glasses show wide optical window from UV to MIR part of electromagnetic spectrum (0.4–6.2 μm), which did not shift significantly with the concentration of BaO and ZnO modifiers. The structure of glassy network was studied via Raman scattering. It was observed, that the addition of modifiers leads to an increase of non-bridging oxygens in glassy network resulting in observation of TeO_{3+1} and TeO_3 vibrational units.

The thermal properties have been studied by the differential thermal analysis and differential scanning calorimetry. The glass transition temperature ($T_g \approx 319$–369 °C) significantly increases with the higher BaO and ZnO content and a lower concentration of TeO_2 which is discussed in term of bond strengths and molar volume of TBZ glasses. The decrease in TeO_2 concentration for central composition tie line results in increase of glass transition temperature with a step of approximately +10 °C per decrease of 10 mol.% of TeO_2. Crystallization behaviour seems to be oriented more on the surface than internal crystallization. Prepared glasses with observable crystallization peak have shown good thermal stability, where the thermal coefficient was estimated as $\Delta T \geq 100$ °C. The differences in thermal properties between synthesis of TBZ glasses in Pt or Al_2O_3 crucible was studied as well. Samples synthesized in alumina crucible possess higher glass transition temperature than those synthesized in Pt crucible. This behaviour was addressed to differences in molar volume. The measured density of prepared glasses decreases with increasing concentration of BaO and decreasing concentration of TeO_2, which is attributed to the radius of cations. PCR and ellipsometry measurements showed that the refractive index of TBZ glasses increases with: 1) substitution of ZnO by TeO_2, 2) substitution of BaO by TeO_2, and 3) substitution of BaO by ZnO. Such behaviour is explained on the basis of changes in molar volume of TBZ glasses. Compositional evolution of refractive index seems to be linear, which providesthe opportunity

to prepare TBZ glasses of the desired refractive index. Refractive index values obtained from PCR as well as ellipsometry are in very good agreement however, the advantage of ellipsometry is possibility to measure dispersion of refractive index at high number of wavelengths. Optical band gap energy E_g derived from ellipsometry data analysis increases with decreasing TeO_2 concentration and increasing BaO content.

For the study of applicability of TBZ glasses for photoluminence, the selected samples were doped with 0.2 at.% of Er^{3+} ions. Nine bulk glassy samples with typical pink colour were prepared. Samples $T_{80}B_{15}Z_5$:$Er_{0.2}$, $T_{70}B_{25}Z_5$:$Er_{0.2}$, $T_{60}B_{35}Z_5$:$Er_{0.2}$ and $T_{60}B_{20}Z_{20}$:$Er_{0.2}$ were homogeneous while the the rest of them were opaque. The amorphous state of Er-doped glasses was investigated by XRD analysis, their chemical composition by the EDX spectroscopy.

In comparison to undoped TBZ samples, the temperatures of glass transition increased in the range from 11 to 21 °C depending on the composition. Observed difference was explained as the function of used crucible for synthesis. Refractive index and optical band gap energy E_g were obtained by analysis of spectroscopic ellipsometry data.

The UV-Vis-NIR spectra of all studied Er^{3+}-doped TBZ glasses exhibit ten common Er^{3+} ground state absorption bands from ground state Er^{3+}:$^4I_{15/2}$ to $^4I_{13/2}$ (≈1.53 μm), $^4I_{11/2}$ (≈976 nm), $^4I_{9/2}$ (≈802 nm), $^4F_{9/2}$ (≈652 nm), $^4S_{3/2}$ (≈546 nm), $^2H_{11/2}$ (≈522 nm), $^4F_{7/2}$ (≈489 nm), $^4F_{5/2}$ (≈450 nm), $^2H_{9/2}$ (≈406 nm) and $^4G_{11/2}$ (≈378 nm) energy levels.

The intensities of the Er^{3+} intra-4*f* electronic transitions were calculated on the basis of the Judd-Ofelt theory from which the phenomenological parameters Ω_2, Ω_4 and Ω_6 have been determined. The branching ratios and radiative lifetimes of Er^{3+} intra-4*f* transitions for different TBZ:Er^{3+} glasses have been determined as well.

In the photoluminescence emission spectra of TBZ:Er^{3+} glasses was observed intense Stokes (1.55 μm) and upconversion photoluminiescence emission from visible to near-infrared spectral region (802 nm, 660 nm, 550 nm, 530 nm, 495nm) which make these glasses promising in photoluminescence applications however further study for exploration of the upconversion dynamics is highly desirable.

In conclusion, the RE^{3+}-doped TeO_2-BaO-ZnO glasses are promising materials for photonics applications due to their good thermal stability, broad spectral transparency from visible up to mid-infrared spectral region and large refractive index resulting in intense photoluminescence emission. The applicability of these glasses may be seen in the manufacturing of optical fiber amplifiers, lasers, sensors and detectors.

6 REFERENCES

[1] R.A.H. El-Mallawany, *Tellurite glasses Handbook, Physical properties and data (second edition)*. London : CRC Press, 2012. 13:978-1-4398-4984-2(eBook).

[2] J.S. Wang, E.M. Vogel, E. Snitzel, J.L. Jackel, V.L. da Silva, Y. Silberberg, *1.3 um emission of neodymium and praseodymium in tellurite-based glasses.,* J. Non.-Cryst. Solids, 178 (1994), pp. 109-113.

[3] H. Burger, K. Kneipp, H. Hobert, W. Vogel, V. Kozhukarov, S. Neov S., *Glass formation, properties and structure og glasses in the TeO_2-ZnO system.* J. Non.-Cry. Sol. , 151 (1992), pp. 134-142

[4] N. Manikandan, A. Ryasnuanskiy, J. Toulouse, *Thermal and optical properties of TeO_2-BaO-ZnO glasses.*, J. Non.-Cryst. Solids., 358 (2012) pp. 947-951

[5] M. Mochida, K. Takashi, K. Nakata, S. Shibusawa, *Properties and Structure of the Binary Tellurite Glasses Containing Mono-and Di-valent Cations,* J. Ceram. Assoc. Jpn., 86 (1978) 995 pp. 316-326

[6] S. Sakida, S. Hayakawa, T. Yoko, *^{125}Te NMR Study of MO-TeO2 (M=Mg, Zn, Sr, Ba and Pb) Glasses*, J. Ceram. Soc. Jpn., 107 (1999) 5 pp. 395-402

[7] S. Sakida, S. Hayakaw, T. Yoko, *Part.1. ^{125}Te NMR study of tellurite crystals.* J. Non.-Cryst. Sol., 243(1999) 1 pp. 1-12,

[8] A. Feltz, *Amorphous Inorganic materials and glasses.* New York : Weinheim/VCH Publishers, 1993, 3-527-28421-4.

[9] N.F. Mott, E.A. Davis *Electron processes in non-crystalline materials.* London : Oxford University Press, 1971, 9780199645336

[10] J.W.Schmelzer, *Kinetic criteria of glass formation and pressure dependence of the glass transition temperature,* J. Chem. Phys., 136 (2012) 7

[11] M. Frumar, *Chemie pevných látek I. (úvod)*. Pardubice : VŠCHT Pardubice, 1992, 80-85113-41-4.

[12] V.M. Goldsmidt, *Geochemische Verteilungsgesetze der Elemente,* Skifter Norske Videnskaps, 1926.

[13] L. Sodomka, *Fyzika a chemie kondenzovaných látek s aplikacemi 2 (1.vyd.),* Liberec, Adhesiv, 2004. 80-239-1417-0.

[14] A.A. Lebedev*, Trudy. Cossud.* Opt. Inst., 57 (1921) 2.

[15] W.H. Zachariasen*, The atomic Arrangement in Glass, J. Am. Chem. Soc., 54(1932) 10 pp. 3841-3851.*

[16] P. Patnaik*, Handbook of Inorganic Chemicals,* New York, The McGraw-Hill Companies, 2002, 0-07-049439-8.

[17] *J.E. Stanworth., Tellurite Glasses., Nature, 169 (1952) pp.581-582*

[18] G.W. Brady, *X-ray Study of Tellurium Oxide Glass.,* J. Chem. Phys., 24(1956) 477

[19] *G.W. Brady***,** *Structure of Tellurium Oxide Glass,* J. Chem. Phys., 27(1957) 300

[20] V. Chereminsinov, V. Zalomanov, Opt.Spectrosc., 12(1962) 110

[21] O. Lanquist., Acta. Chem. Scand. . 977, 22(1968) 977

[22] B. Warren**,** *The basic Principles Involved in the Glassy State*, J. Appl. Phys., 13 (1942) 602

[23] T. Sekiya, N. mochida, A. Ohtsuka, M. Tonokawa**,** *Normal Vibrations of Two Polymorphic forms of TeO_2 Crystals and Assignments of Raman Peaks of Pure TeO_2 glass,* Nippon Seramikkusu Kyokai Rinbunshi, 97 (1989) 12 pp.1435-1440

[24] T. Sekya, N. Mochida, A. Ohtsuka, M. Monokawa., *Raman Spectra of $Mo_{1/2}TeO_2$ (M = Li, Na, K, Rb, Cs and Th) glasses*, J. Non.-Cryst. Solids, 144(1992) p. 128-144

[25] S. Manning, H. Ebendorf-Heidepriem, T. Monroe, *Ternary tellurite glasses for the fabrication of nonlinear optical fibres,* Optical Materials Express, 2 (2012) 2 pp. 140-152
[26] C. Blanchetier, K. Le Foulgoc, H.L. Ma, X.H. Zhang, J. Lucas, *Tellurium halide glass fibers: preparation and applications,* J. Non.-Cryst- Solids, 184 (1995) pp. 200-203
[27] A. Mirgorodsky, T. Merle-Mjean, J.-C.Champarnaud, P. Thomas, B. Frit, *Dynamics and structure of TeO_2 polymorphs: model treatment of paratellurite and tellurite; Raman scattering evidence for new gama- and delta-phases,* J. Phys. Chem. Solids, 61 (2000) 4 pp.501-509
[28] O. Noguera, T. Merle-Mjean, A. Mirgorodsky, M. Smirnov, P. Thomas, J.C.Champarnaud-Mesjard, *Vibrational and structural properties of glass and crystalline phase of TeO_2,* J. Non.-Cryst. Solids, 330 (2003) 1-3 pp.50-60
[29] T. Sekiya, N. Mochida, A. Ohtsuka, *Raman Spectra of MO-TeO_2 (M = Mg, Sr, Ba, Zn) glasses*, J. Non.-Cryst. Solids, 168(1994) 1-2 pp.106-114
[30] H.M.M Moawad, H. Jain, R. El-Mallawany, *DC conductivity of silver vanadium tellurite glasses,* J. Phys. Chem. Solids, 70(2009) 1 pp.224-233
[31] R. Stegeman, L. Jankovic, H. Kim, C. Rivero, G. Stegeman, K. Richardson, Delfyett, Y. Guo, A. Schulte, T. Cardinal, *Tellurite glasses with peak absolute Raman gain coefficients up to 30 times than of fused silica,* Opt. Lett., 28(2003) 13 pp.1126-1128.
[32] A.E. Miller, K. Nassau, K.B. Lyons, M.E. Lines, *The intensity of Raman scattering in glasses containing heavy metal oxides*, J. Non.-Cryst. Solids, 99 (1988) 2-3 pp.289-307
[33] E. Lambson, S. Saunders, B. Bridge, R. El-Mallawany, *The elastic bahavior of TeO_2 glass under uniaxial and hydrostatik pressure, J. Non.-Cryst. Solids, 69 (1984) pp.117-134.*
[34] N.S. Tagiara, D. Palles, E.D. Simandiras, V. Psycharis, A. Kyritsis, E.I. Kamitsos, *Synthesis, thermal and structural properties of pure TeO_2 glass and zinc-tellurite glasses,* J. Non.-Crys. Sol., 457 (2017) pp.116-125
[35] P.T. Sarjeant, R. Rustum, *New glassy and polymorpic oxide phases using rapid Quenching Techniques,* J. Am. Ceram. Soc., 50(1967) 10 pp.500-503
[36] E.R. Barney, A.C. Hannon, D. Holland, N. Umesaki., M. Tatsumisago, R. G Orman, S. Feller, *Terminal oxygens in amorphous TeO_2,* J. Phys. Chem. Lett., 4 (2013) 14 pp.2312-2316
[37] V. Kozhokarov, M. Marinov, J. Pavlova, J. Mater. Sci., 13 (1978) 977
[38] V.G. Plotnichenko, V.V. Koltashev, V.O. Sokolov, N.V. Popova, I.A. Grishin, M.F. Churbanov, *Spectroscopic properties of new $BaCl_2$-BaO-TeO_2 tellurite glasses for fibre and integrated optics applications*, J. Phys. D: Appl. Phys., 41(2008) 015404
[39] H. Desirena, A. Schulzgen, S. Sabet, G. Ramos-Ortiz, E. Rosa, N. Peyghambarian, *Effect of alkali metal oxides R_2O (R = Li, Na, K, Rb,and Cs) and network intermediate MO (M = Zn, Mg, Ba and Pb) in tellurite glasses,* Opt. Mat., 31(2009) 6 pp.784-789
[40] S. Shu, F. Chang, Solid state ionics, 176 (2005), 2695
[41] M. Redman, J. Chen, *Zinc Tellurite Glasses*, J. Am. Ceram. Soc., 50 (1967) 10 p.523-525.
[42] H. Rawson, *Inorganic Glass-Forming systems,* Academic Press London, 1967
[43] W. Vogel, H. Burger, B. Muller, K. Forkel, *Untersuchengen an Telluritglasern* Silikattechnik, 25 (1974) pp.205-209
[44] W. Vogel, *Chemistry of glass,* Westerville (OH) : American Ceramics Society:, 1985. 0916094731 9780916094737.
[45] K. Nakashima, T. Miyazaki, T. Takaki, *Diagrams for the Glass-forming system MO-TeO_2(M: Ba, Sr)*, J. Japan Ins. Metals, 52 (1988) 454459

[46] R. Mishra, S. Phapale, P. Samui, A. Nagaraj, S.R. Dharwadkar, *Partial phase diagram of BaO-TeO_2 system*, ASM International, 35 (2014) 2 pp.127-136
[47] M. Imaoka, T. Yamazaki, *Studies of the Glass-foramtion Range of Tellurite Systems*, J. Ceram. Assoc. Japan., 76 (1968) 873 pp.160-172
[48] B. Zhou, F. C. Rapp, K.J. Driver, M.J. Myers, J.D. Myers, J. Goldstein, R. Utano, S. Gupta, *Development of tellurium oxide and lead-bismuth oxide glasses for mid-wave infra-red transmission optics*, Proc. of SPIE, 8626 (2013)
[49] P. Yasaka, Y. Ruangtaweep, P. Mangthong, J. Kaewkhao, *Physical and optical investigation of ZnO-BaO-TeO_2 glass system., Materials Today: Proceedings, 5 (2018) 5 pp.14199-14203*
[50] P. Yasaka, Y. Ruangthweep, C. Wongdeeing, Herman, J. Kaewkhao, *Spectroscopic and structural characterization of zinc barium tellurite glass*, Materials Today: Proceedings , 5 (2018) p.15072-15075
[51] K. Boonin, P. Yasaka, J. Kaewkhao, *Optical and Luminescence Characteristic of Dy^{3+} doped ZnO-BaO-TeO_2 glass system*, Applied Mechanics and Materials, 431 (2013) pp.27-31
[52] Y. Ruangtaweep, P. Yasaka, J. Rajagukguk, J. Kaewkhao, *Influence of silver nanoparticles on the Dy^{3+} luminescence properties in TeO_2-ZnO-BaO glasses,* Materials Today: Proceedings, 5 (2018) pp.15014-15018
[53] P. Yasaka, Y. Ruangthaweep, J. Kaewkhao, *Study on physical and Photoluminescence Properties of Er^{3+} doped Zinc Barium Tellurite Glasses*, Key Engineering Materials, 728 (2016) pp.155-159
[54] M.S. Gaafar, S.Y. Marzouk, *Judd-Ofelt analysis of spectroscopic properties of Er^{3+} doped TeO_2-BaO-ZnO glasses,* J. All. Comp. , 723 (2017) p.1070-1078
[55] J. Singh, K. Shimakawa**,** *Advances in amorphous semiconductors. [editor]* G. Kotliar, Y. Tokura D.D. Sarma. London : Taylor & Francis, 2003. 0-415-28770-7.
[56] S. Kugler, K. Shimakawa, *Amorphous Semiconductors,* Cambridge : Cambridge university press, 2015. 978-1-107-01934-8.
[57] F. Urbach, *The Long-Wavelength Edge of Photographic Sensitivity and of the Electronic Absorption of Solids,*Phys. Rev., 92 (1953)
[58] K. Shimakawa, J. Singh, S. K. O'Leary, *Optical Properties of Condensed Matter and Applications: Optical properties of disordered condensed matter,* Wiley, 2006. 9780470021927.
[59] D.L. Wood, J. Tauc. *Weak Absorption Tails in Amorphous Semiconductors,* Physical Review. 8 (1972) 5.
[60] F.A. Jenkins, H.E. White, *Fundamentals of optics. Third edition.* York : McGraw-Hill book company, Inc., 1957.
[61] R. M. Martin, *Reciprocity between Emission and Absorption for Rare Earth Ions in Glass. PhD. thesis. Worcester : Worchester Polytechnic Institute, 2006.*
[62] B.M., Walsh. *Advances in Spectroscopy for Lasers and Sensing: Judd-Ofelt theory: principles and practices.* Dordrecht: Springer, 2006. 978-1-4020-4789-3.
[63] A.D. McNaught, A. Wilkinson, *Compendium of Chemical Terminology, 2nd ed. (online)*: IUPAC, 1997. 0-86542-648-8.
[64] I. Pelant, J. Valenta*, Luminiscenční spektroskopie I. Objemové polovodiče,* Praha: ACADEMIA, 2006. 80-200-1447-0.
[65] I. Pelant, J. valenta., *Luminiscenční spektroskopie II. Nanostruktury, elektroluminiscence, stimulovaná emise,* Praha ACADEMIA, 2010. 978-80-200-1846-5.
[66] F. Auzel, *Upconversion and Anti-stokes Processes with f and d ions in Solids.,* Chem. Rev., 104 (2004). 1 pp 139-174

[67] *B.R. Judd, Optical Absorption Intensities of Rare-Earth ions,* Phys. Rev. 127 (1962) 750
[68] G.S. Ofelt, *Intensities of Crystal Spectra of Rare Earth-Ions.,* J. Chem Phys., 37 (1962) 511
[69] B. Di Bartolo, O. Forte, *Advances in Spectroscop for lasers and Sensing.:* Dordrecht: Springer (Published in cooperation with NATO Public Diplomacy Division), 2006.
[70] K.A. Gschneidner Jr., L. Eyring, *Handbook on the Physics and Chemistry of Rare Earths. Amsterdam : Elsevier, 1999. 978-0-444-50185-1*
[71] R. Shuker, R.W. Gammon, *Raman-Scattering Selection-Rule Breaking and the Density of States in Amorphous Materials,* Phys. Rev. Lett. , 25 (1970) 222
[72] N.M. Temme, *NIST Handbook of Mathematical Functions*. Cambridge : Cambridge University Press, 2010. 978-0521192255.
[73] G.E. Jellison Jr., F.A. Modine, *Parametrization of the optical functions of amorphous materials in the iterband region*, Appl Phys. Lett., 69 (1996) 2137
[74] G.E. Jellison Jr., F.A. Modine, *Erratum: "Parametrization of the optical functions of amorphous materials in the interband region"*, Appl. Phys. Lett., 69 (1996) 2137
[75] D.A.G., Bruggeman, *Berechnung verschiedener physikalischer Konstanten von heterogenen Substanzen. I. Dielektrizitatskonstanten und Leitfahigkeiten der Mischkorper aus isotropen Substanzen*, Ann. Phys., 24 (1935) 636
[76] K. Tanaka, K. Shimakawa, *Amorphous Chalcogenide Semiconductors and Related Materials*, New York : Springer, 2011. 978-1-44199509-4.
[77] J. Faber, T. Fewcett, *The Powder Diffraction File: present and future*, Acta Cryst., B58 (2002) pp. 325-332.
[78] E.R. Shaaban, Y.B. Saddeek, M. Abdel Rafea, *Crystalization kinetics of the TeO_2-BaO glass system*, Philosophical Magazine, 89 (2009) pp. 27-39
[79] D.R. Lide, *Handbook of Chemistry and Physics.*, CRC Press. Boca Raton, 2001.
[80] J. B. Pedley, E. M. Marshall, *Themochemical data for Gaseous Monoxides*, J. Phys. Chem. Ref. Data, 12 (1984) 967
[81] D.E. Clemmer, N.F. Daltaska, P.B. Armentrout, *Reaction of Zn+ with NO_2. The gas-phase thermochemistry of ZnO*, J. Chem. Phys., 5 (1991) 7263
[82] C.S. Ray, Q. Yang, W.-H. Huang, D.E. Day, *Surface and internal Crystalization in Glasses as Determined by Differential Thermal Analysis*, J. Am. Ceram. Soc., 79 (1996) pp. 3155-3160
[83] A.F. Wells, *Structural Inorganic Chemistry,* 5th ed., Clarendon Press, Oxford. 1984, 0198553706
[84] V. Dimitrov, T. Komatsu, *Electronic polarizability, optical basicity and non-linear optical properties of oxide glasses*, J. Non.-Cryst. Solids, 249 (1999) pp.160-179
[85] O. Mossotti, *Mem. e Fisica di Modena.* 24 (1850) 49
[86] R. Clausius, *Die Mechanishe Wärmlehre*, Vol. II. Brunswick: Vieweg-Verlag. 1879.
[87] L. Lorentz. *Experimentale og theoretiske Undersogelser over Legemernes Brydningsforhold,* Vidensk Sisk Sckrifter, 8 (1870) 205
[88] V. Dimitrov, S. Sakka, *Electronic oxide polarizability and optical basicity of simple oxides*. J. Appl. Phys., 79 (1996) 1736
[89] V. Nazabal, S. Todoroki, A. Nukui, T. Matsumoto, S. Suehara, T. hondo, T. Araki, S. Inoue, C. Rivero, T. Cardinal, *Oxyfluoride tellurite glasses doped by erbium: thermal analysis, structural organisation and spectral properties,* J. Non.-Cryst. Solids, 325 (2003) pp. 85-102.
[90] R.V. Adams, *Infrared absorption due to water in glasses, Phys. Chem. Glasses 2 (1961) 50 pp.39-49*
[91] M. Arnaudov, Y. Dimitriev, V. Dimitrov, M. Dimitrovapankova, *Infrared spectral investigations of water in tellurite glasses,* Phys. Chem. Glasses 27 (1970) pp.48-50

[92] L.M. Ovecoglu, M.R. Ozalp, G. Ozen, F. Altin, V. Kalem, Crystallization Behaviour of Some TeO_2-ZnO Glasses., Key Engineering Materials, 264-265 (2004) pp. 1891-1894

[93] *L. Zhang, H. Hu, C. Qi, F. Lin, Spectroscopic properties and energy transfer in Yb^{3+}/Er^{3+} - doped phosphate glasses., Opt. Mater., 17 (2001) pp. 371-377.*

[94] H. Ebendorff-Heidepriem, D. Ehrt, J. Philipps, T. Toepfer, A. Speghini, M. Bettinelli M., R. Wong, *Properties of Er^{3+}-doped glasses for waveguide and fiber lasers.,* Proc. SPIE - The International Society for Optical Engineering , 29 (2000) 3942

[95] V.D. Rodriguez, I.R. Martin, R. Alcala, , R. Cases, *Optical properties and cross realxation among m^{3+} ions in fluorzincate glasses.,* J. Lumin, 54 (1992) pp. 231-236

[96] W.T. Carnall, P.R. Fields. K. Rajnak, *Electronic energy levels in the trivalent lanthanide aquo ions: Pr^{3+}, Nd^{3+}, Pm^{3+}, Sm^{3+}, Dy^{3+}, Ho^{3+}, Er^{3+} and Tm^{3+},* J. Chem. Physics., 49 (1968) pp. 4424-4442

[97] M. Pollnau, D.R. Gamelin, S.R. Luthi, H.U. Gudel, M.P. Hehlen, *Power dependence of upconversion luminescence in lanthanide and transition-metal-ion systems.,* Phys. Rev. B, 61 (2000) pp. 3337-3346

[98] E.S. Sazali, R. Sahar, S.K. Ghoshal, S. Rohani, R. Arifin, *Judd-Ofelt intensity parameters of barium doped lead tellurite glasses, J.Non-Oxide.Glas., 6 (2014) pp.61-67*

[99] R. Rolli, M. Montagna, S. Chaussedent, A. Monteil, V.K. Tikhomirov, M. Ferrari, *Erbium-doped tellurite glasses with high quantum efficiency and broadband stimulated emission cross section at 1.5 μm,* Opt. Mat., 21 (2003) pp. 743-748

[100] S. Bhardwaj, R. Shukla, S. Sanghi, A. Agarwal, I. Pal, *Spectroscopic properties of Sm^{3+} doped lead bismosilicate glasses using Judd-Ofelt theory,* Spectrochim. Acta Part 117 (2014) pp.191-197

7 APPENDIX

AP.1. *Calculated linestrength (S_{ED}),electric (A_{ED}) and magnetic (A_{MD}) transition probabilities, branching ratios, and calculated radiative lifetimes τ^{JO} (ms) of intra-4f eletronic transitions derived from JO analysis for sample $T_{60}B_{35}Z_5:Er_{0.2}$*

intra-4f transition	λ (nm)	S_{ED}	A_{ED} (s^{-1})	A_{MD} (s^{-1})	β (%)	τ^{JO} (ms)
$^4F_{7/2}\rightarrow{}^2H_{11/2}$	7429	2.0616	2.845	0	< 1%	351.5220
$^4F_{7/2}\rightarrow{}^4S_{3/2}$	4666	0.0111	0.062	0	0	344.0262
$^4F_{7/2}\rightarrow{}^4F_{9/2}$	1910	0.2132	17.326	20.065	< 1%	24.8154
$^4F_{7/2}\rightarrow{}^4I_{9/2}$	1245	1.1932	350.369	21.379	4.02	2.4269
$^4F_{7/2}\rightarrow{}^4I_{11/2}$	979	0.8168	494.899	0	5.36	1.1026
$^4F_{7/2}\rightarrow{}^4I_{13/2}$	720	0.6082	927.535	0	10.04	0.5451
$^4F_{7/2}\rightarrow{}^4I_{15/2}$	491	1.5227	7403.212	0	80.14	0.1083
$^2H_{11/2}\rightarrow{}^4S_{3/2}$	12547	0.3789	0.072	0	0	13819.0482
$^2H_{11/2}\rightarrow{}^4F_{9/2}$	2571	3.6702	81.475	0.255	< 1%	12.2245
$^2H_{11/2}\rightarrow{}^4I_{9/2}$	1496	2.7672	312.195	1.118	1.41	2.5309
$^2H_{11/2}\rightarrow{}^4I_{11/2}$	1127	0.6804	179.719	13.990	< 1%	1.6983
$^2H_{11/2}\rightarrow{}^4I_{13/2}$	798	0.4464	333.809	110.140	2.00	0.9683
$^2H_{11/2}\rightarrow{}^4I_{15/2}$	525	8.0475	21210.394	0	95.36	0.0450
$^4S_{3/2}\rightarrow{}^4F_{9/2}$	3234	0.0535	1.791	0	< 1%	558.4951
$^4S_{3/2}\rightarrow{}^4I_{9/2}$	1699	0.6526	150.856	0	3.27	6.5511
$^4S_{3/2}\rightarrow{}^4I_{11/2}$	1238	0.1560	93.141	0	2.02	4.0685
$^4S_{3/2}\rightarrow{}^4I_{13/2}$	852	0.6952	1279.803	0	27.76	0.6555
$^4S_{3/2}\rightarrow{}^4I_{15/2}$	548	0.4439	3084.205	0	66.91	0.2169
$^4F_{9/2}\rightarrow{}^4I_{9/2}$	3578	1.3444	13.292	4.533	< 1%	56.1012
$^4F_{9/2}\rightarrow{}^4I_{11/2}$	2007	3.3003	185.005	10.905	5.82	4.6787
$^4F_{9/2}\rightarrow{}^4I_{13/2}$	1156	0.5207	152.947	0	4.54	2.7272
$^4F_{9/2}\rightarrow{}^4I_{15/2}$	660	1.8926	3001.329	0	89.11	0.2969
$^4I_{9/2}\rightarrow{}^4I_{11/2}$	4570	0.4067	1.929	1.937	< 1%	258.6556
$^4I_{9/2}\rightarrow{}^4I_{13/2}$	1708	1.4610	132.899	0	31.51	7.3118
$^4I_{9/2}$- $^4I_{15/2}$	810	0.3323	285.041	0	67.58	2.3708
$^4I_{11/2}$- $^4I_{13/2}$	2727	2.8197	52.473	15.055	13.64	14.8087
$^4I_{11/2}\rightarrow{}^4I_{15/2}$	984	1.0757	427.609	0	86.36	2.0196
$^4I_{13/2}\rightarrow{}^4I_{15/2}$	1539	3.2804	291.314	65.251	100	2.8045

AP.2 *Calculated linestrength (S_{ED}),electric (A_{ED}) and magnetic (A_{MD}) transition probabilities, branching ratios, and calculated radiative lifetimes τ^{JO} (ms) of intra-4f eletronic transitions derived from JO analysis for sample $T_{70}B_{25}Z_5:Er_{0.2}$*

intra-4f transition	λ (nm)	S_{ED}	A_{ED} (s^{-1})	A_{MD} (s^{-1})	β (%)	τ^{JO} (ms)
$^4F_{7/2}\rightarrow{}^2H_{11/2}$	7396	1.9184	2.9	0	< 1%	345.8378
$^4F_{7/2}\rightarrow{}^4S_{3/2}$	4739	0.0098	0.1	0	0	339.2331
$^4F_{7/2}\rightarrow{}^4F_{9/2}$	1904	0.1919	16.9	21.567	< 1%	24.1096
$^4F_{7/2}\rightarrow{}^4I_{9/2}$	1241	1.1582	370.6	23.024	4.08	2.2982
$^4F_{7/2}\rightarrow{}^4I_{11/2}$	979	0.7583	494.8	0	5.13	1.0753
$^4F_{7/2}\rightarrow{}^4I_{13/2}$	720	0.5370	882.0	0	9.14	0.5519
$^4F_{7/2}\rightarrow{}^4I_{15/2}$	491	1.4978	7839.5	0	81.23	0.1036
$^2H_{11/2}\rightarrow{}^4S_{3/2}$	13193	0.3370	0.060	0	0	16757.0990
$^2H_{11/2}\rightarrow{}^4F_{9/2}$	2565	3.2403	78.1	0.274	< 1%	12.7452
$^2H_{11/2}\rightarrow{}^4I_{9/2}$	1491	2.5128	308.8	1.204	1.46	2.5741
$^2H_{11/2}\rightarrow{}^4I_{11/2}$	1128	0.6097	173.1	14.862	< 1%	1.7347
$^2H_{11/2}\rightarrow{}^4I_{13/2}$	798	0.4070	327.3	117.089	2.09	0.9795
$^2H_{11/2}\rightarrow{}^4I_{15/2}$	526	7.1266	20204.5	0	95.19	0.0471
$^4S_{3/2}\rightarrow{}^4F_{9/2}$	3184	0.0537	2.0	0	< 1%	492.5232
$^4S_{3/2}\rightarrow{}^4I_{9/2}$	1681	0.6384	164.2	0	3.27	6.0150
$^4S_{3/2}\rightarrow{}^4I_{11/2}$	1234	0.1558	101.4	0	2.02	3.7354
$^4S_{3/2}\rightarrow{}^4I_{13/2}$	849	0.6986	1397.2	0	27.83	0.6006
$^4S_{3/2}\rightarrow{}^4I_{15/2}$	547	0.4461	3355.7	0	66.84	0.1992
$^4F_{9/2}\rightarrow{}^4I_{9/2}$	3560	1.1937	12.9	4.901	< 1%	56.1394
$^4F_{9/2}\rightarrow{}^4I_{11/2}$	2014	3.2282	193.0	11.496	6.00	4.4974
$^4F_{9/2}\rightarrow{}^4I_{13/2}$	1158	0.4772	150.2	0	4.40	2.6842
$^4F_{9/2}\rightarrow{}^4I_{15/2}$	661	1.7840	3037.9	0	89.08	0.2932
$^4I_{9/2}\rightarrow{}^4I_{11/2}$	4636	0.3902	1.9	1.977	< 1%	257.2009
$^4I_{9/2}\rightarrow{}^4I_{13/2}$	1717	1.4653	141.4	0	33.94	6.8803
$^4I_{9/2}$- $^4I_{15/2}$	812	0.2958	271.4	0	65.13	2.3995
$^4I_{11/2}$- $^4I_{13/2}$	2726	2.7555	55.3	16.048	13.73	14.0132
$^4I_{11/2}\rightarrow{}^4I_{15/2}$	984	1.0465	448.4	0	86.27	1.9236
$^4I_{13/2}\rightarrow{}^4I_{15/2}$	1539	3.2469	310.8	69.525	100	2.6288

AP.3. *Calculated linestrength (S_{ED}),electric (A_{ED}) and magnetic (A_{MD}) transition probabilities, branching ratios, and calculated radiative lifetimes τ^{JO} (ms) of intra-4f eletronic transitions derived from JO analysis for sample $T_{80}B_{15}Z_5:Er_{0.2}$*

intra-4f transition	λ (nm)	S_{ED}	A_{ED} (s^{-1})	A_{MD} (s^{-1})	β (%)	τ^{JO} (ms)
$^4F_{7/2}\rightarrow{}^2H_{11/2}$	7474	1.7694	2.983	0	< 1%	335.2031
$^4F_{7/2}\rightarrow{}^4S_{3/2}$	4787	0.0096	0.062	0	0.0000	328.4049
$^4F_{7/2}\rightarrow{}^4F_{9/2}$	1919	0.1764	17.6	23.742	< 1%	22.5346
$^4F_{7/2}\rightarrow{}^4I_{9/2}$	1244	1.1384	417.0	25.713	0.0399	2.0532
$^4F_{7/2}\rightarrow{}^4I_{11/2}$	976	0.7491	569.7	0	0.0513	0.9463
$^4F_{7/2}\rightarrow{}^4I_{13/2}$	721	0.5299	1005.3	0	0.0906	0.4850
$^4F_{7/2}\rightarrow{}^4I_{15/2}$	492	1.4979	9033.2	0	0.8142	0.0901
$^2H_{11/2}\rightarrow{}^4S_{3/2}$	13316	0.3329	0.066	0	0	15116.0561
$^2H_{11/2}\rightarrow{}^4F_{9/2}$	2582	2.7949	76.1	0.302	< 1%	13.0542
$^2H_{11/2}\rightarrow{}^4I_{9/2}$	1493	2.2583	319.0	1.350	1.49	2.5190
$^2H_{11/2}\rightarrow{}^4I_{11/2}$	1123	0.5632	187.4	16.994	< 1%	1.6627
$^2H_{11/2}\rightarrow{}^4I_{13/2}$	797	0.3777	351.8	132.273	2.25	0.9212
$^2H_{11/2}\rightarrow{}^4I_{15/2}$	526	6.2448	20422.4	0	94.95	0.0465
$^4S_{3/2}\rightarrow{}^4F_{9/2}$	3203	0.0538	2.3	0	< 1%	433.5613
$^4S_{3/2}\rightarrow{}^4I_{9/2}$	1682	0.6381	189.2	0	3.25	5.2219
$^4S_{3/2}\rightarrow{}^4I_{11/2}$	1226	0.1561	119.5	0	2.05	3.2146
$^4S_{3/2}\rightarrow{}^4I_{13/2}$	848	0.7003	1625.0	0	27.93	0.5165
$^4S_{3/2}\rightarrow{}^4I_{15/2}$	548	0.4472	3882.9	0	66.73	0.1718
$^4F_{9/2}\rightarrow{}^4I_{9/2}$	3540	1.0369	13.1	5.615	< 1%	53.2427
$^4F_{9/2}\rightarrow{}^4I_{11/2}$	1986	3.1481	226.5	13.496	6.12	3.8643
$^4F_{9/2}\rightarrow{}^4I_{13/2}$	1154	0.4619	169.8	0	4.33	2.3329
$^4F_{9/2}\rightarrow{}^4I_{15/2}$	661	1.7751	3495.0	0	89.08	0.2549
$^4I_{9/2}\rightarrow{}^4I_{11/2}$	4525	0.3857	2.3	2.395	< 1%	210.9869
$^4I_{9/2}\rightarrow{}^4I_{13/2}$	1712	1.4682	165.0	0	34.51	5.8891
$^4I_{9/2}$- $^4I_{15/2}$	813	0.2922	308.4	0	64.49	2.0909
$^4I_{11/2}$- $^4I_{13/2}$	2753	2.7168	61.1	17.548	13.80	12.7134
$^4I_{11/2}\rightarrow{}^4I_{15/2}$	991	1.0139	491.3	0	86.20	1.7545
$^4I_{13/2}\rightarrow{}^4I_{15/2}$	1548	3.2278	350.7	76.994	100	2.3378

AP. 4. *Calculated linestrength (S_{ED}),electric (A_{ED}) and magnetic (A_{MD}) transition probabilities, branching ratios, and calculated radiative lifetimes τ^{JO} (ms) of intra-4f eletronic transitions derived from JO analysis for sample $T_{60}B_{20}Z_{20}:Er_{0.2}$*

intra-4f transition	λ (nm)	$S_{ED} \cdot 10^{-20}$ (cm^2)	A_{ED} (s^{-1})	A_{MD} (s^{-1})	β (%)	τ^{JO} (ms)
$^4F_{7/2} \rightarrow {}^2H_{11/2}$	7880	1.7121	2.1	0	< 1%	478.9053
$^4F_{7/2} \rightarrow {}^4S_{3/2}$	4824	0.0081	0.043	0	0	469.1657
$^4F_{7/2} \rightarrow {}^4F_{9/2}$	1945	0.1653	13.5	20.0	< 1%	28.0019
$^4F_{7/2} \rightarrow {}^4I_{9/2}$	1258	1.0636	327.6	22.2	3.53	2.5941
$^4F_{7/2} \rightarrow {}^4I_{11/2}$	982	0.6641	437.0	0	4.41	1.2158
$^4F_{7/2} \rightarrow {}^4I_{13/2}$	724	0.4443	758.3	0	7.66	0.6326
$^4F_{7/2} \rightarrow {}^4I_{15/2}$	493	1.3878	8317.7	0	84.03	0.1010
$^2H_{11/2} \rightarrow {}^4S_{3/2}$	12438	0.2812	0.058	0	0	17203.9817
$^2H_{11/2} \rightarrow {}^4F_{9/2}$	2583	2.7690	64.3	0.3	< 1%	15.4712
$^2H_{11/2} \rightarrow {}^4I_{9/2}$	1496	2.1969	265.7	1.2	1.30	3.0166
$^2H_{11/2} \rightarrow {}^4I_{11/2}$	1122	0.5218	151.9	15.2	< 1%	2.0054
$^2H_{11/2} \rightarrow {}^4I_{13/2}$	797	0.3548	297.9	121.4	2.05	1.0894
$^2H_{11/2} \rightarrow {}^4I_{15/2}$	526	6.0901	19558.0	0	95.52	0.0488
$^4S_{3/2} \rightarrow {}^4F_{9/2}$	3260	0.0507	1.8	0	< 1%	570.5602
$^4S_{3/2} \rightarrow {}^4I_{9/2}$	1701	0.5885	144.7	0	2.83	6.8267
$^4S_{3/2} \rightarrow {}^4I_{11/2}$	1233	0.1464	95.8	0	1.87	4.1282
$^4S_{3/2} \rightarrow {}^4I_{13/2}$	852	0.6601	1351.1	0	26.44	0.6276
$^4S_{3/2} \rightarrow {}^4I_{15/2}$	550	0.4216	3516.1	0	68.82	0.1957
$^4F_{9/2} \rightarrow {}^4I_{9/2}$	3558	1.0251	10.9	4.8	< 1%	63.5620
$^4F_{9/2} \rightarrow {}^4I_{11/2}$	1984	2.9923	184.9	11.9	6.07	4.7062
$^4F_{9/2} \rightarrow {}^4I_{13/2}$	1153	0.4142	133.0	0	4.10	2.8949
$^4F_{9/2} \rightarrow {}^4I_{15/2}$	661	1.5855	2897.7	0	89.35	0.3083
$^4I_{9/2} \rightarrow {}^4I_{11/2}$	4484	0.3537	1.9	2.1	1.08	248.5696
$^4I_{9/2} \rightarrow {}^4I_{13/2}$	1707	1.3823	134.6	0	35.98	7.2149
$^4I_{9/2}$- $^4I_{15/2}$	812	0.2471	235.4	0	62.94	2.6735
$^4I_{11/2}$- $^4I_{13/2}$	2756	2.5455	48.6	15.3	13.43	15.6357
$^4I_{11/2} \rightarrow {}^4I_{15/2}$	991	0.9664	412.3	0	86.57	2.0995
$^4I_{13/2} \rightarrow {}^4I_{15/2}$	1548	3.0306	283.6	68.0	100	2.8435